

# Using DNA origami to create hybrid nanophotonic architectures for single-photon emitters

Thesis by  
Anna Mitskovets

In Partial Fulfillment of the Requirements for the  
Degree of  
Doctor of Philosophy in Applied Physics

The logo for the California Institute of Technology (Caltech), featuring the word "Caltech" in a bold, orange, sans-serif font.

CALIFORNIA INSTITUTE OF TECHNOLOGY  
Pasadena, California

2020  
Defended May 29, 2020

© 2020

Anna Mitskovets

ORCID: 0000-0003-1967-5334

All rights reserved

## ACKNOWLEDGEMENTS

I would like to thank Harry Atwater for giving me a chance to work in his very multidisciplinary group. I have enriched my knowledge of physics and material science vastly beyond the research performed for my thesis. Harry always supported me and provided with plentiful professional advice about research projects and career paths throughout this journey. I would also like to thank Paul Rothemund for being a great mentor and an example of how to be an artist while conducting scientific research. I sincerely thank Ashwin Gopinath for introducing me to the DNA origami world and teaching me countless things.

KNI staff and members from different groups have always been responsive and helpful at various points in my time at Caltech. I would like to thank Guy, Melissa, Matt, Alex, Max and Ryan.

I would like to thank my dearest Caltech friends Ruzan, Nina, Sophia, Kelly, Giulia, Yuri the Beautiful, Michelle, Dagny, Benji and Hamid who provided invaluable advice, professional guidance and emotional support. I will cherish our friendship long after leaving Caltech.

I would also like to thank my husband Yury who has supported me during all these years both emotionally and professionally. I am very grateful to my parents, who raised me to be brave, curious and ambitious.

Finally, I would like to thank my committee members: Kerry Vahala, Andrei Faraon, Paul Rothemund, Harry Atwater and Ashwin Gopinath. Kerry and Andrei also served on my candidacy committee and gave extremely helpful and insightful feedback. I had several conversations with Andrei about the research outlook in the field of solid-state single-photon emitters and he was kind to share his personal experience and expertise in the field.

## ABSTRACT

The limitations in physical dimensions of silicon transistors give us a stimulus to explore alternative systems for better computational performance. The most promising system that received a lot of attention in the past few years is a quantum computer. Ideally, a nanophotonic quantum computer would consist of hundreds of single-photon emitters, optical or plasmonic resonators, optical waveguides and interconnects. The main difficulty in large-scale production of such quantum photonic networks is the integration and deterministic coupling of single-photon sources to photonic elements.

In the first part of this thesis, we utilize spontaneous parametric down-conversion to create correlated pairs of indistinguishable photons. These photons are generated by bismuth borate nonlinear crystal and then are coupled to a photonic chip where they interfere at directional couplers to produce a path-entangled state. Our photonic chip consists of waveguides, directional couplers, and a single Mach-Zender interferometer with a thermo-optic phase shifter. When a part of the waveguide connecting directional couplers is replaced with a plasmonic waveguide, quantum state of photons is converted to plasmonic state. Here we report a measurement of path entanglement between surface plasmons with 95% contrast, confirming that a path-entangled state can indeed survive without measurable decoherence. Our measurement suggests that elastic scattering mechanisms of the type that might cause pure dephasing in plasmonic systems must be weak enough not to significantly perturb the state of the metal under the experimental conditions we investigated.

The second part of this work is dedicated to the study of a novel DNA origami self-assembly technique for creating hybrid nanophotonic architectures to create single-photon emitters. DNA origami is a modular platform for the combination of molecular and colloidal components to create optical, electronic, and biological devices. We present a DNA origami molecule that can be deterministically positioned on a silicon chip within  $3.2^\circ$  alignment. Orientation is absolute (all degrees of freedom are specified) and arbitrary (every molecule's orientation is independently specified). The use of orientation to optimize device performance is shown by aligning fluorescent emission dipoles within microfabricated optical cavities. Large-scale integration is demonstrated via an array of 3,456 DNA origami with 12 distinct orientations, which indicates the polarization of the excitation light. Following this experiment, we explore how many molecular emitters can be coupled

to this DNA origami shape and discover interesting interactions between ssDNA extensions that can cause origami to fold along its seam. Finally, we examine DNA origami self-assembly methods that can be used to deterministically couple single-photon emitters to resonators in order to decrease pure-dephasing rates and increase indistinguishability of emitted photons.

## PUBLISHED CONTENT AND CONTRIBUTIONS

Gopinath, Ashwin, Chris Thachuk, Anna Mitskovets, Harry A. Atwater, David Kirkpatrick, and Paul W. K. Rothmund (2018). “Absolute and arbitrary orientation of single molecule shapes”. In: arXiv: 1808.04544 [physics.app-ph].

A.M. participated in atomic force microscopy measurements and discussion of the results.

Fakonas, James S, Anna Mitskovets, and Harry A Atwater (2015). “Path entanglement of surface plasmons”. In: *New Journal of Physics* 17.2, p. 023002. DOI: 10.1088/1367-2630/17/2/023002. URL: <https://doi.org/10.10882F1367-26302F172F22F023002>.

A.M. performed optical measurements and participated in data preparation.

## TABLE OF CONTENTS

Acknowledgements . . . . .	iii
Abstract . . . . .	iv
Published Content and Contributions . . . . .	vi
Table of Contents . . . . .	vi
List of Illustrations . . . . .	viii
Chapter I: Introduction . . . . .	1
1.1 Linear optical quantum computing . . . . .	1
1.2 Single-photon sources . . . . .	2
1.3 DNA origami enabled nanophotonics . . . . .	7
1.4 Scope of this thesis . . . . .	11
Chapter II: Path entanglement of surface plasmons . . . . .	12
2.1 Classical description of surface plasmons . . . . .	12
2.2 Surface plasmon polaritons at a single interface . . . . .	14
2.3 Decoherence of surface plasmons . . . . .	17
2.4 Two-photon quantum interference . . . . .	18
2.5 Path entanglement of surface plasmons . . . . .	20
2.6 Experiment design and fabrication . . . . .	23
2.7 Conclusions . . . . .	28
Chapter III: DNA origami coupled to molecular emitters . . . . .	29
3.1 Method of deterministic DNA origami placement with arbitrary ori- entation . . . . .	29
3.2 DNA origami functionalization with Eu ions . . . . .	41
3.3 Interaction of single-stranded extensions with substrates and each other . . . . .	48
3.4 Conclusions . . . . .	52
Chapter IV: DNA origami as a platform for nanoparticle assembly . . . . .	54
4.1 DNA origami functionalization with QDs . . . . .	54
4.2 Single-photon fluorescent enhancement . . . . .	63
4.3 Optical measurements of a self-assembled nanoplasmonic system with embedded emitters . . . . .	70
4.4 Conclusions . . . . .	73
Bibliography . . . . .	75
Appendix A: Fabrication methods . . . . .	87
A.1 Samples path-entanglement experiments . . . . .	87
A.2 Fabrication and simulation methods of PCC arrays . . . . .	87
A.3 Fabrication of substrates for placement . . . . .	87
A.4 DNA origami preparation . . . . .	88
A.5 DNA origami placement procedure . . . . .	89
A.6 AFM characterization . . . . .	90

## LIST OF ILLUSTRATIONS

<i>Number</i>	<i>Page</i>
1.1 <b>Universal liner optical processor.</b> A: An m-mode circuit that can be used to realize any LO operation. It consists of Mach-Zender interferometers $M_{i,j}$ built from phase shifters (yellow) and beam-splitters, to control photon amplitudes ( $\alpha_{i,j}$ ) and phases ( $\phi_{i,j}$ ). B: Multiphoton ensembles are generated via spontaneous parametric down-conversion, comprising a BiBO crystal, dichroic mirrors (DM), and interference filter (IF), preceded by a pulsed Ti:sapphire laser and second harmonic generation from a bismuth borate (BiBO) crystal. Photons are collected into polarization-maintaining fibers and delivered to the LPU via a packaged v-groove fiber array (VGA). Adapted from (Carolan et al., 2015). . . . .	1
1.2 <b>Schematic representation of a down-conversion process within a nonlinear crystal.</b> A single photon of a frequency $\omega_0$ simultaneously generates a pair of signal and idler photons of frequencies $\omega_1$ and $\omega_2$ subject to the phase-matching conditions. . . . .	4
1.3 <b>Generation of the correlated photons pairs with the same polarization by degenerate down-conversion with type I phase-matching in a BiBO crystal.</b> . . . . .	5
1.4 <b>Design of DNA origami.</b> a: A long single-stranded DNA origami strand is folded to raster fill a shape in red. b: Red crossovers connect different parts of the scaffold (black) together. c: Usually a seam of the origami runs through the middle of the shape. d: Similar to c with strands drawn as helices. e: A finished design after merges and rearrangements along the seam. Adapted from (Rothmund, 2006). . . . .	8
1.5 <b>DNA origami shapes.</b> Top row, folding paths. Second row from top, diagrams showing the bend of helices at crossovers (where helices touch) and away from crossovers (where helices bend apart). Bottom two rows, AFM images. Adapted from (Rothmund, 2006). . . . .	9
2.1 <b>Geometry for surface plasmon propagation.</b> The interface between a dielectric and a metal is parallel to the x-axis and perpendicular to the z-axis. . . . .	15

2.2	<b>Dispersion relation of SPPs at the interface between silver and silica.</b> The real part of the wavevector is depicted by continuous black curve, the imaginary part - by a black broken curve, the light line is shown in blue. . . . .	16
2.3	<b>Classical (a) and quantum (b) interference in a lossless beamsplitter.</b> $A_1$ and $A_2$ are incident classical electromagnetic fields. They correspond to the annihilation operators $\hat{a}_1$ and $\hat{a}_2$ in case of quantum interference. The output classical fields are $B_1$ and $B_2$ with the corresponding annihilation operators are $\hat{b}_1$ and $\hat{b}_2$ . . . . .	19
2.4	<b>Schematic of path-entanglement experiment.</b> BiBO crystal; BPF — bandpass filters ( $814 \pm 2.5$ nm); PM — polarization-maintaining; MM — multimode; SPAD — single-photon avalanche diode; DLSP-PWs — dielectric-loaded surface plasmon polariton waveguides. . . . .	21
2.5	<b>The completed chip.</b> (a) Optical micrograph showing dielectric waveguides (thin dark lines), contact pads (large gold rectangles), DLSPPWs (small gold rectangles), and under-etched region (large dark oval). The two dark, vertical lines in the right half of the image separate the area covered with 350 nm of PMMA (between these lines) from that covered with $2.5 \mu\text{m}$ of PMMA (everywhere else). The dashed box encloses a single interferometer with $10 \mu\text{m}$ DLSPPWs, as represented schematically in figure 2.4. (b) Optical micrograph of the region where the silicon handle has been etched out from underneath the heaters and waveguides. The two light gray, horizontal lines connecting pairs of gold contacts are resistive NiCr heaters, while the long, dark oval between them is the hole through which the underlying silicon was etched. (c) Scanning electron micrograph of a $10 \mu\text{m}$ DLSPPW. (d) Diagram showing a cross-section of the under-etched region. . . . .	24

- 2.6 **Raw measurements on the interferometer that had 10  $\mu\text{m}$  DL-SPPWs.** (a) Top: one-particle interference obtained by blocking one input of the interferometer and recording the count rate at one of the detectors. Bottom: two-particle interference obtained by counting coincidences with both inputs unblocked. Error bars indicate one sample standard deviation above and below the average, calculated from three trials. (b) Resistance of the NiCr heater plotted over its operating range, showing a maximum variation of about 1%. (c) Plot of the phase shift induced by the heater as a function of the power supplied to it, computed from the one-particle interference data. The first maximum of the interference data was taken to correspond to zero phase. . . . . 26
- 2.7 **Measurements of two-particle interference.** Results of interference in the interferometers with 10  $\mu\text{m}$  (left) and 20  $\mu\text{m}$  (right) DLSPWs showing clear path entanglement with visibilities of  $0.954 \pm 0.016$  and  $0.948 \pm 0.021$ , respectively. Each data point marks the average of three measurements, while the error bars represent one sample standard deviation above and below the average. The red curves are sinusoidal fits. . . . . 27
- 3.1 **Schematics and AFM for the death star origami.** (A) Dimensions of the death star origami. (B) Dimensions of the e-beam patterned binding site used for DNA origami placement of the death star origami. (C) AFM of death star origami on an unpatterned  $\text{SiO}_2$  surface. The staples of the death star origami are all modified with 20T extensions, but the symmetry of the death star prevents a determination of whether they are landing right-side up (with 20Ts up) or upside down. (D) AFM of a modification of the death star designed to help verify that death stars bind  $\text{SiO}_2$  right-side up. Inset shows a region of staples (red) which were omitted to break the D1 symmetry of the small moons. The resulting C1 shape allows discrimination based on which edge of the origami looks ragged or broken. Green shading indicates origami which were judged to be right-side up. Of 642 origami inspected, 95.6% (614) were found to be right-side up; 4.4% were found to be upside-down or their orientation could not be determined. . . . . 30

3.2	<b>DNA origami placement of shapes within different symmetry groups.</b> A. DNA origami placement of equilateral triangles does not allow aligning all origami in a certain direction. There are 3 possible orientations with right-side up and 3 orientation with right-side down. B. Asymmetric "moon-like" origami shapes can self-assemble with only two possible absolute orientations: right-side up and upside-down. . . . .	31
3.3	<b>DNA origami placement of death star origami.</b> . . . . .	31
3.4	<b>DNA origami placement of death star origami.</b> Averaged AFM (N=600) of DNA origami placement on arrays of A: small moon sites, B: disk-shaped sites. . . . .	32
3.5	<b>Annotated AFM of small moon origami placed on square array of 105 nm diameter disk-shaped binding site.</b> Scale bar, 2 $\mu\text{m}$ . Red circles indicate single origami binding events (at 83% of 600 sites) which were cut out automatically and averaged to yield annular image in figure 3.4B. . . . .	33
3.6	<b>Annotated AFM of death star origami placed on a square array of small moon binding sites.</b> Scale bar, 2 $\mu\text{m}$ . Blue ovals indicate which sites were not analyzed. The remaining 592 sites (98.7% of 600 total sites; only 529 sites are shown) were cut out and averaged to yield the reconstruction of the death star in figure 3.4A. Orientation of each death star was automatically extracted and they were found to be oriented to $0^\circ \pm 6.7$ degrees. We suggests that the discrepancy between this orientational fidelity, and that measured optically ( $\pm 3.2^\circ$ ) can be explained by a poorer ability to measure the orientation of small moons from AFM data, which are noisy and have apparent salt artifacts (see white dots on origami). . . . .	34
3.7	<b>Death star intercalation by TOTO-3 fluorescent molecule.</b> Rotation of the fluorescent dye TOTO-3's absorption dipole along the length of a TOTO-3 intercalated helix. Coordinate system shows relationships between helix axes, excitation polarization ( $\beta$ ) and origami rotation ( $\theta$ ). . . . .	35

- 3.8 **Fluorescence microscopy of TOTO-3 intercalated into DOP arrays on disk-shaped and shape-matched sites (ex. 642 nm; em. 660 nm).** Fluorescence microscopy of TOTO-3 intercalated into DOP arrays on disk-shaped and shape-matched sites (ex. 642 nm; em. 660 nm). A and C Intensity (red dots) of N=600 sites in B and D as a function of excitation polarization. Blue line, best fit. . . . . 35
- 3.9 **Schematic and raw fluorescence data for death star origami placed on a 1  $\mu\text{m}$  period square array 105 nm diameter disk-shaped binding sites.** A: Schematic indicates that death star origami will bind with random orientations and the excitation dipoles of intercalated TOTO-3 fluorophores will be uncontrolled. B: 36 images show the rotation of excitation light polarization (green) relative to the array axis (blue) in  $10^\circ$  increments. Variations in the intensity of death star origami are uncorrelated. . . . . 36
- 3.10 **Schematic and raw fluorescence data for death star origami placed on a 1  $\mu\text{m}$  period square array of small moon binding sites.** A: Schematic indicates that death star origami will align to the binding sites and in turn align the excitation dipoles of intercalated TOTO-3 fluorophores. B: 36 images show the rotation of excitation light polarization (green) relative to the array axis (blue) in  $10^\circ$  increments. Variations in the intensity of death star origami are highly correlated, and small moons are brightest when the polarization axis lines up with the array axis. . . . . 37

- 3.11 **Analysis of orientation based on fluorescence data.** A: A subsection of data presented in figure 3.9, TOTO-3 labelled death stars bound to disk-shape binding sites. Ten particular binding sites are highlighted with differently colored circles. B: Traces of fluorescence intensity from ten binding sites highlighted in A, as a function of the orientation of excitation polarization  $\beta$ . All of the  $k = 1$  to 600 individual traces can be fit to  $I_0 \cos^2(\beta - \theta) + c$ . C: Histogram of  $\theta_k$  aggregated into  $10^\circ$  bins shows that the  $\theta_k$  are randomly distributed and that death stars exhibit no preferential orientation on disk-shaped sites. The flat histogram further suggests that the excitation polarization is that intended, and that the experimental setup introduces no undesired anisotropy. D: Histogram of  $\theta_k$  aggregated into  $1^\circ$  bins for data from figure 3.10, the binding of small moons to shape-matched binding sites.  $\theta_k$  cluster around  $0^\circ$  with a standard deviation of  $3.2^\circ$ . . . . . 38
- 3.12 **Design and raw data for the polarimeter.** A: Design shows the orientation of small moon origami in each of the 12 rays of the polarimeter. DNA helices are perpendicular to the ray and so the excitation dipole of intercalated TOTO-3 is aligned parallel to the ray. B: 36 images of the polarimeter under polarized illumination; green arrows indicate axis of polarization. . . . . 39
- 3.13 **Mechanism of fluorescent emission from europium compound.** A: Chemical formula of europium chelate complex labelled by single-stranded DNA. B: Chelated europium ion is attached to sensitizer molecule that absorbs light at wide range of UV wavelengths. This energy is transferred to Eu ion which later emits fluorescent light at 616nm. . . . . 41
- 3.14 **DNA origami labelled by Eu ions.** A: Eu ion chelated complexes were labelled by 20A DNA strands and attached to death star origami with 20T extensions via different procedures. B: Measured spectra of Eu ions immobilized on the  $\text{SiO}_2$  substrate via DNA origami covalent bonding to the surface at room temperature. C: AFM image of death star origami labelled by Eu ions. . . . . 42

- 3.15 **Samples for DNA origami arrays.** A: Image of a sample with gold grid lines and labelled squares under white light illumination in a microscope. B: A single 3 by 3 array of disk-shaped DNA origami binding sites fabricated inside a gold frame of a labelled square. C: Death star DNA origami modified with 235 20T ssDNA extensions. . . . . 43
- 3.16 **DNA origami placement of death stars labelled by Eu ions.** A: An AFM image of a 9 by 9 array of unmodified death star. B: An AFM images of a 5 by 5 array of unmodified death star. C: An AFM image of a 9 by 9 array of death star origami modified with 235 20T extensions and linked to Eu ions. D: An AFM image of a 5 by 5 array of death star origami modified with 235 20T extensions and linked to Eu ions. E-F: Epifluorescence image of a grid with arrays of death star origami labelled with Eu ions under UV excitation light with emission filtered at 620 nm. E: 9 by 9 array of death star origami modified with 235 20T extensions and linked to Eu ions. F: 5 by 5 array of death star origami modified with 235 20T extensions and linked to Eu ions. . . . . 44
- 3.17 **Death star DNA origami with 235 20T extensions.** A: Post stained electrophoresis gel imaged in the channel of SYBR gold fluorescence. B: Prior to staining electrophoresis gel imaged by cell phone camera. C: AFM image of sample with 5 times higher concentration of Eu labelled ssDNA. D: AFM image of sample with lower concentration of Eu labelled ssDNA. . . . . 45
- 3.18 **Death star DNA origami with 20T extensions.** A: Death star DNA origami with 235 20T extensions. Every staple that forms death star origami shape was modified by adding 20T to its sequence. B: Death star DNA origami with 42 20T extensions formed by 14 clusters of 3 20T extensions located at the circumference of the disk. . . . . 46
- 3.19 **Death star DNA origami with 42 20T extensions.** A: An AFM image of a 5 by 5 array of death star origami modified by 42 20T extensions and linked to Eu ions. B: An AFM image of a 9 by 9 array of death star origami modified with 42 20T extensions and linked to Eu ions. C: Epifluorescence image of a grid with 9 by 9 arrays of death star origami labelled with 42 Eu ions under UV excitation light with emission filtered at 620 nm. . . . . 47

3.20 **Death star origami placement with 232 20C extensions.** A: Death star DNA origami with 232 20C extensions and 3 5'-ACTACTACTACTACTACT-3' strands in the middle of the origami. B: AFM of death star DNA origami with 232 20C extensions immobilized on silanized surface of SiO<sub>2</sub>. C: AFM of a part of a 9 by 9 array of death star origami with 20C extensions. D: AFM of a 4 by 4 array of the same origami with 20C extensions. . . . . 48

3.21 **Death star DNA origami with 235 5'-GTTGTAGTGGTATGAGGTTG-3' extensions.** A: Death star DNA origami with 235 20T extensions. Every staple that forms death star origami shape was modified by adding 20T to its sequence. B: Death star DNA origami with 42 20T extensions formed by 14 clusters of 3 20T extensions located at the circumference of the disk. . . . . 50

3.22 **Death star DNA origami with variable number of 5'-GTTGTAGTGGTATGAGGTTG-3' extensions per origami.** A: Death star DNA origami with X% of staples modified 5'-GTTGTAGTGGTATGAGGTTG-3' sequence and the rest of the staples are not modified and correspond to the "bare" death star origami. B-F: AFM images of death star DNA origami immobilized on SiO<sub>2</sub> and ethanol dried. Each AFM image has different percentage (X%) of modified staples, meaning that approximately one death star has X·235/100 extensions. B: 0% corresponds to "bare" or unmodified death star, that usually does not form taco. C: 25% of staples are modified with extensions. You can see that tacos start appearing in the AFM. D: 50% of staples have extension. In the AFM scans of large areas with sufficient numbers of origami show about half of death stars folded into tacos. E: 75% of staples have extension and a higher percentage of origami is folded. F: 100% almost all origami folded into tacos. . . . . 51

4.1 **DNA origami functionalization with QDs.** A: Death star DNA origami labelled with 42 20T strands arranged in groups of three. B: Death star DNA origami labelled with 3 20T strands. These three strands extend from the neighboring staples and are designed to hold a single QD in the middle like a tripod. C: To functionalize QD by 20A DNA strands, we incubate streptavidin coated QDs with 20A ssDNA with biotin at 3' end. . . . . 55

4.2	<b>AFM images of death star origami functionalized with QDs</b> A: Each origami was designed to capture 14 QDs, however, the average number of QDs per origami is 6 due to large hydrodynamic radius of QDs. B: Each origami was modified to carry only one QD, but the average number of QDs per origami is 0.5 with some origami having zero QDs. This can be explained by half of the death stars attaching face down to the surface and blocking the 20T extensions from binding to a QD. . . . .	56
4.3	<b>Fabrication flow diagram of a microring with DNA origami on top.</b> . . . . .	57
4.4	<b>DNA origami placement on microrings</b> A: SEM images of a microring with 4 $\mu\text{m}$ diameter. B: Zoomed-in side SEM image of the ring, which is 200nm tall and about 300nm wide. C: AFM image of DNA origami with QDs positioned equidistantly on top of a ring by using DNA origami directed self-assembly method. D: Closer AFM of a segment of the ring with origami and QDs. . . . .	58
4.5	<b>Photoluminescence of QDs</b> A: Fluorescence from an array of 4 $\mu\text{m}$ rings functionalized by QDs under 488 nm excitation laser. B: Spectra of this fluorescence shows peak at 655 nm, which corresponds to emission of QDs. . . . .	59
4.6	<b>Death star origami with one binding site for a QD.</b> A: A death star is functionalized with 20C extensions to break the symmetry and insure that that origami always attaches to the surface with the right-side up. One binding site for a QD is in the middle consists of three ssDNA making a tripod construction for a QD. B: AFM image of these origami immobilized on $\text{SiO}_2$ . . . . .	59
4.7	<b>Single QD-origami system.</b> Our system with highest percentage of single QDs coupled to single origami. The AFM shows 87% of origami have only a single QD attached to the origami. . . . .	60

- 4.8 **Density gradient ultracentrifugation.** Absorbance of different fractions at 260 nm of origami sample coupled to a single QD. The first peak corresponds to short staples that were not coupled to QDs. The sharp peak at 28 nm is comprised of single origami that do not carry QDs. The broader peak after that at 35 nm correspond to the origami coupled to only one QD. The peaks after 38 nm position are due to absorption of origami with more than one QD, origami dimers and QDs that are not bound to origami. . . . . 61
- 4.9 **Gel electrophoresis and AFM of individual fractions collected after ultracentrifugation.** A: AFM image of the sample in the well number 12, which corresponds to a fraction with a single origami. B: Sample with one QD per origami as shows in the AFM of the sample in the well 19. C: Sample in the well 22 shows significant fluorescence in the gel scanner which is emitted by two QDs per origami. . . . . 62
- 4.10 **Design of a silicon nitride ring.** A: Geometry of the ring. The outer radius is  $2.2 \mu\text{m}$  and the inner radius is  $1.8 \mu$ . The ring is etched into 270 nm of silicon nitride and supported by several micrometers of silicon dioxide layer. B: Electric-field profile of a cross-section of the ring shows that the light is confined in the ring and a bit is leaking into the silicon dioxide substrate. C: Spectral response of such a ring has several sharp peaks that can be matched with emission of europium ions or QDs. . . . . 64
- 4.11 **Electric field of a microring.** A: Top view of the electric-field profile of the cross-section of the ring. Whispering gallery mode manifests in the multiple antinodes equidistant along the ring. B: Angular distribution of electric field projected into the far field of the ring. The majority light escapes through the side walls of the ring. . . . . 65
- 4.12 **Plasmonic nanocube dimer.** A: Geometrical dimensions and configuration of two 50 nm gold nanocubes with a horizontal dipole in between. The two cubes are separated by 3 nm and are sitting on top. B: View from the top. C: Radiative decay rate as a function of emission wavelength of a dipole from A and B. . . . . 66

- 4.13 **Electric-field distribution.** A: View from the side. Electric field is confined in the space between two cubes. B: Far field angular distribution of  $|\vec{E}|^2$  demonstrates that the system outcouples the light effectively into the far field. . . . . 67
- 4.14 **Fabrication of a 50nm gold dimer.** A: SEM image of a gold cube. B: Coupling schematic of a nanocube functionalized with DNA strands and a death star origami with complimentary extensions. C: AFM showing an attempt to couple nanocubes to a placed death star origami array. It seems that the used nanocubes do not bind to origami on immobilized on the surface. . . . . 67
- 4.15 **Gold nanostructure assembled via DNA origami.** A: Three gold spheres with a 30 nm diameter are attached to a triangular origami. A gold triangular plate 20 nm thick and with a 48 nm side in located in the middle of the origami. B: TEM image of the structures provided by Risheng Wang. C: AFM image of a structure deposited on a glass slide scanned in air. . . . . 68
- 4.16 **Electromagnetic simulation of the nanostructure.** A: The response in the structure was recorded after being excited by a horizontal dipole pointing in the direction of the center of the triangular plate. B: The structure is deposited on a 5 nm SiO<sub>2</sub> spacer layer on top of gold. C: Electric-field profile at  $\lambda = 555$  nm from 3D FDTD simulation in Lumerical software. D. Purcell factor for different wavelengths with respect to the dipole spontaneous decay rate in vacuum. . . . . 69
- 4.17 **AFM of the sample with 3 emitters per structure.** This AFM image shows that not all the structures remained in the initial configuration after deposition and ethanol drying procedures. Several structures aggregated, others lost one or more elements or deformed. However, one structure in the AFM has designed organization of its elements. . . . . 70
- 4.18 **Scanning confocal microscope setup.** In this experiment the samples were excited by 532 nm CW laser for PL measurements and with 532 nm pulsed laser for time-resolved measurements. The sampled were scanned by a fast steering mirror and background was reduced by confocal pinhole. The PL maps and time-resolved PL were acquired with single-photon avalanche photodiodes (SPADs) and the spectra from the sampled was measured by a monochromator with a Peltier cooled CCD camera. . . . . 71

- 4.19 **Photoluminescence maps of the samples.** A: A gold nanostructure with 3 ATTO molecules. B: A gold nanostructure with one ATTO molecule. C: A PL map of the sample with structures in A deposited on silicon dioxide chip. D: A PL map of the sample with structures in B deposited on silicon dioxide chip. E: The intensity cross-section of one of the bright spots of the PL map in C was fitted with a Gaussian curve. The parameters of the fitting curve are: radius equals to  $0.5 \mu\text{m}$  and the amplitude equals  $5.4 \cdot 10^4$ . F: The parameters of the fitted Gaussian for the intensity distribution of one of the spots in D: radius equals to  $0.5 \mu\text{m}$  and the amplitude equals  $1.8 \cdot 10^4$ . This amplitude value in the sample A is three times large than the corresponding value of the sample B for all the spots, which suggests that light is emitted from a single ATTO molecule in sample B. . . . . 72
- 4.20 **Measurements of an ensemble ATTO molecules.** A: PL decay rate at log scale is a line. The lifetime of ATTO molecules obtained from the plot is 4 ns. B: AFM image of triangular origami with a single ATTO molecule. C: Triangular origami with a single ATTO molecules and removed gold nanoparticles. D: PL spectra of an ensemble of ATTO molecules coupled to DNA origami and excited by a CW laser with 532 nm wavelength and  $5 \mu\text{W}$  power. After each 30 s the PL significantly reduces and goes to background level in 2 min. . . . . 73

## Chapter 1

## INTRODUCTION

## 1.1 Linear optical quantum computing

As chipmakers around the world push the performance of extreme ultraviolet lithography and Samsung reports the smallest manufactured transistor size of 3 nm, we are approaching physical limits in the number of atoms that can operate as a classical gate. While quantum computers cannot offer a comprehensive replacement for classical computers, they can solve problems such as factoring large integers, optimization problems and quantum physics simulations that are impossible for any classical supercomputer in the world. Quantum computing can significantly aid in

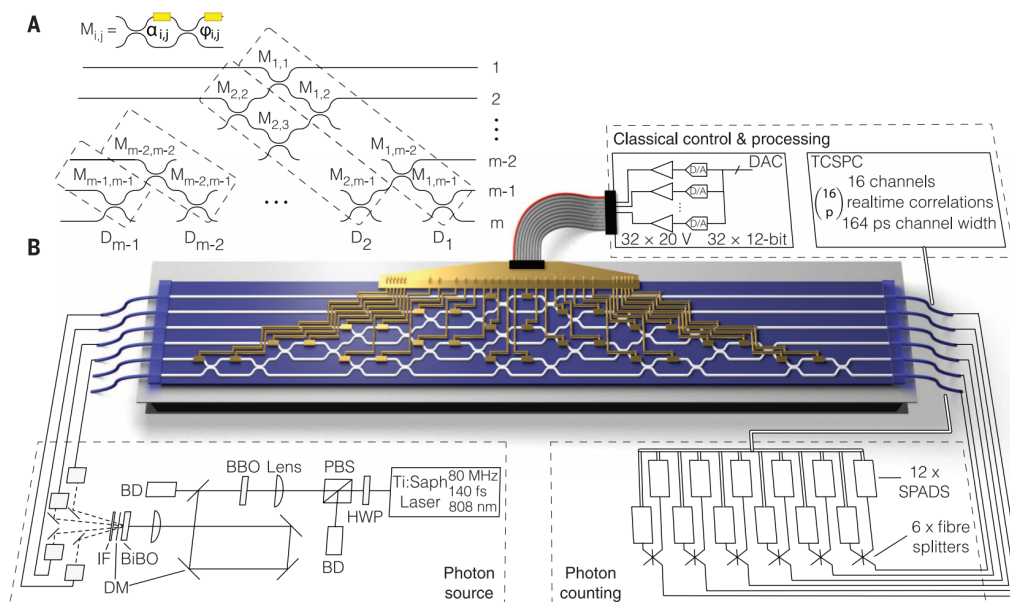


**Figure 1.1: Universal linear optical processor.** A: An  $m$ -mode circuit that can be used to realize any LO operation. It consists of Mach-Zender interferometers  $M_{i,j}$  built from phase shifters (yellow) and beamsplitters, to control photon amplitudes ( $\alpha_{i,j}$ ) and phases ( $\phi_{i,j}$ ). B: Multiphoton ensembles are generated via spontaneous parametric down-conversion, comprising a BiBO crystal, dichroic mirrors (DM), and interference filter (IF), preceded by a pulsed Ti:sapphire laser and second harmonic generation from a bismuth borate (BiBO) crystal. Photons are collected into polarization-maintaining fibers and delivered to the LPU via a packaged v-groove fiber array (VGA). Adapted from (Carolan et al., 2015).

drug discovery, break modern encryption protocols, introduce secure communications and expand the power of artificial intelligence. That is why companies are racing to build reliable quantum computers and governments invest billions of dollars for academic research.

In 2001 (Knill, Laflamme, and Milburn, 2001) proposed a method for efficient quantum computation that relies on using only beamsplitters, phase shifters, single-photon sources and photo-detectors. (Carolan et al., 2015) built a universal linear optical processor (LPU) and demonstrated implementation of several quantum information protocols with a maximum number of six photons. The proposed processor itself could be easily scaled up by semiconductor manufacturing process. Furthermore, integrated options exist for single-photon detection such as superconducting nanowire single-photon detectors (Goltsman et al., 2001). However, scaling up spontaneous down-conversion sources requires significant increase in the laser power and a huge number of involved free-space optical components. In the next section, we will discuss different examples of solid-state single-photon sources and their suitability for large-scale fabrication.

## 1.2 Single-photon sources

For the first time, a single-photon source was demonstrated in 1974 by utilizing a cascade transition within mercury atoms (Clauser, 1974). Since then many systems were used for generation of single-photons. Many quantum key distribution experiments ((Bennett et al., 1992), (Hiskett et al., 2006), (Fernandez et al., 2007)) used weak coherent pulses of a laser beam attenuated down to a single-photon level. This method was convenient, even though weak coherent pulses are pseudo-single-photon sources.

- **Trapped atoms.** A true single-photon source is an isolated two-level atom system. The excitation of the neighboring atoms may result in multi-photons emission, thus various isolation and filtering techniques can be applied such as ion-traps, optical cavities and magneto-optical traps. However, isolating a single atom with the help of traps is very challenging, requires bulky apparatus and not scalable for multi-qubit operations.
- **Color centers in diamond.** In 1954, (Kaiser and Bond, 1959) identified that diamond can have isolated single nitrogen impurities and (Brouri et al., 2000) observed photon antibunching in the fluorescent light emitted from

a single nitrogen-vacancy center in diamond at room temperature. Color centers in diamond until now remain one of the top candidates for on demand single-photon generation sources.

- **Quantum dots.** Quantum dots (QDs) are small semiconductor particles or structures that confine electron in three dimensions and cause quantization of energy transitions. The fluorescence of colloidal CdSe/ZnS nanocrystals at room-temperature exhibits perfect antibunching under excitation as was studied in (Michler et al., 2000) and (Brokmann et al., 2004). Additional techniques can be applied to improve indistinguishability of emitted photons (Saxena et al., 2019). The indistinguishability of these solid-state emitters is largely limited by dephasing and can be mitigated by using optical cavities in these systems. By far the fabrication method of QDs that gives the best results is self-assembly. This method is described in the review (Buller and Collins, 2009). Unfortunately, self-assembly is a random process and it is impossible to control the precise location of a QD. This nature of self-assembled QDs makes it difficult to integrate them into nanofabricated cavities and build large-scale optical networks.
- **Monolayer transition metal dichalcogenides and monolayer and multi-layer hexagonal boron nitride.** 2D materials gained popularity in the recent years due to the several advantages over emitters embedded into 3D materials such as color centers in diamond and QDs. Atomically thin transition metal dichalcogenides, such as MoS<sub>2</sub>, MoSe<sub>2</sub>, WS<sub>2</sub>, and WSe<sub>2</sub> (Tonndorf et al., 2015) and two-dimensional hexagonal boron nitride (Tran et al., 2016) show much greater quantum efficiency and single-photon emission rates at room temperature. Integration strategies of 2D materials with microfabricated photonic networks require precise pick-and-place techniques, which is extremely challenging (Peyskens et al., 2019). However, CMOS compatibility and potential for electric tuning and control of emission makes 2D materials one of the most promising hosts for single-photon emitters.
- **Heralded photons.** Heralded means that the presence of a photon in one mode is defined by the detection of its pair photon. The most popular types of heralded single-photon sources are spontaneous parametric down-conversion ((Hong and Mandel, 1986), (X. Zhang, Xu, and Ren, 2018)) and spontaneous four-wave mixing. The next section describes spontaneous parametric down-conversion in detail.

## Spontaneous parametric down-conversion

Spontaneous parametric down-conversion is a nonlinear process, which is used in quantum optics for generation of correlated photon pairs. The correlated photon pairs are generated in a nonlinear crystal from the incident single photons of a pump frequency  $\omega_0$ . Conservation of the energy requires that the initial and generated photons with frequencies  $\omega_1$  and  $\omega_2$ , respectively, will satisfy the following relation:

$$\omega_0 = \omega_1 + \omega_2.$$

Moreover, the momentum of the system of the initial and generated photons also needs to be preserved:

$$\mathbf{k}_0 = \mathbf{k}_1 + \mathbf{k}_2,$$

where  $k_i$  is a wave vector of the photon in the crystal as depicted in the figure 1.2.

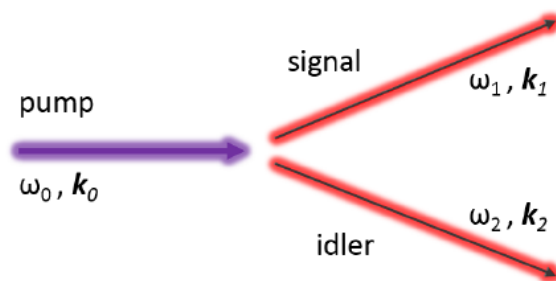


Figure 1.2: **Schematic representation of a down-conversion process within a nonlinear crystal.** A single photon of a frequency  $\omega_0$  simultaneously generates a pair of signal and idler photons of frequencies  $\omega_1$  and  $\omega_2$  subject to the phase-matching conditions.

The second condition is equivalent to requiring that the nonlinear waves and the fundamental beam all remain in phase throughout the nonlinear medium. These two conditions are also called phase-matching conditions (Fox, 2006).

Due to the dispersion of the refractive index in the nonlinear crystal there are a limited number of the frequencies combinations allowed by phase-matching conditions. Phase-matching conditions can be divided into the two types according to the polarization of the initial and generated beams. In the type I phase-matching the polarizations of the down-converted photons are parallel to each other and orthogonal to the pump photon, while in type II phase-matching the down-converted photons have orthogonal polarizations (Bhar, 1991).

Since for the perfect two-photon quantum interference we need a pair of nondistinguishable photons, we use degenerate spontaneous parametric down-conversion process in a BiBO nonlinear crystal. When a strong UV pump laser beam is directed at the crystal, most of the photons continue straight through it. However, occasionally some of the photons undergo spontaneous down-conversion with type I polarization correlation and the resultant correlated photon pairs have trajectories that are constrained to be within a cone, which axis is parallel to the pump beam. Due to the conservation of energy, the two photons are always symmetrically located within the cone, relative to the pump beam as in figure 1.3.

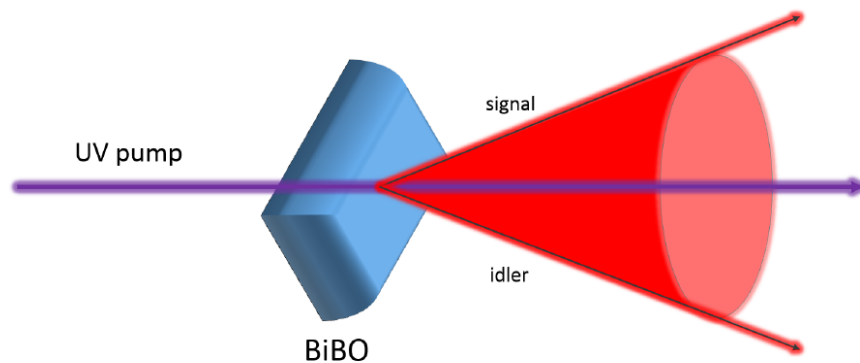


Figure 1.3: **Generation of the correlated photons pairs with the same polarization by degenerate down-conversion with type I phase-matching in a BiBO crystal.**

The BiBO crystal has excellent optical properties such as a high nonlinearity effect, a wide range of transparency from the ultraviolet to infrared wavelength and a high damage threshold. It has been used extensively in research for generation of entangled photons. The theoretical investigation of the optimal phase-matching conditions in the spontaneous parametric down-conversion process undergoing in the BiBO crystal one can find in (Huo, H. Chen, and M. Zhang, 2016).

### **Integrated single-photon sources**

The progress in electronic and optical devices is mainly driven by miniaturization of the functional components and confinement of light. This approach enables to decrease energy consumption and material use. If several material systems are utilized, such device can be called as hybrid (Benson, 2011). Ideally a nanophonic hybrid quantum network would consist of hundreds of single-photon emitters, optical or plasmonic resonators, optical waveguides and interconnects. The main

difficulty in large-scale production of such quantum photonic networks is the integration and deterministic coupling of single-photon sources to photonic elements. All existing fabrication methods can be divided into the following categories:

- **Stochastic or random.** This is probably the most widespread method since it does not require additional fabrication efforts. In this method, single-photon emitters (colloidal and self-assembled QDs, color centers in diamond) are randomly positioned or grown on a substrate in large quantities. Then, a number of resonators or optical circuits are fabricated on the same substrate on top of the layer with quantum emitters. Afterwards, the substrate is scanned for the devices that by chance got an optical cavity built on top of an emitter. The yield of such process is very small, however, there is a number of distinguished researchers that built such systems and demonstrated quantum electrodynamics phenomena on an integrated photonic platform (Englund, Faraon, et al., 2007), (Faraon et al., 2011), (Choy et al., 2011).
- **Deterministic scanning and localization.** This approach requires identifying the position of an emitter on a surface of the substrate prior to positioning a cavity. Atomic force microscopy was used to locate an absolute position of self-assembled QDs in (Hennessy et al., 2007). In the following step, a photonic crystal cavity was positioned relative to the pre-selected QD, so that the electric-field maximum of the cavity was aligned to the QD. They have observed a strong coupling of the QD to the cavity in the spectral and time domains. Another method in this category includes using a scanning probe tip to push a cavity over an emitter as in (Englund, Shields, et al., 2010). Other scanning-probe approaches are discussed in the review (Benson, 2011) but all of them are inherently impossible to scale up.
- **Directed self-assembly.** Directed self-assembly method is based on lithographically pre-defining sites that are able to immobilize nanoparticles ((Y. Chen et al., 2018), (Jiang et al., 2015)) or molecular single-photon emitters (Gopinath, Miyazono, et al., 2016). In the case of nanoparticles such as colloidal QD the sites have to be small enough to hold exactly one particle, which is challenging for the current semiconductor UV technologies due to the small QD size. However, directed self-assembly is the most promising method for creating scalable hybrid nanophotonic networks for quantum computing and communication. In this work, we are focused on the method of directed DNA

self-assembly, which will be described in the following sections. This method is fully CMOS compatible, scalable and offers a greater resolution compared to other top-down directed self-assembly techniques.

### **1.3 DNA origami enabled nanophotonics**

#### **DNA self-assembly**

As was discussed in the previous chapter, the top-down semiconductor nanofabrication methods have limitations on the resolution and, ultimately, on the number of electronic components that can fit in a personal computing device. Molecular self-assembly is spontaneous organization of molecules into stable, structurally well-defined aggregates under equilibrium (Whitesides GM, 1991). These methods typically produce relatively large structures between 1 and 100 nm in size and with molecular weights from  $10^4$  to  $10^{10}$  daltons. The larger molecular aggregates are comparable in size to the structures developed by photolithographic methods and provide an alternative and inexpensive method to conventional top-down fabrication techniques.

Deoxyribonucleic acid is a molecule composed of two polynucleotide chains that form a double helix carrying genetic information. The two DNA strands are composed of monomeric structures that are called nucleotides. There are only 4 types of nucleobases: cytosine (C), guanine (G), adenine (A) or thymine (T). Together with a sugar called deoxyribose, and a phosphate group nucleobases compose nucleotides. The nucleotides are attached to one another through hydrogen bonds forming a DNA double helix. Watson-Crick base pairing principle allows each type of nucleobase to bind with just one type of nucleobase. Therefore, each single strand of the DNA can be joined by a specific complimentary strand. The Watson-Crick property allows designing DNA nanostructures with great combinatoric variability. Since the diameter of each strand of DNA is about 2 nm, and the helical pitch is about 3.5 nm, each nucleotide base pair could be considered as a building block or "pixel" in the field of "DNA nanotechnology" (Nadrian C. Seeman, 1982). In nature, genome DNA exists in highly wrapped conformation assisted by histone proteins in order to fit in a cell nucleolus and fulfill its biological functions (Jin and Grote, 2016). However, these programmed DNA molecules always take linear shapes. Branched DNA tiles are introduced to increase the complexity and rigidity of DNA

nanostructures. This principle was used to create a number of two-dimensional periodic structures (Nadrian C Seeman and Lukeman, 2004),(Chworos et al., 2004) and three-dimensional shapes (J. Chen and Nadrian C. Seeman, 1991), (Y. Zhang and Nadrian C. Seeman, 1994).

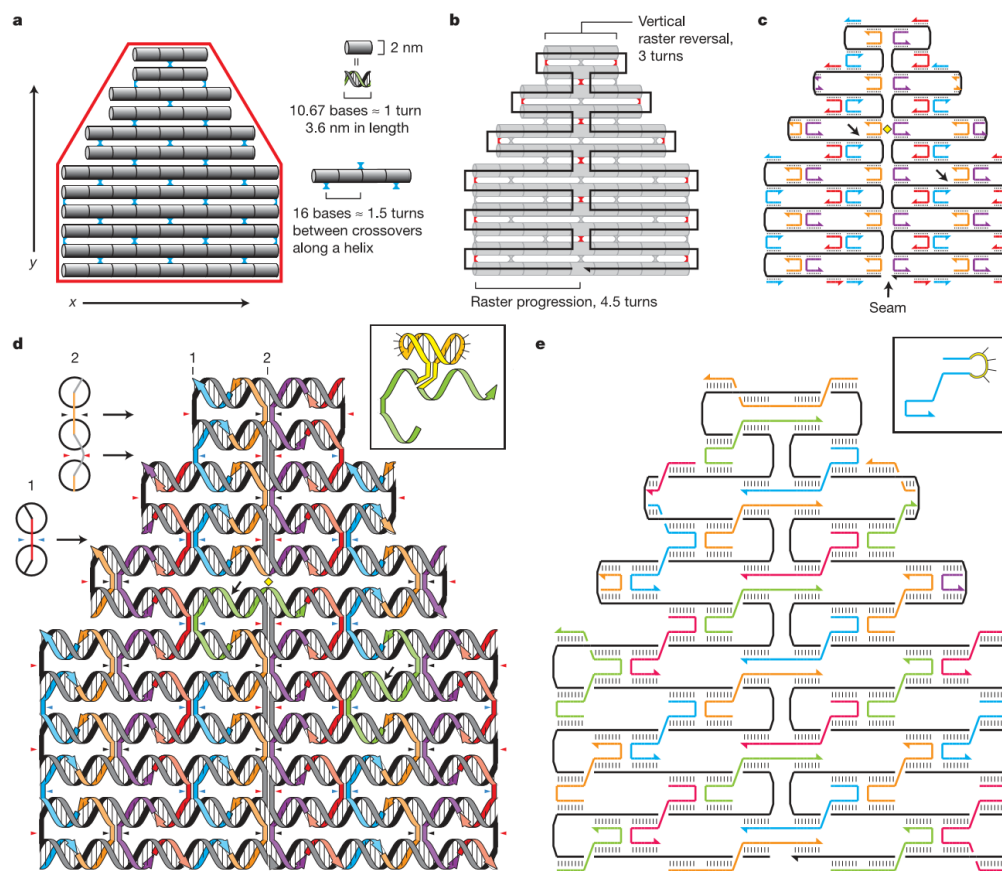


Figure 1.4: **Design of DNA origami.** a: A long single-stranded DNA origami strand is folded to raster fill a shape in red. b: Red crossovers connect different parts of the scaffold (black) together. c: Usually a seam of the origami runs through the middle of the shape. d: Similar to c with strands drawn as helices. e: A finished design after merges and rearrangements along the seam. Adapted from (Rothemund, 2006).

In 2006, Paul Rothemund presented a new self-assembly technique which he called "scaffolded DNA origami" (Rothemund, 2006). DNA origami can be formed by folding a long single strand of DNA into desired shapes and using numerous short single strands of DNA that work like staples holding a shape together. A geometric model of a DNA origami is first designed by raster filling a desired shape of DNA origami by a double helix as depicted in figure 1.4. To hold the shape composed of the double helices together, shorter strands, or "staples", are used to

create crossovers at specific locations. This method enables to synthesize various 2D and 3D shapes 1.5. Besides increased structural versatility of such nanostructures, surface of DNA origami shapes is composed of hundreds of individually accessible pixels. These pixels form a so-called "breadboard", every point of each could be accessed through DNA strands and functionalized with compatible molecules and nanoparticles. The majority of examples of implementation of DNA origami self-assembly for nanophotonic structures are dealing with a 100-nm-sized DNA origami shapes with a spatial resolution of about 5 nm.

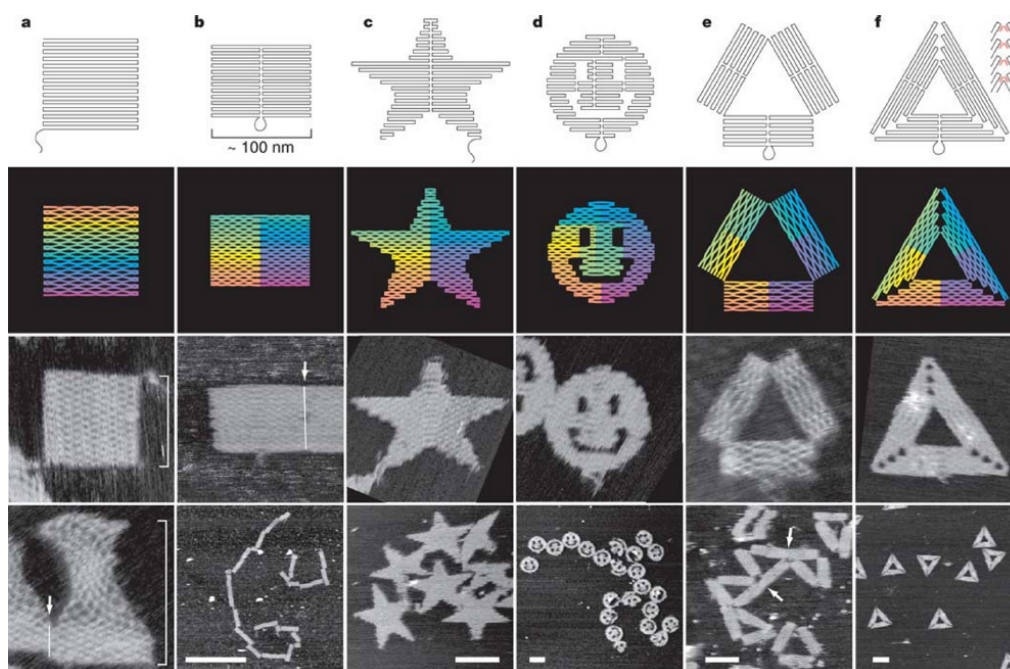


Figure 1.5: **DNA origami shapes..** Top row, folding paths. Second row from top, diagrams showing the bend of helices at crossovers (where helices touch) and away from crossovers (where helices bend apart). Bottom two rows, AFM images. Adapted from (Rothemund, 2006).

## DNA nanophotonics

Driven by relatively cheap DNA synthesis costs, advanced and accessible computational design and analysis tools, DNA origami based nanotechnology evolves rapidly and facilitates a myriad of innovative studies demonstrating novel applications in material science. Nanometer-precise positioning of organic dyes and biomolecules at a large scale is easily achievable. Hybrid self-assembly of DNA origami functionalized with plasmonic nanoparticles, colloidal QDs and organic dyes is more challenging due to interface chemistry between different components.

However, there are several successful examples in the field of nanophotonics as discussed in (Pilo-Pais et al., 2017). DNA origami enabled self-assembly of hybrid nanostructures is specifically successful in confinement and manipulation of light due to the high arrangement precision of synthesized structures (Acuna et al., 2012). Thus, Purcell enhancement of light  $\geq 4 \times 10^3$  was demonstrated in (Chikkaraddy, Turek, et al., 2018) and strong coupling was achieved at room temperature (Chikkaraddy, Nijs, et al., 2016).

### **Deterministic positioning of DNA origami**

In this thesis, we are focused on the exceptional property of DNA origami to bind to pre-defined areas of the substrate under certain conditions. As discussed above, directed self-assembly is crucial for building quantum optical networks at a larger scale. The advantage of the DNA origami comes from leveraging both its structural versatility and a larger molecular size. Within the shape of the DNA origami, it can be accessed and functionalized every 5-nm of its surface area by designing an appropriate combination set of sticky staples. Furthermore, it is possible to electrostatically immobilize origami on binding sites and, since origami is a large molecule with a size of around 100nm, these sites could be defined lithographically with much greater precision than smaller sites for a single nanoparticle of a 5-nm size. Directed self-assembly method of DNA on lithographically defined structures was demonstrated in a number of works ((Hung et al., 2010), (Kuzyk et al., 2008), (Kershner et al., 2009), (Gerdon et al., 2009), (Gao et al., 2010), (Ding et al., 2010), (Penzo et al., 2011), (Pearson et al., 2011), (Scheible et al., 2014)), however, the method presented by (Gopinath and Rothmund, 2014) has proven to be the most versatile and accurate. The full scalability, 5-nm precision and integration with standard semiconductor manufacturing process of directed DNA origami self-assembly was demonstrated in (Gopinath, Miyazono, et al., 2016). For that paper, the authors were able to fabricate specifically designed 65,536 optical devices on a single chip. Each device comprised of a photonic crystal cavity and a number of DNA origami that was varied from 0 to 7, representing 8 intensity levels. DNA origami were positioned in the antinodes of the cavities and had either 3 or 15 organic dyes resonant with the cavities. By collecting the fluorescence from the arrays of such devices, they were able to reproduce a famous painting by Van Gogh with a 65,536-pixel greyscale image.

## 1.4 Scope of this thesis

Chapter II of this thesis covers our work on quantum path entanglement of surface plasmons. The purpose of this work was to experimentally study microscopic interaction between surface plasmons and other excitations in material. We studied surface plasmon propagation through plasmonic waveguides integrated on a chip but, similarly to the majority of papers in this area, our source of heralded photons and single-photon detectors were separate devices. This project opened our eyes on a number of fundamental difficulties in integrated quantum photonics, such as coupling efficiencies and absorption rates in plasmonic waveguides and bulky size of single-photon generation systems. Thus, we have spent a significant amount of time learning about scalable techniques for integration of single-photon sources and appropriate strategies for efficient collection, enhancement and outcoupling of light from these sources.

In the chapter III, we introduce the method of directed DNA origami self-assembly on different substrates characterized by atomic force microscopy. We describe how a particular origami shape can be used to achieve absolute orientation on the substrate. Furthermore, we achieve large-scale implementation of this method by integrating fluorescent molecular dipoles into devices with nanofabricated cavities and measuring polarization of emitted light. We also address the question of coupling large numbers of emitters to death star origami and deterministic placement of definite numbers of emitters on different substrates.

Chapter IV is dedicated to the problems of indistinguishability of solid-state emitters. We propose using DNA origami self-assembly methods to deterministically couple single-photon emitters to resonators in order to decrease pure-dephasing rates. First, we discuss coupling of colloidal QDs to DNA origami and optimize parameters for self-assembly and purification procedures. Then we study assembly methods for efficient coupling of single-photon emitter to resonators. We demonstrate fabricated microring resonator with QDs located in the antinodes of the electric field on top of the ring. Afterwards, we discuss gold nanostructures organized by DNA origami and the potential spontaneous rate enhancement of molecular emitters in such antennas.

Finally, we describe fabrication methods and procedures in Appendix A.

*Chapter 2***PATH ENTANGLEMENT OF SURFACE PLASMONS**

Metals can sustain travelling electromagnetic waves at their surfaces supported by the collective oscillations of their free electrons in unison. Remarkably, classical electromagnetism captures the essential physics of these "surface plasma" waves using simple models with only macroscopic features, accounting for microscopic electron–electron and electron–phonon interactions with a single, semi-empirical damping parameter. Nevertheless, in quantum theory these microscopic interactions could be important, as any substantial environmental interactions could decohere quantum superpositions of surface plasmons, the quanta of these waves. Here we report a measurement of path entanglement between surface plasmons with 95% contrast, confirming that a path-entangled state can indeed survive without measurable decoherence. Our measurement suggests that elastic scattering mechanisms of the type that might cause pure dephasing in plasmonic systems must be weak enough not to significantly perturb the state of the metal under the experimental conditions we investigated.

**2.1 Classical description of surface plasmons**

Plasmons are quantized excitations in a plasma, i.e. oscillations of the free electron gas in metals. Collective excitations in classical plasmas were first studied by Langmuir (Langmuir, 1928). An experimental evidence for the existence of plasmons as a quantized excitation of the valence electrons in metals came from characteristic energy-loss measurements (Marton et al., 1962). Multiple equidistant peaks in the energy-loss spectrum of keV electrons transmitted through a thin metallic foil presented a direct evidence for the quantization of the plasmon energy.

The concept of surface plasmons was introduced by Ritchie (Ritchie, 1957) shortly after the discovery of bulk plasmons in metals. Surface plasmons are quanta of the surface plasma wave excited at the interface between a metal and dielectric material. Similarly to photons, surface plasmons are bosons: they are vector excitations and have spin 1. The bosonic nature of single surface plasmons was first discussed in the works of surface plasmon amplification by stimulated emission of radiation (Spaser) (Bergman and Stockman, 2003) and (Stockman,

2008). However, classical approach captures the essential physics of surface plasmon and is capable of explaining its optical properties such as dispersion relation and propagation. This theory treats electrons as independent particles and does not consider lattice potential and interactions between electrons.

The simplest classical theory that gives a dispersion relation for surface plasmon propagation is Drude model. In this model free gas of electrons oscillate in the response to the applied electromagnetic field. These oscillations are damped due to collisions between electrons with an average time  $\tau$  between these collisions. The equation of motion for an electron can be written as in (Maier, 2007):

$$m\mathbf{x} + m\gamma\mathbf{x} = -e\mathbf{E} \quad (2.1)$$

If we assume harmonic oscillation of the driving field  $\mathbf{E}(t) = \mathbf{E}_0 \exp(-i\omega t)$ , a particular solution to the equation of motion of a free electron in the Drude model is presented by the following expression:

$$\mathbf{x}(t) = \frac{e}{m(\omega^2 + i\gamma\omega)}\mathbf{E}(t) \quad (2.2)$$

Macroscopic polarization is a vector sum of electron dipole moments  $\mathbf{P} = -en\mathbf{x}(t)$  is proportional to the driving electric field  $\mathbf{E}$ :

$$\mathbf{P}(t) = -\frac{e^2n}{m(\omega^2 + i\gamma\omega)}\mathbf{E}(t), \quad (2.3)$$

and displacement field is explicitly given by:

$$\mathbf{D}(t) = \varepsilon_0\left(1 - \frac{\omega_p^2}{\omega^2 + i\gamma\omega}\right)\mathbf{E}(t), \quad (2.4)$$

where  $\omega_p = \frac{ne^2}{\varepsilon_0m}$  is plasma frequency of the Drude metal and depends on the concentration of the free electrons in the metal. The expression for dielectric constant  $\varepsilon$  is then given by:

$$\varepsilon(\omega) = \varepsilon_0\left(1 - \frac{\omega_p^2}{\omega^2 + i\gamma\omega}\right). \quad (2.5)$$

Let us consider different frequency regimes and the dependence of the dielectric constant  $\varepsilon$  on damping parameter  $\gamma = 1/\tau$ . It can be decomposed according to the physical nature of collisions between electrons, electrons and phonons and other microscopic interactions involving electrons:

$$1/\tau = 1/\tau_{e-e} + 1/\tau_{e-ph} + \dots + 1/\tau_{surf}. \quad (2.6)$$

When the frequency of the electric field is large compared to the frequency of electronic collisions  $\omega\tau \gg 1$ , the system experience negligible damping and  $\varepsilon(\omega)$  becomes predominantly real:

$$\varepsilon(\omega) = 1 - \frac{\omega_p^2}{\omega^2}. \quad (2.7)$$

However for real metals this regime is substantially modified by intraband transitions. These interaction can be accounted for by adding a restoring force into (2.1) in a Lorenz-Drude model:

$$m\mathbf{x} + m\gamma\mathbf{x} + m\omega_0\mathbf{x} = -e\mathbf{E}. \quad (2.8)$$

## 2.2 Surface plasmon polaritons at a single interface

Now we can find solutions for an electromagnetic wave travelling at the interface of a dielectric with permittivity  $\varepsilon_d$  and a metal with permittivity  $\varepsilon_m$ . Maxwell's equations for harmonic waves in the absence of space charges and currents take the following form:

$$\nabla \cdot \mathbf{D} = 0 \quad (2.9)$$

$$\nabla \times \mathbf{E} - i\omega\mathbf{B} = 0 \quad (2.10)$$

$$\nabla \cdot \mathbf{B} = 0 \quad (2.11)$$

$$\nabla \times \mathbf{H} + i\omega\mathbf{D} = 0 \quad (2.12)$$

where for the dielectric medium the expression for the displacement field is  $\mathbf{D} = \varepsilon_0\varepsilon_d\mathbf{E}$ , for the metal the field  $\mathbf{D}$  has a similar expression  $\mathbf{D} = \varepsilon_0\varepsilon_m\mathbf{E}$  and field  $\mathbf{H} = \frac{1}{\mu_0}\mathbf{B}$ .

As shown in the 2.1, we consider the interface between the metal and the dielectric in the  $x - y$  plane, the region  $z > 0$  has permittivity  $\varepsilon_d$  and the region  $z < 0$  has permittivity  $\varepsilon_m$ . Equations (2.9) - (2.12) pose restriction for  $\mathbf{H}$ :

$$\mathbf{H}(\mathbf{r}, \omega) = \begin{pmatrix} 0 \\ H_y(z)e^{i(k_x x - \omega t)} \\ 0 \end{pmatrix}, \quad (2.13)$$

where the direction of the wave propagation is along the  $x$ -axis. The components of  $H_y(z)$  exponentially decay away from the surface:

$$H_y(z) = \begin{cases} H_{y,0}e^{zk_z^d} & z > 0 \\ H_{y,0}e^{zk_z^m} & z < 0 \end{cases}. \quad (2.14)$$

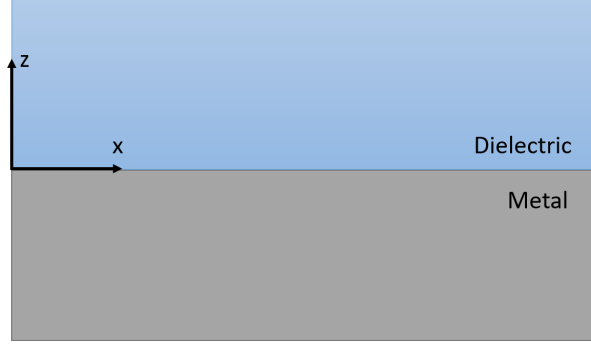


Figure 2.1: **Geometry for surface plasmon propagation.** The interface between a dielectric and a metal is parallel to the x-axis and perpendicular to the z-axis.

Similarly, we can derive that:

$$\mathbf{E}(\mathbf{r}, \omega) = -\frac{1}{i\omega\epsilon_0\epsilon_{m,d}} \begin{pmatrix} -H'_y(z)e^{i(k_x x - \omega t)} \\ 0 \\ ik_x H_y(z)e^{i(k_x x - \omega t)} \end{pmatrix}, \quad (2.15)$$

Wave equation can be obtained by taking a curl from (2.12):

$$\nabla^2 \mathbf{H} = \frac{\omega^2}{c^2} \epsilon_{m,d} \mathbf{H}, \quad (2.16)$$

and by substitution of  $\mathbf{H}$  from (2.13) into (2.16) we can get relations for  $x$  and  $z$  components of  $k$  - vector:

$$(k_z^d)^2 = k_x^2 - \epsilon_d \frac{\omega^2}{c^2}, \quad (2.17)$$

$$(k_z^m)^2 = k_x^2 - \epsilon_m \frac{\omega^2}{c^2}. \quad (2.18)$$

Using the boundary condition for  $x$ -component of the field  $\mathbf{E}$ , we obtain the relation for  $k_z$  in the dielectric and in the metal:

$$\frac{k_z^m}{k_z^d} = -\frac{\epsilon_m}{\epsilon_d}. \quad (2.19)$$

Finally, we arrive at the central result of this section, **dispersion relation** of SSP propagating at the interface between dielectric and metal:

$$k_x = \frac{\omega}{c} \sqrt{\frac{\epsilon_m \epsilon_d}{\epsilon_m + \epsilon_d}}. \quad (2.20)$$

Figure 2.2 shows dispersion relation of SPPS propagating between a Drude metal and an air with unit permittivity and between a metal and a fused silica with

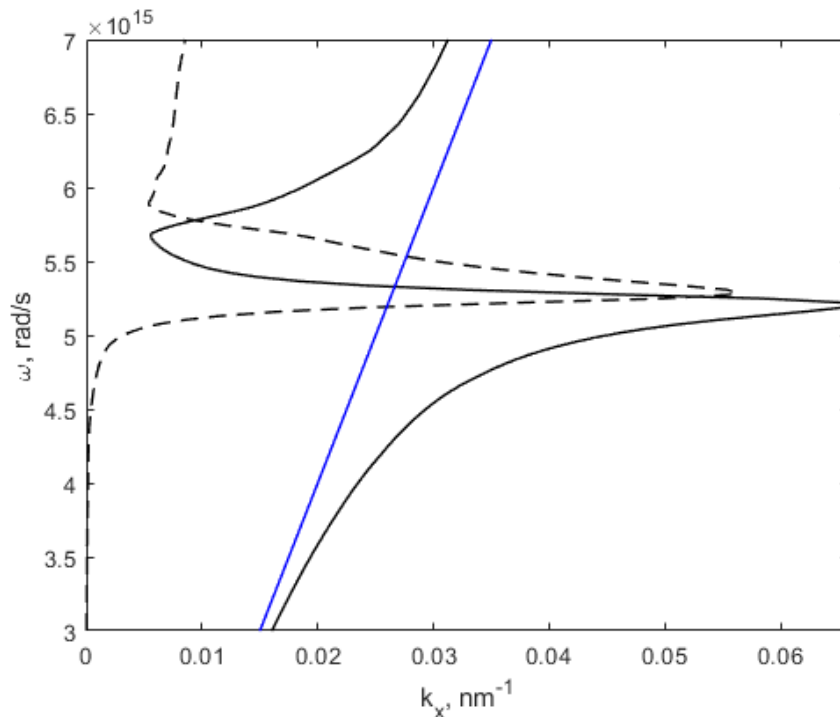


Figure 2.2: **Dispersion relation of SPPs at the interface between silver and silica.** The real part of the wavevector is depicted by continuous black curve, the imaginary part - by a black broken curve, the light line is shown in blue.

permittivity value of 2.25. On y-axis we have the frequency  $\omega$  and on x-axis we have values for wave vector  $k_x$ . The real part of the wavevector  $k_x$  is presented by continuous curves and the imaginary part by broken curves. The straight line corresponds to the light dispersion silica. For small wave vectors SPP propagation line is close to the light line and it is expected that surface plasmons that belong to this region would exhibit similar quantum properties as optical photons. In the experiments described in this chapter we used dielectric-loaded surface plasmon polariton waveguides (DLSPPWs) to sustain SPPs propagation on the chip. The detailed electromagnetic field description of the plasmon mode was calculated via 3D FDTD simulation software Lumerical and the geometrical parameters of the waveguide were chosen to minimize propagation losses. This regime corresponds to "light-like" plasmons in our experiment. A similar quantum entanglement experiment with plasmons belonging to a more dispersive region was also performed in our group and is described in (Tokpanov et al., 2019).

### 2.3 Decoherence of surface plasmons

Classical models of surface plasma waves usually account for the microscopic scattering effects responsible for loss using a single, semi-empirical Drude damping parameter (Liu, Pelton, and Guyot-Sionnest, 2009). It is then straightforward to quantize these waves by analogy to electromagnetic fields in free space (Elson and Ritchie, 1971), (Tame, Lee, et al., 2008), (Archambault et al., 2010), (Tame, McEney, et al., 2013) with surface plasmons, their quanta, playing an analogous role to photons. Experiments in the last several years have tested this analogy, demonstrating singleparticle statistics (Akimov et al., 2007), (Kolesov et al., 2009), (Heeres, Dorenbos, et al., 2010), (Giuliana Di Martino et al., 2012), squeezing (Huck et al., 2009), entanglement (Altewischer, Exter, and Woerdman, 2002), (Fasel et al., 2005), and quantum interference (Heeres, Kouwenhoven, and Zwiller, 2013), (Fakonas et al., 2014), (G. Di Martino et al., 2014), (Fujii, Fukuda, and Inoue, 2014), (Cai et al., 2014) in plasmonic circuits.

As hybrid excitations that involve both electromagnetic and electronic components, surface plasmons occupy an interesting middle ground between photonic systems, which typically interact weakly with their environments, and electronic systems, which usually suffer much stronger environmental interactions. In particular, classical theories of surface plasmons include extra microscopic interactions such as electron–electron, electron–phonon, and electron–surface scattering (Liu, Pelton, and Guyot-Sionnest, 2009) that are absent for photons. These scattering mechanisms contribute both to the absorption of a plasmon, which creates an electron–hole pair, and the subsequent thermalization of the hot electron and hole. The full extent of these interactions is still a matter of some controversy, however, as elastic scattering processes might (Guo et al., 2010), (Scharte et al., 2001) or might not (Scharte et al., 2001), (Sönnichsen et al., 2002) cause ‘pure dephasing’ of plasmons that have not yet been absorbed.

If a surface plasmon scatters from phonons or electrons in the metal that supports it without being absorbed, thereby leaving behind a record of its existence in the electronic or atomic motions of the metal, it should be possible to detect such a scattering event as decoherence in a measurement of entanglement between plasmons. Experiments to date have shown that photons that are entangled by polarization (Altewischer, Exter, and Woerdman, 2002) or frequency (Fasel et al., 2005) converted to plasmons and back to photons, but an experiment with path-entangled plasmons has not been reported. One reason the latter experiment is particularly

interesting is that the entangled state should decohere if the metals involved (i.e. the 'environment') can detect the mere presence or absence of plasmons, as opposed to distinguishing between their polarization states or frequency components. We also note that the plasmonic waveguides we used for this experiment showed greater confinement, dispersion, and loss than those studied in previous entanglement experiments. Accordingly, we expect interactions between the plasmons and their environment to be stronger in our case.

## 2.4 Two-photon quantum interference

Quantum interference in beam splitters is used in many optical linear quantum computation schemes to create two-photon path-entangled states. The simplest example of such two-photon quantum interference (TPQI) is the Hong-Ou-Mandel interference.

Let us consider two beams of photons of the same polarization and frequency coming from a single-photon source. These two beams contain correlated photon pairs. When the path lengths of the beams are identical, the two photons arrive at the beam splitter at the same time and interfere. When the single photons interfere at a 50-50 beam splitter, destructive interference prevents the possibility that the two photons go to different output ports, and both photons therefore emerge at the same output in an entangled state. To find a rigorous explanation of TPQI, we need to consider the beamsplitter in a fully quantum mechanical context. At a level of single or a few photons, the classical approach to the beam splitting produces erroneous and quite misleading results (Gerry and Knight, 2004).

In a classical lossless beamsplitter, the two incident fields of complex amplitudes  $A_1$  and  $A_2$  interfere with each other resulting in the output fields  $B_1$  and  $B_2$  as depicted in figure 2.3. This can be expressed by the following relation using the matrix representation:

$$\begin{pmatrix} B_1 \\ B_2 \end{pmatrix} = \frac{1}{\sqrt{2}} \begin{pmatrix} 1 & i \\ i & 1 \end{pmatrix} \begin{pmatrix} A_1 \\ A_2 \end{pmatrix}. \quad (2.21)$$

The complex  $i$  that appears twice in (2.21) originates from the phase difference that occurs for one of the reflections in the beamsplitter. This phase difference is required by the law of the conservation of the energy and also holds in the case of quantum interference. To treat the beamsplitter quantum mechanically, we should replace the classical complex field amplitudes  $A_i$  and  $B_i$  by a set of annihilation

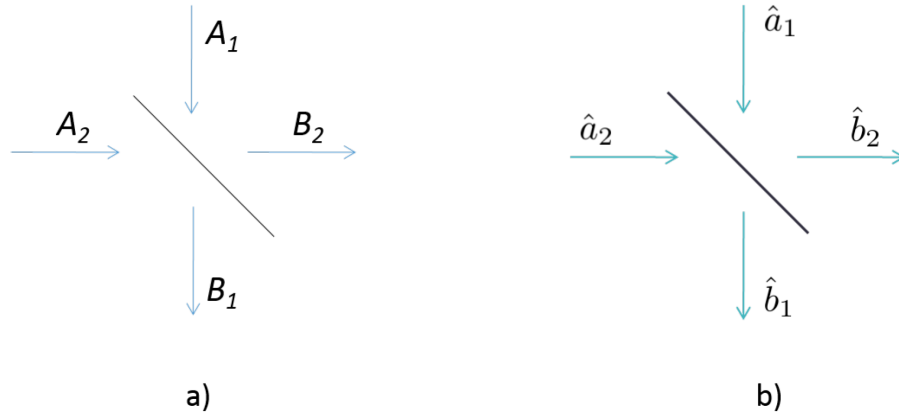


Figure 2.3: **Classical (a) and quantum (b) interference in a lossless beamsplitter.**  $A_1$  and  $A_2$  are incident classical electromagnetic fields. They correspond to the annihilation operators  $\hat{a}_1$  and  $\hat{a}_2$  in case of quantum interference. The output classical fields are  $B_1$  and  $B_2$  with the corresponding annihilation operators are  $\hat{b}_1$  and  $\hat{b}_2$ .

operators  $\hat{a}_i$  and  $\hat{b}_i$ , where  $i = 1, 2$ . This results in the following equation:

$$\begin{pmatrix} \hat{b}_1 \\ \hat{b}_2 \end{pmatrix} = \frac{1}{\sqrt{2}} \begin{pmatrix} 1 & i \\ i & 1 \end{pmatrix} \begin{pmatrix} \hat{a}_1 \\ \hat{a}_2 \end{pmatrix}. \quad (2.22)$$

The corresponding creation operators are found by taking the Hermitian conjugates of (2.22):

$$\begin{pmatrix} \hat{b}_1^\dagger \\ \hat{b}_2^\dagger \end{pmatrix} = \frac{1}{\sqrt{2}} \begin{pmatrix} 1 & -i \\ -i & 1 \end{pmatrix} \begin{pmatrix} \hat{a}_1^\dagger \\ \hat{a}_2^\dagger \end{pmatrix}. \quad (2.23)$$

When the two photons interfere in the beamsplitter the input state can be expressed in the form:

$$|\Psi\rangle_{in} = |1, 1\rangle,$$

where  $|1, 1\rangle$  is a state, when one photon is impinging on the input 1 and one photon is impinging on the input 2. This state is created by two creation operators acting on a  $|0, 0\rangle$  state:

$$|\Psi\rangle_{in} = \hat{a}_1^\dagger \hat{a}_2^\dagger |0, 0\rangle.$$

The creation operators of the output mode can be calculated from (2.23) and related to the creation operators of the input mode:

$$\begin{pmatrix} \hat{a}_1^\dagger \\ \hat{a}_2^\dagger \end{pmatrix} = \frac{1}{\sqrt{2}} \begin{pmatrix} 1 & i \\ i & 1 \end{pmatrix} \begin{pmatrix} \hat{b}_1^\dagger \\ \hat{b}_2^\dagger \end{pmatrix}. \quad (2.24)$$

Now, we can use (2.24) to construct the output state from the action of the transformed creation operators on the vacuum states of the output mode, since it is being obvious that an input vacuum transforms to an output vacuum:

$$|0, 0\rangle_{in} \rightarrow |0, 0\rangle_{out}.$$

Thus, we can write:

$$\begin{aligned} \hat{a}_1^\dagger \hat{a}_2^\dagger |0, 0\rangle_{in} &= \frac{1}{2}(\hat{b}_1 + i\hat{b}_2)(i\hat{b}_1 + \hat{b}_2) |0, 0\rangle_{out} \\ &= \frac{1}{2}(i(\hat{b}_1)^2 + i(\hat{b}_2)^2) |0, 0\rangle_{out} \\ &= \frac{i}{\sqrt{2}}(|2, 0\rangle_{out} + |0, 2\rangle_{out}). \end{aligned} \quad (2.25)$$

This is an important result. At the output of our system we obtained a superposition of the two states or the two-photon path-entangled state. Apparently, the two photons emerge together such that photo-detectors placed in the output beams should not register simultaneous counts. In fact, the absence of the simultaneous counts can be used as an indication that the photons arrive at the first beamsplitter at the same time.

Our motivation was to compare propagation of a quantum-entangled state through almost lossless dielectric waveguides with propagation through strongly dispersive plasmonic waveguides. In the setup when a two-photon path-entangled state is generated at the dielectric beamsplitter and is propagated away towards photo-detectors, the entangled state interacts with its environment before it impinges on the detectors. If this interaction is strongly decohering, it will cause a collapse of the wave function of the entangled state into a statistical mixture of  $|2, 0\rangle$  and  $|0, 2\rangle$  states. Nevertheless, 50% of the photons in this statistical mixture will be in the state  $|2, 0\rangle$  and the rest 50% will be in the state  $|0, 2\rangle$  and the detectors will not register coincidence counts, in the case when the two initial photons arrive at the beamsplitter at the same time. Thus, with the setup with a single beamsplitter is not able to indicate whether the interaction between the entangled photons and their environment resulted in the decoherence of their quantum superposition state.

## 2.5 Path entanglement of surface plasmons

Figure 2.4 shows a schematic of our experiment. We create pairs of single photons by spontaneous parametric down-conversion (SPDC) and couple them into

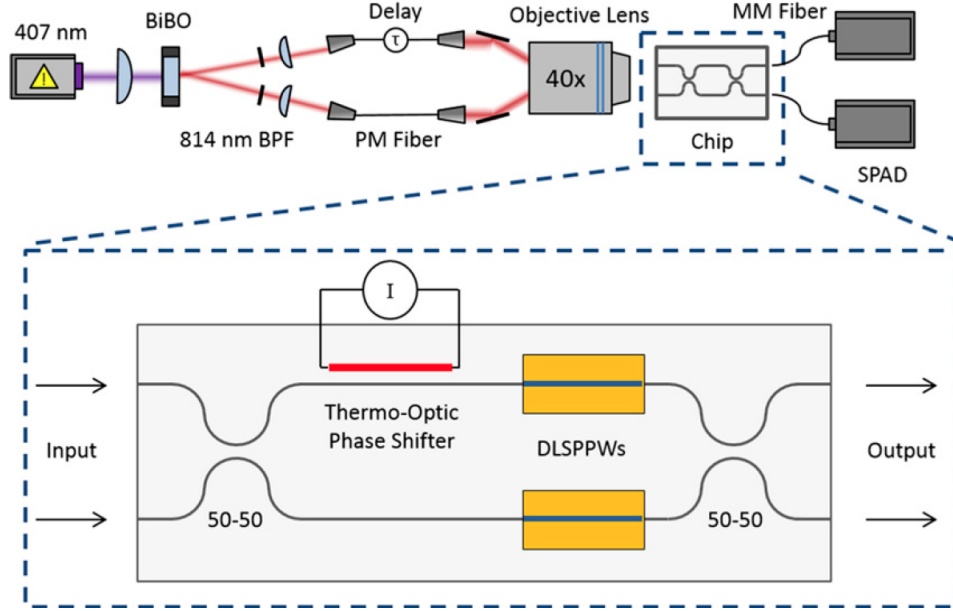


Figure 2.4: **Schematic of path-entanglement experiment.** BiBO crystal; BPF — bandpass filters ( $814 \pm 2.5$  nm); PM — polarization-maintaining; MM — multimode; SPAD — single-photon avalanche diode; DLSPPWs — dielectric-loaded surface plasmon polariton waveguides.

a pair of waveguides which we fabricate on a silicon chip. The waveguides are coupled at two sequential 50–50 directional couplers, forming a Mach–Zehnder interferometer, and a resistive heater shifts the phase in one of the waveguides by the thermo-optic effect. Between the directional couplers, we integrate dielectrically loaded surface plasmon polariton waveguides (DSLPPWs) into the dielectric waveguides. Above we derived that quantum interference at the first coupler produces a path-entangled state:

$$|1, 1\rangle \otimes |E_i\rangle \xrightarrow{\text{1st coupler}} \frac{1}{\sqrt{2}}(|2, 0\rangle + |0, 2\rangle) \otimes |E_i\rangle, \quad (2.26)$$

where as before  $|i, j\rangle$  denotes a state with  $i$  photons in one waveguide and  $j$  photons in the other but we omitted the subscripts "in" and "out" to avoid overcrowding the formulae.  $|E_i\rangle$  represents the state of the environment before the photons are converted to surface plasmons. Here, "the environment" refers to all of the degrees of freedom of the electrons and phonons in the two metal pads that form the plasmonic waveguides. (We describe decoherence in this system using a von Neumann model of measurement, as described in section 3 of (Schlosshauer, 2005).) The heater introduces a phase shift to only the component in which both photons are in the first

waveguide:

$$\frac{1}{\sqrt{2}}(|2, 0\rangle + |0, 2\rangle) \otimes |E_i\rangle \xrightarrow{\text{phase shift}} \frac{1}{\sqrt{2}}(e^{i2\Delta\phi}|2, 0\rangle + |0, 2\rangle) \otimes |E_i\rangle. \quad (2.27)$$

Note that the relative phase  $\Delta\phi$  imparted by the heater contributes a phase to the state  $|2, 0\rangle$  which is twice as large. The factor of two comes from two powers of the creation operator,  $\hat{a}^\dagger$ , each shifted by  $\Delta\phi$ , as in:  $|2, 0\rangle = (e^{i\Delta\phi}\hat{a}^\dagger)^2|0, 0\rangle$ .

At the plasmonic waveguides, the state of the environment evolves along with the state of the plasmons:

$$\frac{1}{\sqrt{2}}(e^{i2\Delta\phi}|2, 0\rangle + |0, 2\rangle) \otimes |E_i\rangle \xrightarrow{\text{plasmons}} \frac{1}{\sqrt{2}}(e^{i2\Delta\phi}|2, 0\rangle \otimes |E_{2,0}\rangle + |0, 2\rangle \otimes |E_{0,2}\rangle). \quad (2.28)$$

Here,  $|E_{0,2}\rangle$  is the state of the environment that would result from both plasmons traversing the first waveguide, and  $|E_{2,0}\rangle$  is the corresponding state for the other case. These two states are equal if the plasmons do not interact at all with their environment, but they would be different in the case that the plasmons elastically scatter from electrons or phonons, as described earlier. Note also that we have ignored components of the resulting state that have fewer than two plasmons. Physically, this corresponds to post-selecting for only those trials in which neither plasmon was absorbed.

Finally, quantum interference at the second coupler produces a complicated output state:

$$\begin{aligned} \xrightarrow{\text{2nd coupler}} \frac{1}{4} & \left[ e^{i2\Delta\phi} (\sqrt{2}|2, 0\rangle - 2i|1, 1\rangle - \sqrt{2}|0, 2\rangle) \otimes |E_{2,0}\rangle \right. \\ & \left. + (-\sqrt{2}|2, 0\rangle - 2i|1, 1\rangle + \sqrt{2}|0, 2\rangle) \otimes |E_{0,2}\rangle \right] \end{aligned} \quad (2.29)$$

Constructing the density operator corresponding to this state and tracing over the degrees of freedom of the environment gives the reduced density operator of the surface plasmons,  $\rho_{\text{red}}$ , from which the probability of detecting simultaneous counts at the outputs can be found:

$$P_{\text{coinc}} = \langle 1, 1 | \rho_{\text{red}} | 1, 1 \rangle = \frac{1}{2} \left[ 1 + |\langle E_{2,0} | E_{0,2} \rangle| \cos 2\Delta\phi \right]. \quad (2.30)$$

In the absence of interactions between the plasmons and the environment, we have  $|E_{2,0}\rangle = |E_{0,2}\rangle$  and, as a result,  $P_{\text{coinc}} = \frac{1}{2}(1 + \cos 2\Delta\phi)$ . In contrast, if the

surface plasmons alter the state of the metal such that  $|\langle E_{2,0}|E_{0,2}\rangle| < 1$ , the amplitude of the sinusoidal oscillation of  $P_{\text{coinc}}$  is reduced, with the case  $|\langle E_{2,0}|E_{0,2}\rangle| = 0$  corresponding to total decoherence and no dependence of  $P_{\text{coinc}}$  on  $\Delta\phi$ . As a result, by measuring the coincidence count rate at the outputs of the waveguides as a function of the applied phase,  $\Delta\phi$ , we can probe the perseverance or decoherence of the path-entangled plasmon state.

## 2.6 Experiment design and fabrication

For our SPDC source, shown schematically in figure 2.5, we use a 100 mW, 407 nm diode laser and a BiBO crystal to generate pairs of single photons at 814 nm. Lenses on either side of the crystal focus the laser onto it and collect the divergent down-converted light from it. A pair of identical 5 nm bandpass filters centered at 814 nm isolate the down-converted photons from background light, and collimators collect them into polarization-maintaining fiber. When we connect these fibers to our silicon single-photon avalanche diodes (SPADs), each roughly 50% efficient at this wavelength, we observe approximately 26,000 coincidence counts per second.

The waveguide-coupling apparatus, also depicted in figure 2.5, consists of a 40 $\times$  microscope objective that focuses the photons into the input side of the chip, lensed multimode fibers to collect them from the output side of the chip, and SPADs to detect them. We use a fiber-coupled adjustable delay line to ensure that both photons arrive at the chip simultaneously, which we verify by observing Hong–Ou–Mandel interference (Hong, Ou, and Mandel, 1987) as we vary the delay setting. We observe approximately 6% transmission through a circuit with 10  $\mu\text{m}$  DLSPWs and 3% transmission through one with 20  $\mu\text{m}$  DLSPWs.

We fabricate our interferometers on silicon chips using a combination of lithography, wet and dry etching, and thin film deposition techniques, which are described in more detail in (Fakonas et al., 2014). Briefly, we pattern the dielectric waveguides in 280 nm of silicon nitride on top of a 3  $\mu\text{m}$   $\text{SiO}_2$  lower cladding layer. Subsequent lithography, etching, deposition, and lift-off steps define recessed gold pads for the DLSPWs, followed by further lithography and metallization steps to create nickel-chromium heaters and gold contact pads. Two final lithography steps in 2.5  $\mu\text{m}$  and 350 nm PMMA cover layers define spot-size converters (Shoji et al., 2002) at the ends of the waveguides and the dielectric loads of the DSLPPWs, respectively. The completed DLSPWs consist of strips of PMMA 300 nm wide, 350 nm tall, and either 10 or 20  $\mu\text{m}$  long on top of gold pads of the same length.

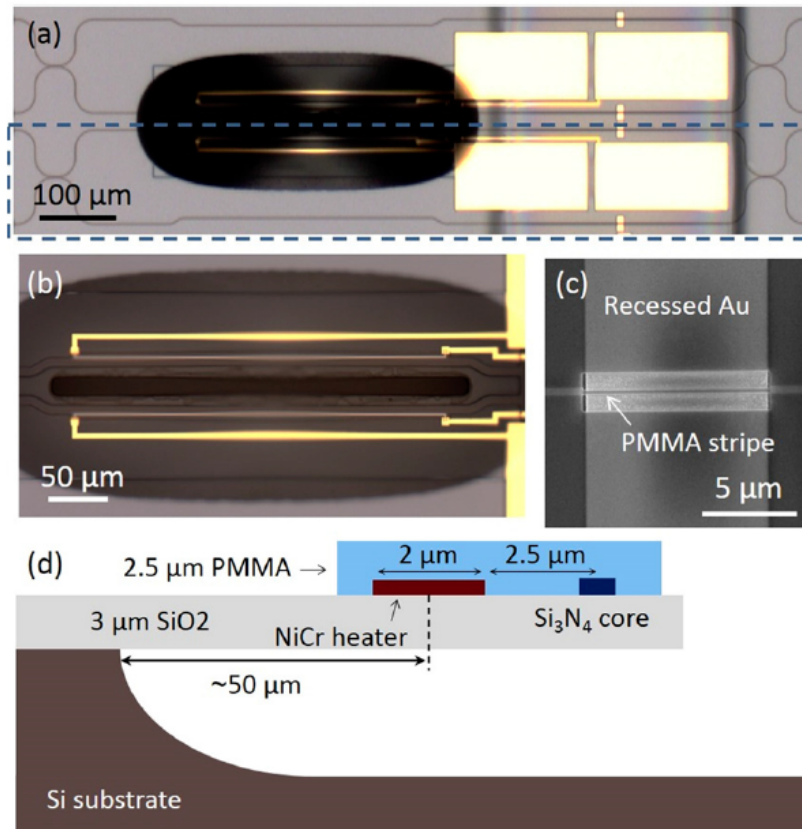


Figure 2.5: **The completed chip.** (a) Optical micrograph showing dielectric waveguides (thin dark lines), contact pads (large gold rectangles), DLSPPWs (small gold rectangles), and under-etched region (large dark oval). The two dark, vertical lines in the right half of the image separate the area covered with 350 nm of PMMA (between these lines) from that covered with  $2.5 \mu\text{m}$  of PMMA (everywhere else). The dashed box encloses a single interferometer with  $10 \mu\text{m}$  DLSPPWs, as represented schematically in figure 2.4. (b) Optical micrograph of the region where the silicon handle has been etched out from underneath the heaters and waveguides. The two light gray, horizontal lines connecting pairs of gold contacts are resistive NiCr heaters, while the long, dark oval between them is the hole through which the underlying silicon was etched. (c) Scanning electron micrograph of a  $10 \mu\text{m}$  DLSPPW. (d) Diagram showing a cross-section of the under-etched region.

Figure 2.5 shows the fabricated chip. Panel (a) depicts two complete interferometers, each with a pair of contact pads (large gold rectangles) and  $10 \mu\text{m}$  DLSPPWs (small gold rectangles, shown also in panel (c)). The large, dark oval near the center of the image is an area where the silicon underneath the waveguides has been etched away using  $\text{XeF}_2$  in order to thermally isolate the resistive heaters, which can be seen more clearly in panel (b). The diagram in panel (d)

sketches a cross-section of this part of the chip, showing the heater-waveguide separation and the approximate extent of the undercut. With this design, we need roughly 50 times less power to achieve a given phase shift than for a similar chip without the undercut.

The measurements themselves consist of two main steps. First, we set the heater power to give a phase shift of approximately  $\pi/2$  and record simultaneous counts at the detectors as a function of the adjustable delay setting. The resulting Hong–Ou–Mandel interference allows us to find the setting that corresponds to the simultaneous arrival of both photons at the first directional coupler. Second, we step the voltage across the heater from 0 to 3 V (roughly 0-5 mW), recording both one- and two-particle interference in the count rates of the SPADs. Specifically, at each step we: (1) block one of the inputs and record the count rate on each detector; (2) unblock the input and record the coincidence count rate; and (3) block the same input as before and record the separate count rates again to make sure they did not change substantially. Following this procedure allows us to observe single-particle ("classical") interference in the data with one input blocked and two-particle interference in the coincidence data.

Our raw data for the 10  $\mu\text{m}$  DLSPPWs are shown in figure 2.6(a). The top panel shows the count rate of one of the SPADs with one input blocked (i.e. one-particle interference), while the bottom panel shows the coincidence count rate with neither input blocked. Both signals oscillate, and it is clear that the latter does so at twice the frequency of the former. The oscillations are not sinusoidal, though, indicating that the phase shift caused by the heater does not depend linearly on the power supplied to it. We also note that the heater itself was quite stable, as its resistance, shown in figure 2.6(b), did not change by more than about 1% over the course of the measurement. Taking the thermo-optic coefficient of the silicon nitride to be  $2.45\text{e-}5$  (Arbabi and Goddard, 2013) and neglecting the contributions of the cladding materials, we estimate that the heaters increase the temperature of the neighboring waveguides by about  $70^\circ\text{C}$ .

From the single-particle interference in the top panel of figure 2.6(a), we calculate the phase shift that the heater produced at each power setting. The result is shown in figure 2.6(c). We then use this information to plot the coincidence data as a function of phase instead of heater power, as shown in figure 2.7(a). The data in this plot are the same as those in the bottom panel of figure 2.6(a), but here they are plotted as a function of the phase shift induced by the heater. The red curve

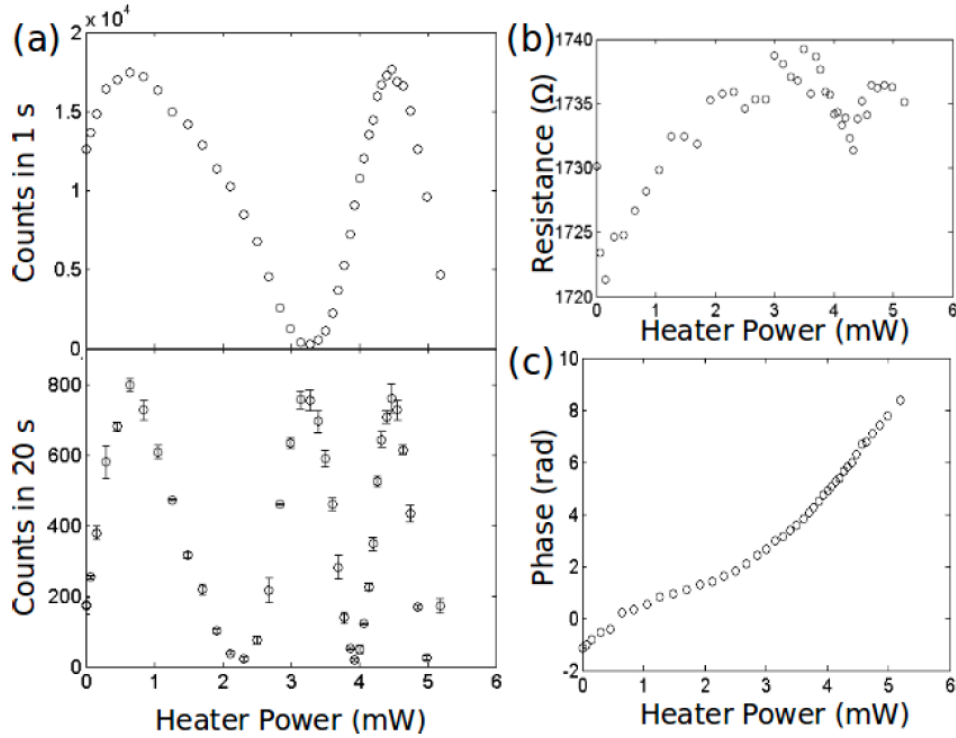


Figure 2.6: **Raw measurements on the interferometer that had  $10\ \mu\text{m}$  DLSP-PWs.** (a) Top: one-particle interference obtained by blocking one input of the interferometer and recording the count rate at one of the detectors. Bottom: two-particle interference obtained by counting coincidences with both inputs unblocked. Error bars indicate one sample standard deviation above and below the average, calculated from three trials. (b) Resistance of the NiCr heater plotted over its operating range, showing a maximum variation of about 1%. (c) Plot of the phase shift induced by the heater as a function of the power supplied to it, computed from the one-particle interference data. The first maximum of the interference data was taken to correspond to zero phase.

shows a sinusoidal fit with a period of  $\pi$ , confirming that the coincidence signal does indeed oscillate as expected from equation (2.30). Figure 2.7(b) shows the result of a similar measurement made in an interferometer with  $20\ \mu\text{m}$  DLSP-PWs, where we have applied the same method of analysis. The result is nearly identical to that in panel (a), indicating that increasing the length of the DLSP-PWs (and therefore the losses suffered) did not affect the degree of path entanglement.

The visibility of interference in these measurements is defined as

$$V = \frac{C_{\max} - C_{\min}}{C_{\max} + C_{\min}} = 1 - \frac{2C_{\min}}{C_{\max} + C_{\min}}, \quad (2.31)$$

where  $C_{\max}$  and  $C_{\min}$  are the maximum and minimum count rates observed as the

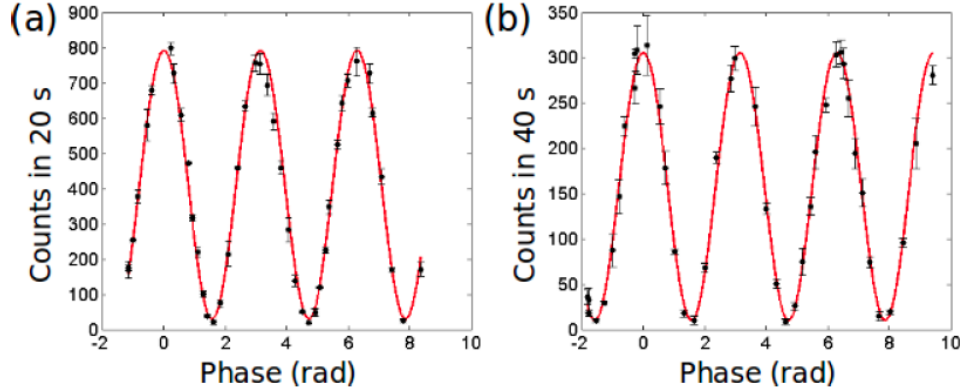


Figure 2.7: **Measurements of two-particle interference.** Results of interference in the interferometers with  $10\ \mu\text{m}$  (left) and  $20\ \mu\text{m}$  (right) DLSPWs showing clear path entanglement with visibilities of  $0.954 \pm 0.016$  and  $0.948 \pm 0.021$ , respectively. Each data point marks the average of three measurements, while the error bars represent one sample standard deviation above and below the average. The red curves are sinusoidal fits.

phase varies. In the interferometer with  $10\ \mu\text{m}$  DLSPWs we observe one-particle and two-particle interference with visibilities of  $0.974 \pm 0.005$  and  $0.954 \pm 0.016$ , respectively. In each of these calculations, we estimate the standard deviation of the visibility using the (measured) standard deviation of  $C_{\min}$ , taking  $C_{\max}$  to be constant because fluctuations in  $C_{\max}$  are proportionately much smaller than fluctuations in  $C_{\min}$ . In the circuit with  $20\ \mu\text{m}$  DLSPWs, we observe visibilities of  $0.972 \pm 0.007$  and  $0.948 \pm 0.021$  for one- and two-particle interference, respectively.

While the longer, higher-loss waveguides did not reduce the visibility of entanglement, they certainly reduced the overall transmission of light through the interferometers. As shown in figure 2.7, increasing the length of the DLSPWs by  $10\ \mu\text{m}$  reduced the coincidence count rate by roughly a factor of five, which is consistent with the observed drop in the single-particle signal by slightly more than a factor of two. In previous measurements (Fakonas et al., 2014), we estimated the  $1/e$  absorption length in similar waveguides to be roughly  $7\ \mu\text{m}$ , however, which suggests that the difference between losses observed in the  $10\ \mu\text{m}$  and  $20\ \mu\text{m}$  waveguides in the current experiment should have been larger. We suspect that the coupling of light into and out of the interferometer with  $20\ \mu\text{m}$  DLSPWs might have been slightly more efficient than for the interferometer with  $10\ \mu\text{m}$  DLSPWs, partially offsetting the extra absorption loss.

## 2.7 Conclusions

In conclusion, we observed path entanglement between surface plasmons with a visibility of approximately 95%. Moreover, doubling the length of the plasmonic waveguides did not have an effect on the visibility of entanglement. As a result, we conclude that the plasmons in our experiment did not interact strongly enough with the metal that sustained them — as by elastically scattering electrons or phonons, for example — to decohere the path-entangled state. Our findings suggest that surface plasmons propagating in the waveguides with "light-like" dispersion do not lose coherence due to elastic interactions with other electrons, phonons and surfaces. Similar conclusions about pure dephasing of surface plasmons propagating through hole array in an insulator-metal-insulator structure was drawn from experiment by (Tokpanov et al., 2019). However, in this experiment plasmon mode belonged to a more dispersive part of the plasmon dispersion curve. Thus, despite being extremely lossy, plasmonic structures can find applications in quantum computing technologies. Further investigations of microscopic mechanisms for pure dephasing of plasmons can be studied through the combination of experiment and density functional theory simulations.

The future work in this area might focus on overcoming high loss in plasmonic structures by loss compensation and gain. Several examples of surface plasmon polariton amplification and gain were reviewed in (Berini and Leon, 2012) at the classical level. It is yet to be determined how these techniques can be realised in quantum regime. Solving the problem of high plasmonic absorption would advance the development of integrated quantum photonics based on hybrid plasmonic and nanophotonic structures that take advantage of strong confinement of light. The fabrication techniques developed in this work might assist in integration of various quantum computing components on a single silicon based platform for linear optical computing.

*Chapter 3***DNA ORIGAMI COUPLED TO MOLECULAR EMITTERS**

DNA origami is a modular platform for the combination of molecular and colloidal components to create optical, electronic, and biological devices. Integration of such nanoscale devices with microfabricated connectors and circuits is challenging: large numbers of freely diffusing devices must be fixed at desired locations with desired alignment. We present a DNA origami molecule whose energy landscape on lithographic binding sites has a unique maximum. This property enables device alignment within  $3.2^\circ$  on  $\text{SiO}_2$ . Orientation is absolute (all degrees of freedom are specified) and arbitrary (every molecule's orientation is independently specified). The use of orientation to optimize device performance is shown by aligning fluorescent emission dipoles within microfabricated optical cavities. Large-scale integration is demonstrated via an array of 3,456 DNA origami with 12 distinct orientations, which indicates the polarization of the excitation light.

**3.1 Method of deterministic DNA origami placement with arbitrary orientation**

A large portion of the chapter I was dedicated to the discussion of scalable approaches to integration of hybrid components with widespread semiconductor manufacturing process. The method of directed DNA origami self-assembly stands out due to its versatility, reproducibility on a large scale and 5-nm precision. So far, we have discussed the absolute orientation of the DNA origami shape relative to the substrate and the freedom in choice of the orientation. Now, we will demonstrate how the design of the DNA origami shape and the design of the shape of its binding site can solve these challenges.

DNA origami placement match between the overall shape of an origami and lithographically patterned binding sites is used both to position the origami in  $x$  and  $y$ , and to control its in-plane rotation angle  $\theta$ . The advantage of DNA origami placement over other methods of directed self-assembly is that thousands of origami can be oriented with high yield and fidelity:  $\sim 95\%$  of sites have single origami aligned within  $\pm 10^\circ$  of a desired angle  $\theta$ . However, certain shapes of

DNA origami used in the previous works, like equilateral triangles, do not achieve absolute orientation and its use is limited to devices with compatible symmetry, e.g. point-like, threefold, or sixfold. DNA origami placement for equilateral triangles is depicted in the figure 3.2A.

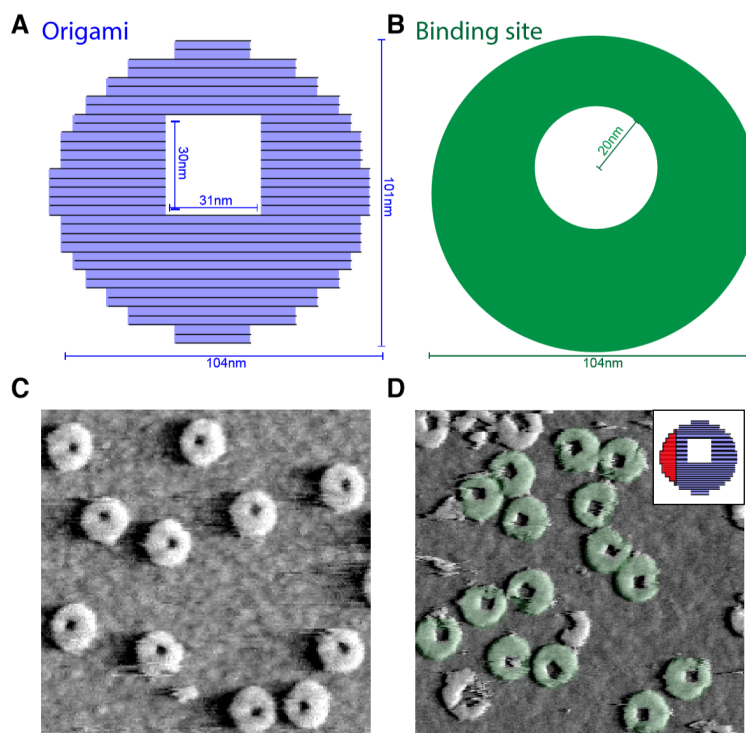


Figure 3.1: **Schematics and AFM for the death star origami.** (A) Dimensions of the death star origami. (B) Dimensions of the e-beam patterned binding site used for DNA origami placement of the death star origami. (C) AFM of death star origami on an unpatterned  $\text{SiO}_2$  surface. The staples of the death star origami are all modified with 20T extensions, but the symmetry of the death star prevents a determination of whether they are landing right-side up (with 20Ts up) or upside down. (D) AFM of a modification of the death star designed to help verify that death stars bind  $\text{SiO}_2$  right-side up. Inset shows a region of staples (red) which were omitted to break the  $D_1$  symmetry of the small moons. The resulting  $C_1$  shape allows discrimination based on which edge of the origami looks ragged or broken. Green shading indicates origami which were judged to be right-side up. Of 642 origami inspected, 95.6% (614) were found to be right-side up; 4.4% were found to be upside-down or their orientation could not be determined.

To solve this problem we have designed an origami with "moon-like" asymmetric shape that we called "death star". Geometrical parameters and atomic force microscope image are presented in the figure 3.1A and 3.1C, respectively. Figure 3.2B shows death star origami organizing with two indistinguishable orientations:

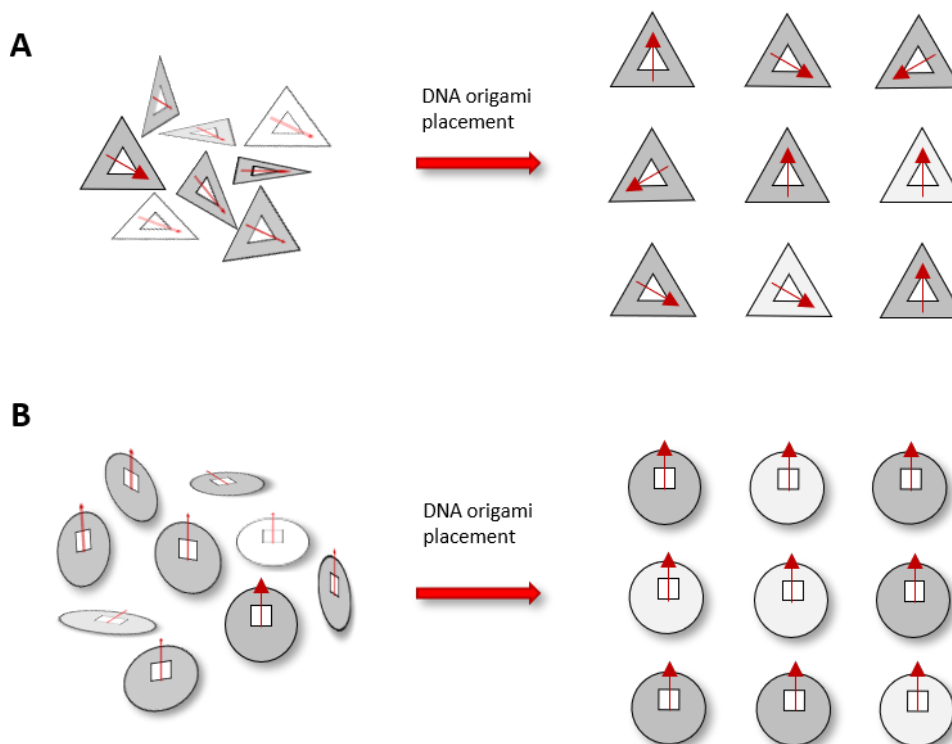


Figure 3.2: **DNA origami placement of shapes within different symmetry groups.** A. DNA origami placement of equilateral triangles does not allow aligning all origami in a certain direction. There are 3 possible orientations with right-side up and 3 orientation with right-side down. B. Asymmetric "moon-like" origami shapes can self-assemble with only two possible absolute orientations: right-side up and upside-down.

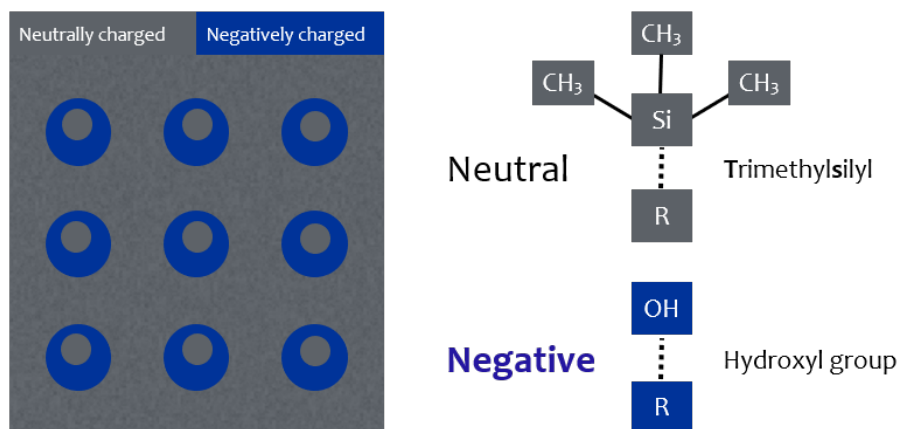


Figure 3.3: **DNA origami placement of death star origami.**

right-side up and upside-down. However, we proved that it is possible to break the symmetry by modifying DNA origami with 20T extensions on one side. Our idea

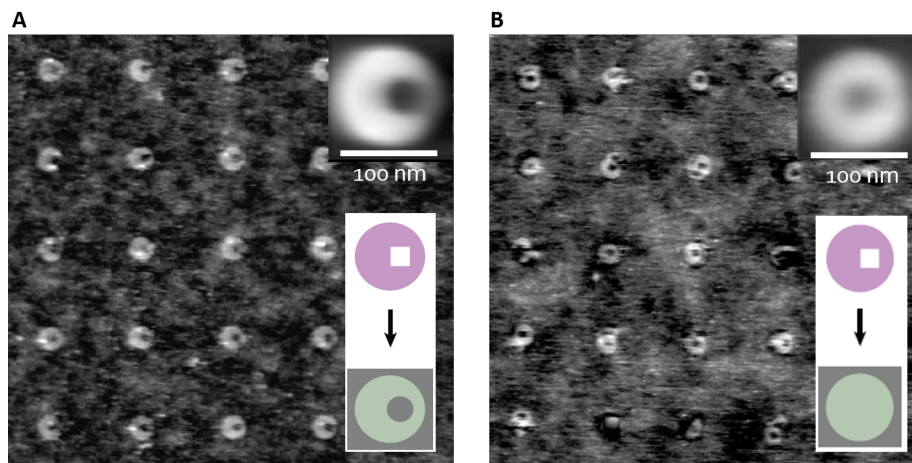


Figure 3.4: **DNA origami placement of death star origami.** Averaged AFM (N=600) of DNA origami placement on arrays of A: small moon sites, B: disk-shaped sites.

was to make one side of the origami non-sticky and hence bias binding, through the addition of single-stranded (ssDNA) 20T extensions to the 5' ends of staples. To distinguish orientation with right-side up, we modified the shape of death star by "cutting off" one side of the circle. Practically, this modification was done by removing staples on the left side of the origami. AFM images of modified death stars presented in figure 3.1 and orientations with right-side up are colored in green. Of 642 origami inspected, 95.6% (614) were found to be right-side up; 4.4% were found to be upside-down or their orientation could not be determined.

Here we show how absolute orientation can be achieved by DNA origami placement with death star DNA origami shapes, and demonstrate two applications in which absolute and arbitrary orientation work together to optimize or integrate optical devices.

DNA origami placement can be performed on any planar substrate (e.g. SiO<sub>2</sub>, quartz, silicon nitride [SiN], gallium phosphate [GaP] and diamond-like carbon) whose surface can be differentiated into negatively charged binding sites (blue colored in the figure 3.3) which bind negatively charged DNA origami strongly in the presence of bridging Mg<sup>2+</sup> ions, and a neutral background which binds origami weakly (gray colored in the figure 3.3). In our experiments e-beam patterned binding sites are made negative via silanols which are ionized at the pH (8.3) of the origami binding buffer and the neutral background is a trimethylsilyl monolayer, generated via silanization (see figure 3.3). DNA origami placement is a complex adsorption

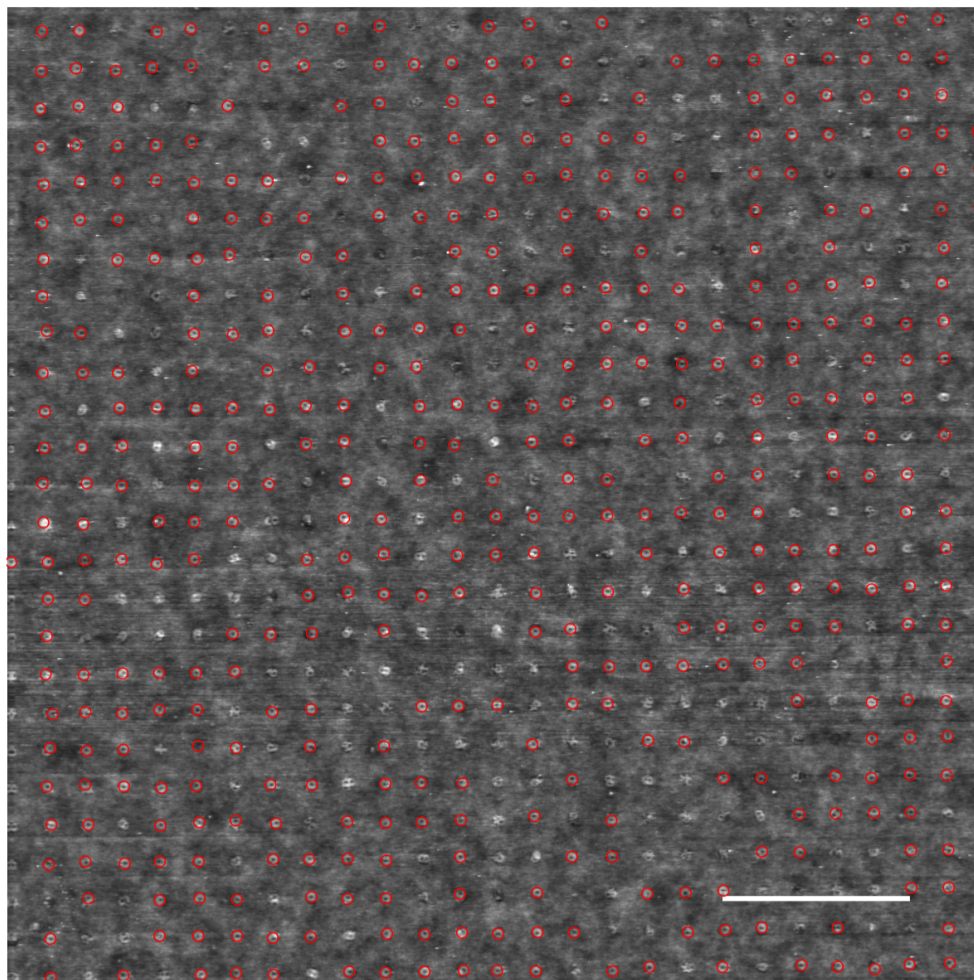


Figure 3.5: **Annotated AFM of small moon origami placed on square array of 105 nm diameter disk-shaped binding site.** Scale bar,  $2 \mu\text{m}$ . Red circles indicate single origami binding events (at 83% of 600 sites) which were cut out automatically and averaged to yield annular image in figure 3.4B.

process which involves both 3D diffusion to the surface, and 2D diffusion of weakly bound origami on the background. To achieve absolute orientation of death star origami we have designed a binding site with a shape similar to the death star origami shape. We call this shape "small moon" and it is depicted in the figure 3.1B.

DNA origami placement of death star origami with ssDNA extensions to break up-down symmetry was performed on both disk-shaped control sites (figures 3.4B and 3.5) and small moon sites (figures 3.4A and 3.6). The average of 498 AFM images of control sites with single origami (83% of 600 total sites) gave an annular shape indicating random orientation; the average of 592 images on small moon sites (98.7% of 600 total sites) reconstruct the death star shape, confirming unique

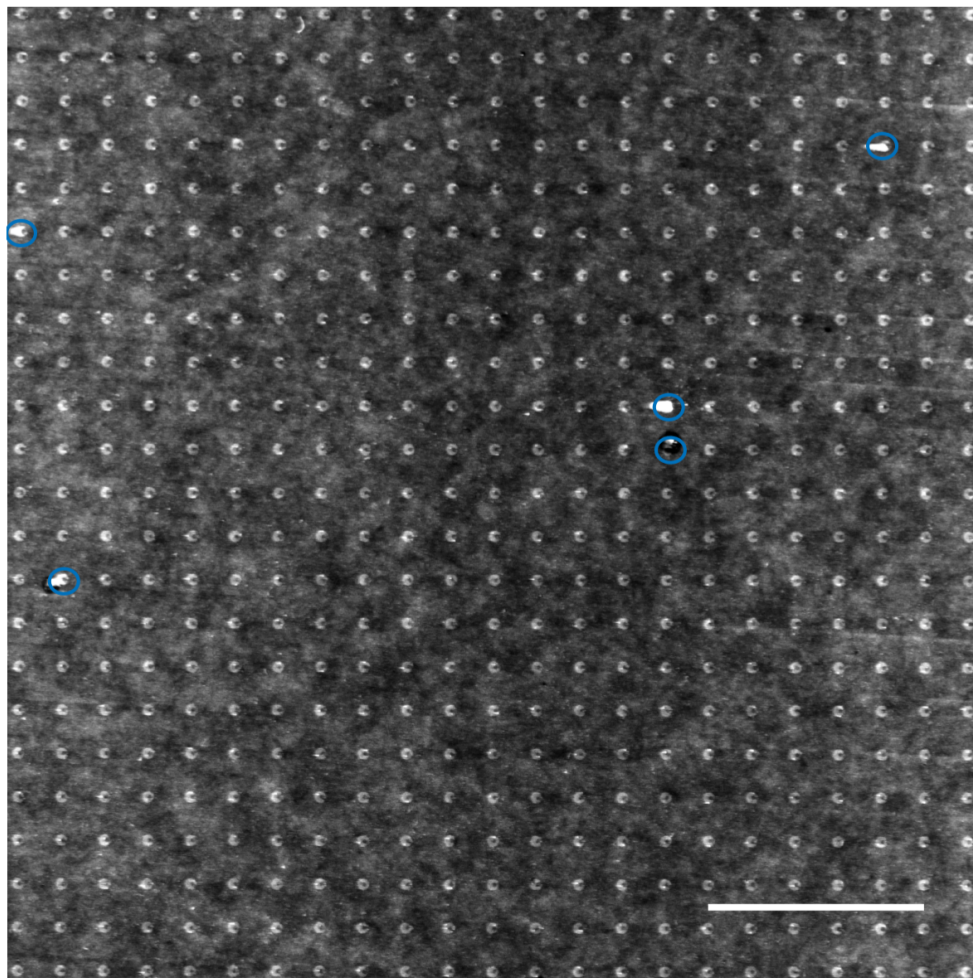


Figure 3.6: **Annotated AFM of death star origami placed on a square array of small moon binding sites.** Scale bar,  $2\mu\text{m}$ . Blue ovals indicate which sites were not analyzed. The remaining 592 sites (98.7% of 600 total sites; only 529 sites are shown) were cut out and averaged to yield the reconstruction of the death star in figure 3.4A. Orientation of each death star was automatically extracted and they were found to be oriented to  $0^\circ \pm 6.7$  degrees. We suggest that the discrepancy between this orientational fidelity, and that measured optically ( $\pm 3.2^\circ$ ) can be explained by a poorer ability to measure the orientation of small moons from AFM data, which are noisy and have apparent salt artifacts (see white dots on origami).

alignment. By fitting the death star shape to AFM of death star origami on small moon sites, we found that alignment varied by  $\pm 6.7^\circ$  ( $\pm 1$  SD). This variability includes both real variability due to fabrication error or imperfect assembly, and spurious variability due to the fitting of a model shape to poorly resolved origami; the latter error is difficult to estimate.

To get a better estimate of alignment precision, we imaged death star DNA

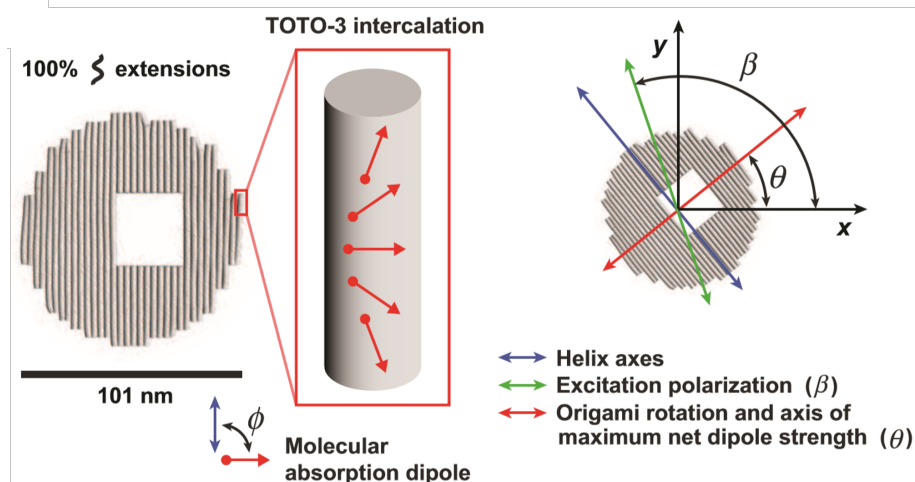


Figure 3.7: **Death star intercalation by TOTO-3 fluorescent molecule.** Rotation of the fluorescent dye TOTO-3's absorption dipole along the length of a TOTO-3 intercalated helix. Coordinate system shows relationships between helix axes, excitation polarization ( $\beta$ ) and origami rotation ( $\theta$ ).

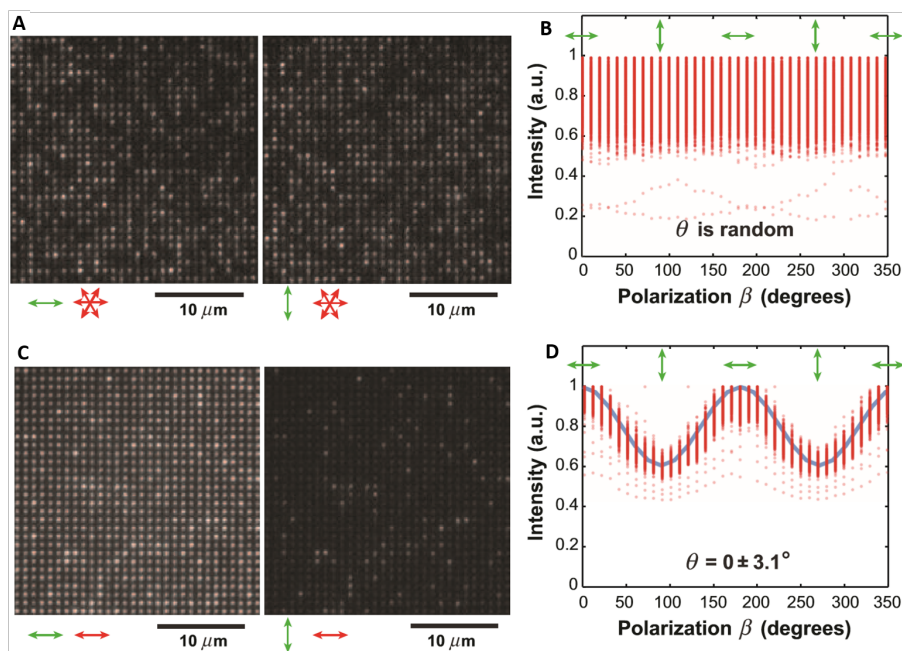


Figure 3.8: **Fluorescence microscopy of TOTO-3 intercalated into DOP arrays on disk-shaped and shape-matched sites (ex. 642 nm; em. 660 nm).** Fluorescence microscopy of TOTO-3 intercalated into DOP arrays on disk-shaped and shape-matched sites (ex. 642 nm; em. 660 nm). A and C Intensity (red dots) of  $N=600$  sites in B and D as a function of excitation polarization. Blue line, best fit.

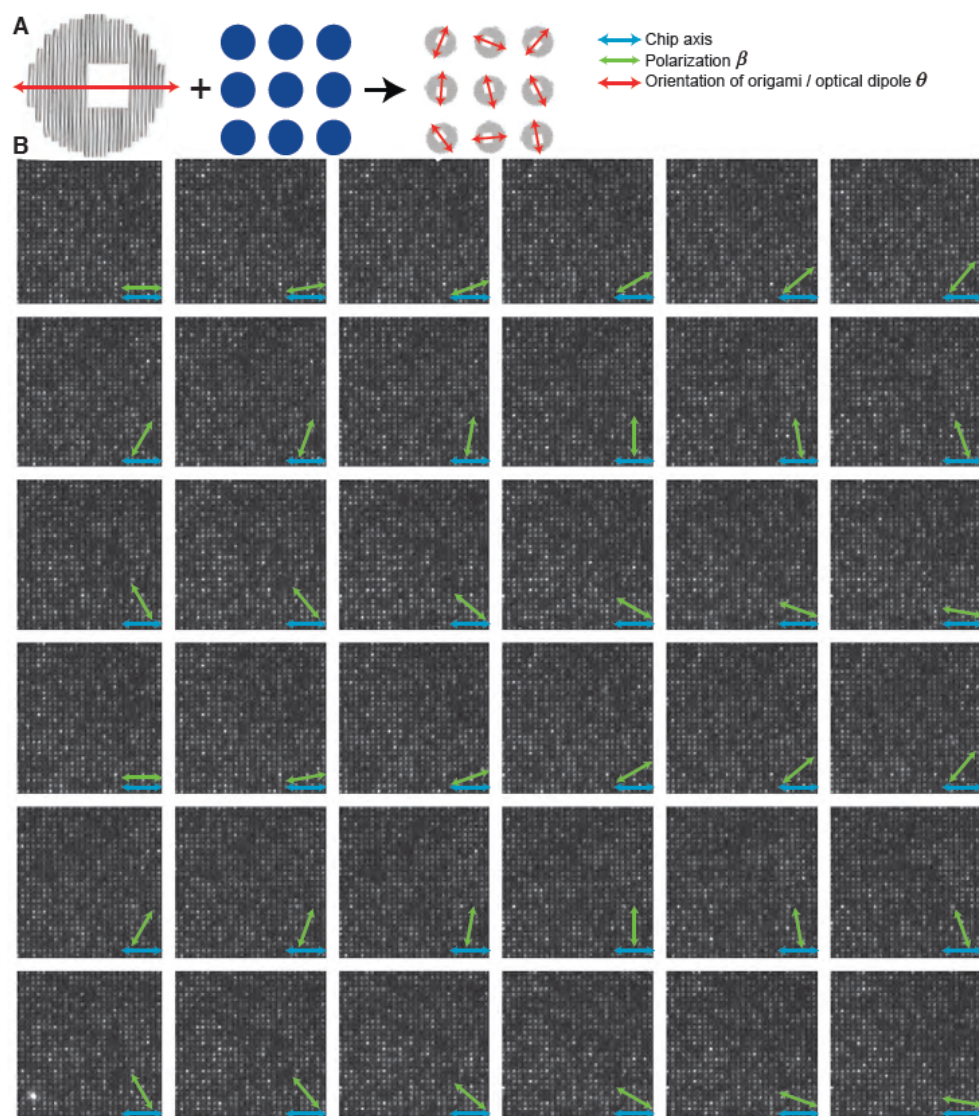


Figure 3.9: **Schematic and raw fluorescence data for death star origami placed on a  $1\ \mu\text{m}$  period square array  $105\ \text{nm}$  diameter disk-shaped binding sites.** A: Schematic indicates that death star origami will bind with random orientations and the excitation dipoles of intercalated TOTO-3 fluorophores will be uncontrolled. B: 36 images show the rotation of excitation light polarization (green) relative to the array axis (blue) in  $10^\circ$  increments. Variations in the intensity of death star origami are uncorrelated.

origami intercalated post-placement with the fluorescent dye TOTO-3 (figure 3.7). For 600-site arrays of small moons on disk-shaped control and shape-matched sites, we measured emission intensity for excitation polarization  $\beta$  in  $10^\circ$  steps (sampling each  $\beta$  twice by rotating the stage from  $0^\circ$  to  $350^\circ$ ) and fit the emission to derive distributions for the origami orientation  $\theta$ . The reported angle between the molecular

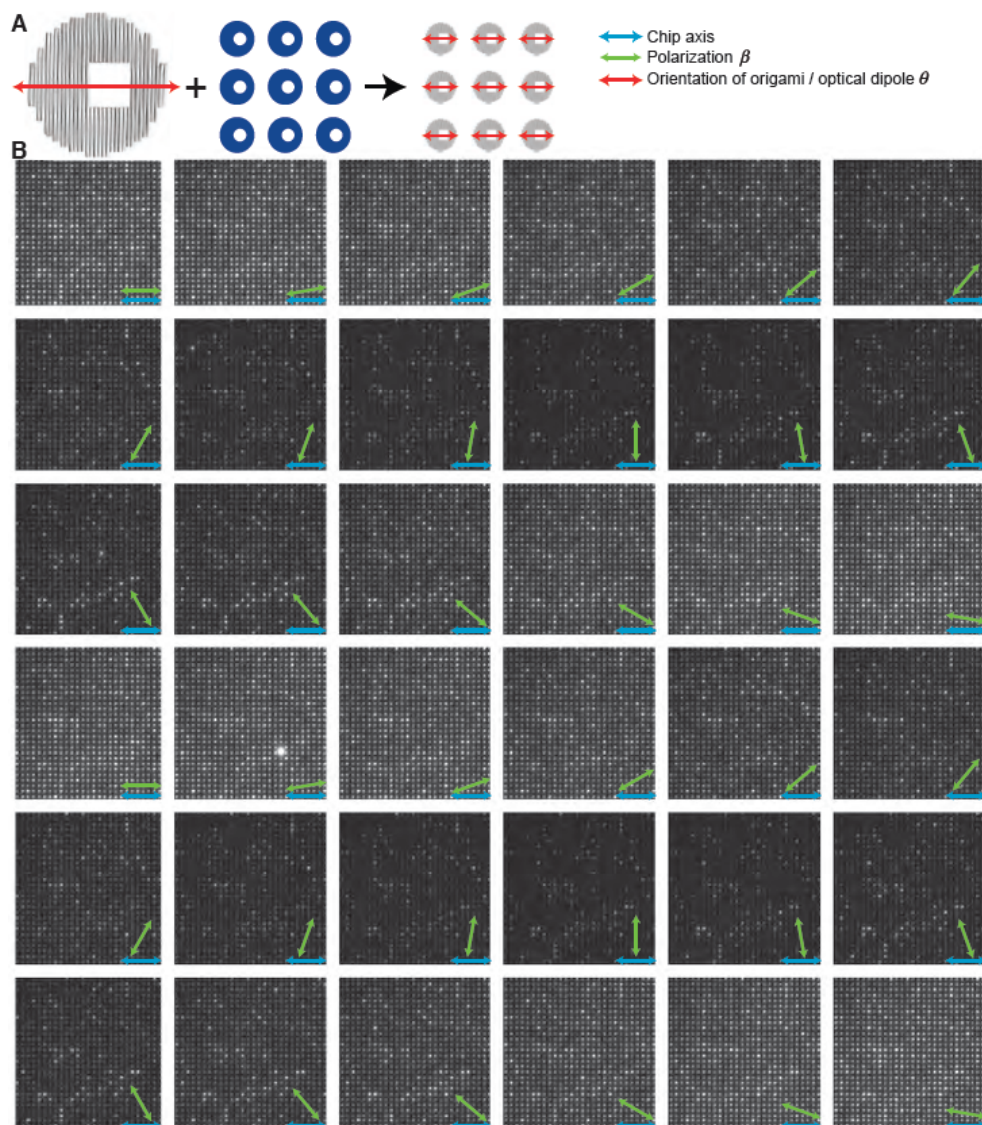
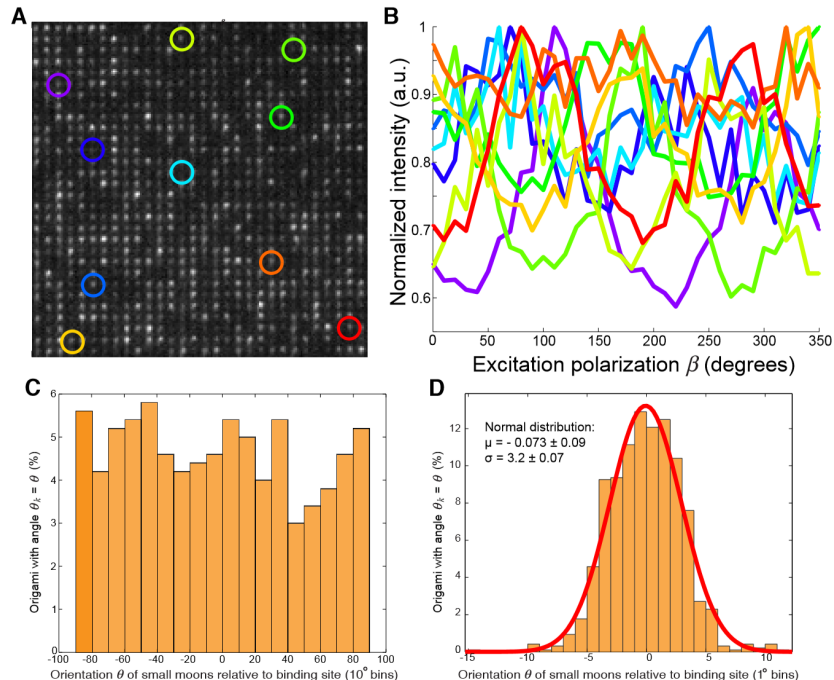


Figure 3.10: **Schematic and raw fluorescence data for death star origami placed on a  $1 \mu\text{m}$  period square array of small moon binding sites.** A: Schematic indicates that death star origami will align to the binding sites and in turn align the excitation dipoles of intercalated TOTO-3 fluorophores. B: 36 images show the rotation of excitation light polarization (green) relative to the array axis (blue) in  $10^\circ$  increments. Variations in the intensity of death star origami are highly correlated, and small moons are brightest when the polarization axis lines up with the array axis.

absorption dipole of TOTO-3 analogs and the DNA helix axis ( $\phi$ ) ranges from  $61^\circ$  to  $90^\circ$  (Spielmann, Wemmer, and Jacobsen, 1995), (Schins et al., 1999), but the exact angle is unimportant for measuring variability: it is close enough to  $90^\circ$  that averaging over multiple dyes (intercalated at varying rotations due to twist) results in



**Figure 3.11: Analysis of orientation based on fluorescence data.** A: A subsection of data presented in figure 3.9, TOTO-3 labelled death stars bound to disk-shape binding sites. Ten particular binding sites are highlighted with differently colored circles. B: Traces of fluorescence intensity from ten binding sites highlighted in A, as a function of the orientation of excitation polarization  $\beta$ . All of the  $k = 1$  to 600 individual traces can be fit to  $I_0 \cos^2(\beta - \theta) + c$ . C: Histogram of  $\theta_k$  aggregated into  $10^\circ$  bins shows that the  $\theta_k$  are randomly distributed and that death stars exhibit no preferential orientation on disk-shaped sites. The flat histogram further suggests that the excitation polarization is that intended, and that the experimental setup introduces no undesired anisotropy. D: Histogram of  $\theta_k$  aggregated into  $1^\circ$  bins for data from figure 3.10, the binding of small moons to shape-matched binding sites.  $\theta_k$  cluster around  $0^\circ$  with a standard deviation of  $3.2^\circ$ .

a strongly anisotropic net dipole strength in the plane of the origami. Consequently, emission peaks for  $\beta$  perpendicular to the helix axes (Persson et al., 2009), coincident with  $\theta$ .

The strength of a molecular dipole  $\vec{\mu}$  excited by an electric field  $\vec{E}$  along the direction of unit vector  $\hat{e} = \frac{\vec{E}}{|\vec{E}|}$ , is:

$$P(\vec{E}) = |\vec{\mu} \cdot \hat{e}|^2 = |\vec{\mu}|^2 \cos^2(\beta - \theta),$$

where  $\beta$  is the polarization of  $\vec{E}$ , and  $\theta$  the in-plane dipole angle. According to the dipole approximation (Sick, Hecht, and Novotny, 2000), (Ha et al., 1999), emission

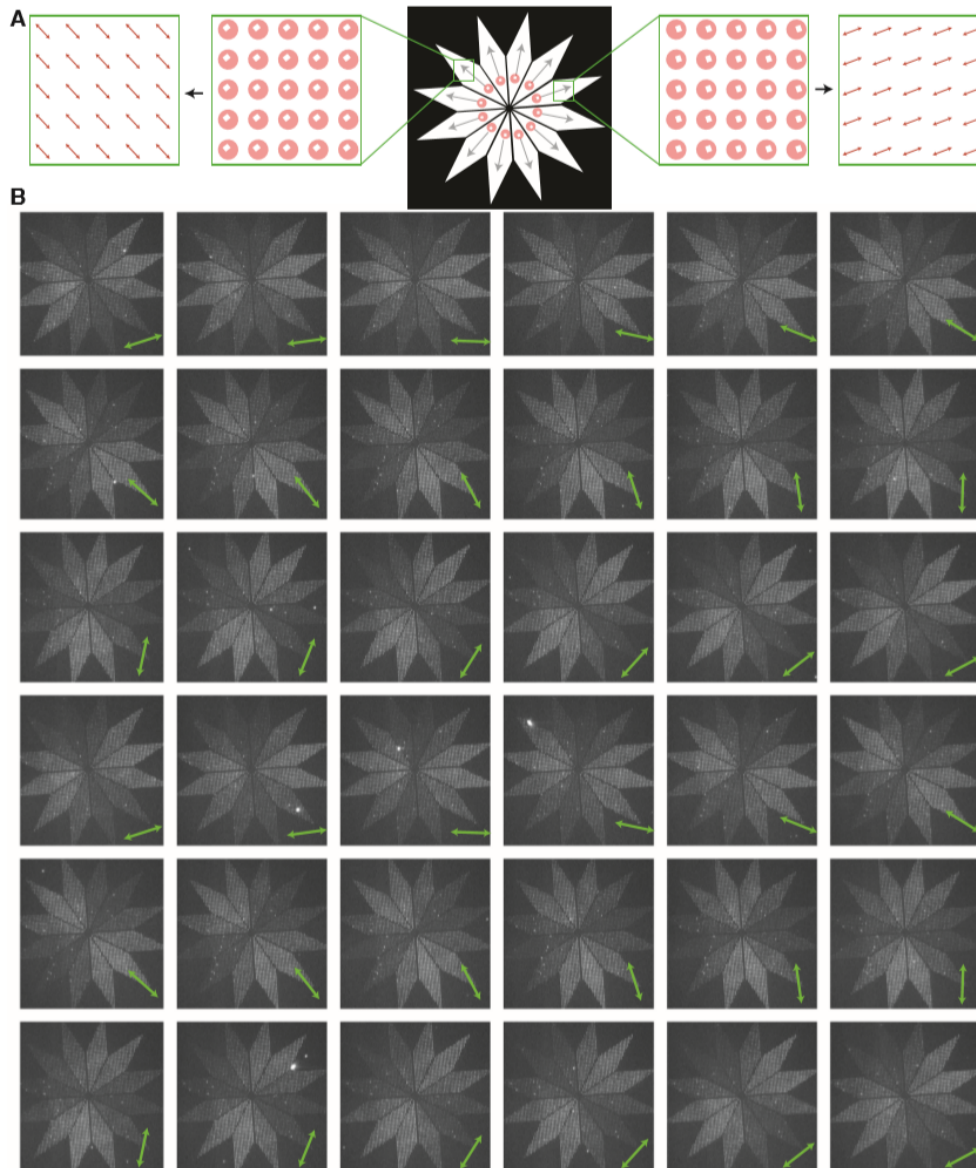


Figure 3.12: **Design and raw data for the polarimeter.** A: Design shows the orientation of small moon origami in each of the 12 rays of the polarimeter. DNA helices are perpendicular to the ray and so the excitation dipole of intercalated TOTO-3 is aligned parallel to the ray. B: 36 images of the polarimeter under polarized illumination; green arrows indicate axis of polarization.

is proportional to absorption, which is proportional to  $|\vec{E}|^2 P(\vec{E})$ . Thus experimental intensity can be fit to:

$$I(\beta) = I_0 \cos^2(\beta - \theta) + c,$$

where  $I_0$  is the maximum emission, and  $c$  is the background (camera noise, reflec-

tion). Emission from a collection of  $n$  molecular dipoles  $\vec{\mu}_k$  bound to an origami is proportional to  $|\vec{E}|^2 P_{\text{net}}$ , where the net dipole strength is given by

$$P_{\text{net}}(\vec{E}) = \sum_{k=1}^n P_k = |\vec{\mu}_k \cdot \hat{e}|^2.$$

Thus the experimental intensity of  $n$  molecular dipoles with an anisotropic net in-plane dipole strength can be fit to the  $\cos^2$  expression above: if  $\vec{E}_k$  and  $\theta$  are defined to lie along the direction of maximum net dipole strength, then  $I_0$  is proportional to the difference:

$$P_{\text{net}}(\vec{E}_{\parallel}) - P_{\text{net}}(\vec{E}_{\perp})$$

and  $c$  is the background plus a contribution proportional to  $P_{\text{net}}(\vec{E}_{\perp})$ , from the direction of smallest net dipole strength.

Emission from control sites (figures 3.8B, 3.11) individually fit this expression but individual  $\theta$  were uniformly distributed (figure 3.11C), both confirming random origami orientation and ruling out polarization anisotropy in our setup. As expected, aggregate data could not be fit. In contrast, aggregate data for shape-matched sites (3.8D) fit  $\theta = 0^\circ$  and fits to individual sites (figure 3.11D) vary by  $\pm 3.2^\circ$ , our best estimate of alignment precision.

Despite the limitations of intercalating dyes, figure 3.12 shows that arbitrary orientation can integrate 3,456 TOTO-3 labelled small moons with 12 different  $\theta$  into a microscopic fluorescent polarimeter, a  $100 \mu\text{m}$  device which glows most strongly along the polarization axis of incident light. The goal of microscopic polarimeters constructed on-chip instruments is to replace multiple bulky and expensive optical components and to make insitu measurements possible, within devices or transmission lines. Since our polarimeter reports polarization directly, it could be fabricated on microscope slides and used in situ to aid polarized fluorescence microscopy.

### 3.2 DNA origami functionalization with Eu ions

In the first chapter we have discussed a number of experiments that involved positioning of single-photon emitters with nm precision within optical cavities. In the majority of those works, single organic dye molecules were used as single-photon emitter of choice. Organic dye molecules such as Cy5 or ATTO are bright emitters and can be easily attached to DNA single strand and incorporated into the surface of DNA origami. However, due to the bleaching of organic dyes and very high dephasing rates they have limited number of applications for quantum computing. With this in mind, we have turned our efforts to alternative molecular emitters such as chelated lanthanide ion compounds. Chelated complexes increase absorption rate of metallic ions and thus fluorescent rate is higher especially for 3+ oxidation state.

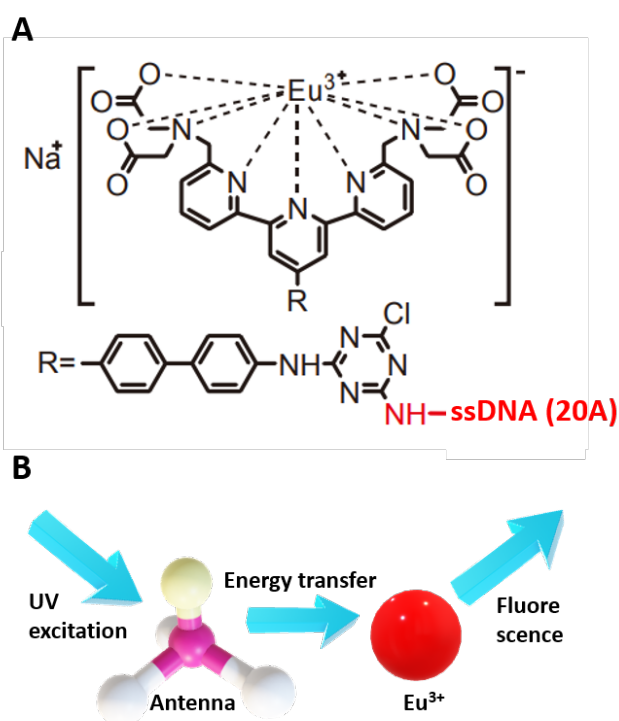


Figure 3.13: **Mechanism of fluorescent emission from europium compound.** A: Chemical formula of europium chelate complex labelled by single-stranded DNA. B: Chelated europium ion is attached to sensitizer molecule that absorbs light at wide range of UV wavelengths. This energy is transferred to Eu ion which later emits fluorescent light at 616nm.

Here we use a fluorescent europium ion labelling reagent from TCI chemicals that was modified and attached to ssDNA. The maximum of emission for this compound as specified by the company is 334 nm and fluorescence emission peak is at

616 nm with lifetime of 1.2 ms. These europium ion complexes have large absorption cross-section in UV due to a sensitizer molecule then excitation is transferred to chelated europium ion through electric transfer 3.13B.

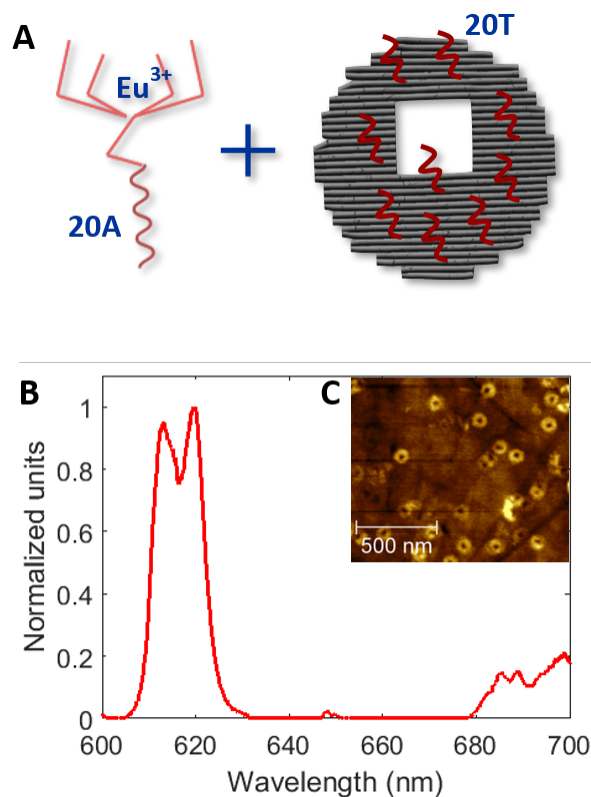


Figure 3.14: **DNA origami labelled by Eu ions.** A: Eu ion chelated complexes were labelled by 20A DNA strands and attached to death star origami with 20T extensions via different procedures. B: Measured spectra of Eu ions immobilized on the  $\text{SiO}_2$  substrate via DNA origami covalent bonding to the surface at room temperature. C: AFM image of death star origami labelled by Eu ions.

Due to extremely long fluorescence lifetime of excited chelated Eu ions, detection of a single photon emitted by europium is very challenging. We wanted to realize two strategies for increasing emission: enhancement of emission by precision placement inside an optical cavity and coherent coupling of several emitters located within the volume  $\lambda^3$ , where  $\lambda$  is the wavelength of emission (Dicke's superradiance, (Dicke, 1954)). The former approach will be discussed in the next chapter and the later - in this section. As was mentioned in the introductory sections, DNA origami can serve as a breadboard for various molecular components, each one separated by 3-6 nm from each other. Death star origami in particular could be functionalized with up to 235 20T ssDNA extensions that can bind to Eu ions labelled to 20A. This

enables to incorporate  $^{232}\text{Eu}$  ions individually separated by 3-6 nm within surface area of  $100^2\text{ nm}^2$ . Provided coherent interaction between emitters, this geometrical distribution satisfies condition for Dicke's superradiance.

Figure 3.14A presents a schematics of coupling Eu ions labelled to a single 20A ssDNA to death star origami with several 20T extension. Eu ions were added to DNA origami staples mixture and a scaffold before annealing of DNA origami. Afterwards, DNA origami were filtered through 100 kDa Amicon spin filter and immobilized on an oxygen plasma treated  $\text{SiO}_2$  surface using a standard DNA origami placement protocol (see Appendix A). The room-temperature emission spectra under 375nm pulsed laser excitation reveal a double peak at approximately 620nm which is expected from the specifications given by commercial company that synthesized the compound 3.14B. However, the number of Eu ions in this experiment is random and defined by the number of DNA origami in the area illuminated by the excitation laser.

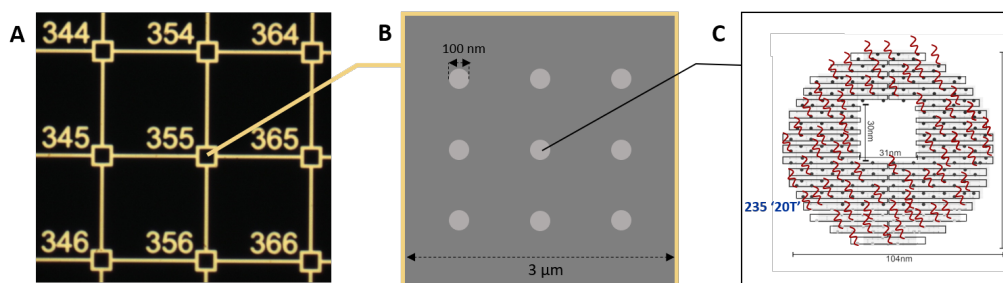


Figure 3.15: **Samples for DNA origami arrays.** A: Image of a sample with gold grid lines and labelled squares under white light illumination in a microscope. B: A single 3 by 3 array of disk-shaped DNA origami binding sites fabricated inside a gold frame of a labelled square. C: Death star DNA origami modified with 235 20T ssDNA extensions.

To have a precise count on Eu ions located in a defined area on the substrate, we prepared samples with lithographically defined binding sites for death star origami. Figure 3.15A shows grid lines fabricated using metal lift-off process and labelled squares with  $3\ \mu\text{m}$  size which are visible and easily identifiable by a camera used to assist in AFM imaging. Each square, as depicted in the figure 3.15B, has an array of disk-shaped binding sites for death star origami. Such design of the samples enables to image an array of DNA origami inside a certain square using AFM tip and then take optical measurements from the same squares, since all the squares on the sample are labelled with a unique number.

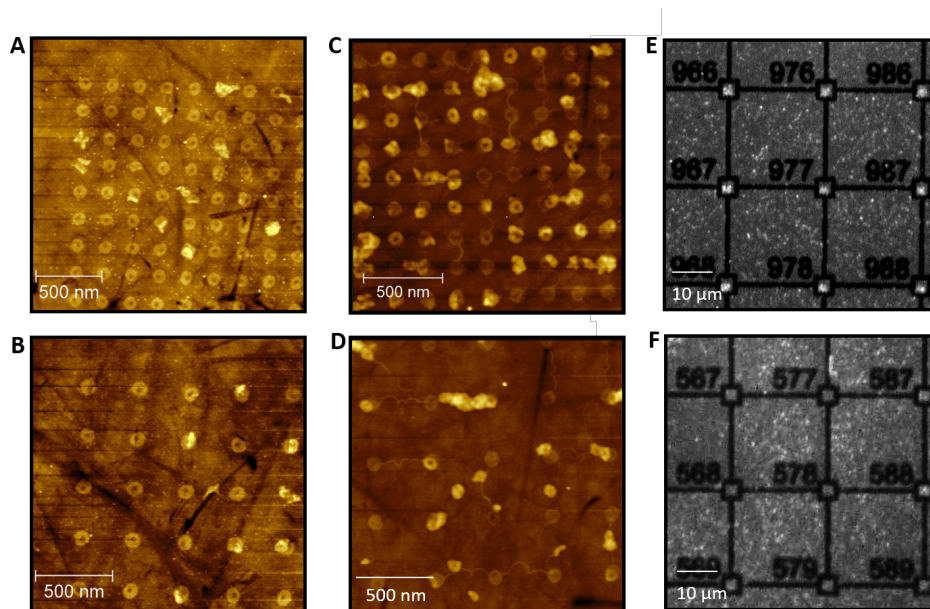
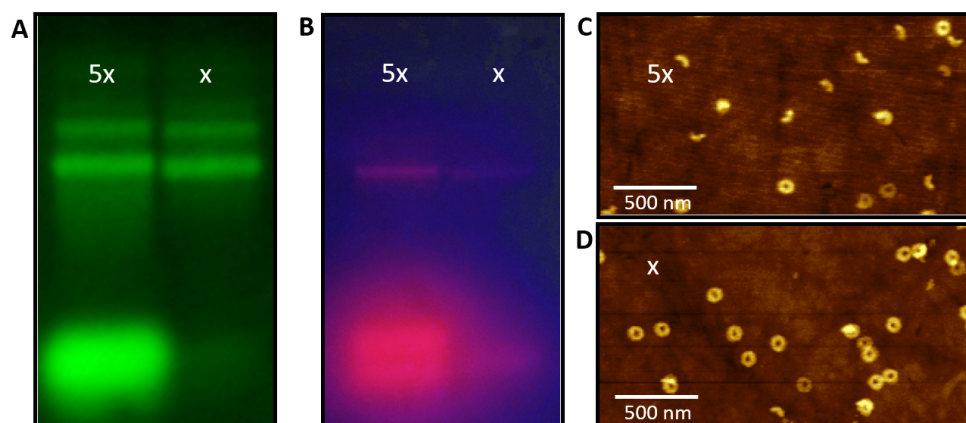


Figure 3.16: **DNA origami placement of death stars labelled by Eu ions.** A: An AFM image of a 9 by 9 array of unmodified death star. B: An AFM images of a 5 by 5 array of unmodified death star. C: An AFM image of a 9 by 9 array of death star origami modified with 235 20T extensions and linked to Eu ions. D: An AFM image of a 5 by 5 array of death star origami modified with 235 20T extensions and linked to Eu ions. E-F: Epifluorescence image of a grid with arrays of death star origami labelled with Eu ions under UV excitation light with emission filtered at 620 nm. E: 9 by 9 array of death star origami modified with 235 20T extensions and linked to Eu ions. F: 5 by 5 array of death star origami modified with 235 20T extensions and linked to Eu ions.

The results of the first set of placement experiments with DNA origami labelled with 235 Eu ions are presented in figure 3.16C-F. For the reference a similar sample for prepared via DNA origami directed self-assembly with unlabelled death star origami is shown in the figure 3.16A-B. If you compare AFM images of two arrays with the same density of origami in the figure 3.16 A against C and B against D, you can notice significant reduction in the quality of placement (percentage of sites occupied by exactly one origami and the number of origami attached to the background). Indeed, this is reflected on the optical measurement of fluorescence from DNA origami arrays labelled by Eu ions (figure 3.16E-F). The fluorescent emission from Eu was collected by 100x microscope objective after being filtered out from the UV excitation light by a bandpass filter. You can clearly observe more light coming out from inside the 9 by 9 arrays of origami (figure 3.16E).

However, emission from 5 by 5 arrays (figure 3.16F) is largely overwhelmed by the background emission coming from non-specifically bound origami even for long acquisition times.



**Figure 3.17: Death star DNA origami with 235 20T extensions.** A: Post stained electrophoresis gel imaged in the channel of SYBR gold fluorescence. B: Prior to staining electrophoresis gel imaged by cell phone camera. C: AFM image of sample with 5 times higher concentration of Eu labelled ssDNA. D: AFM image of sample with lower concentration of Eu labelled ssDNA.

To find out what happens to death star origami modified with 20T extensions when Eu ions linked to 20A are introduced into the solution phase, we ran gel electrophoresis for two samples with different stoichiometry between DNA origami scaffolds and 20A linkers labelled with Eu ions. Figure 3.17A presents a gel post-stained with SYBR gold intercalating dye with the left lane occupied by a sample with five times as many Eu labelled linkers as the sample in the right lane. The ratio between available 20T extensions and Eu 20A linker was 1:10 for the left sample and 1:2 for the right sample. These extra 20 A linkers in the sample "5x" are not incorporated into the DNA origami, which is reflected by the lowest band in the figures 3.17A and 3.17B which is formed by "light" ssDNA staples and linkers that are in excess to DNA origami that can travel longer in a gel. The second from the bottom band corresponds to a single DNA origami and the third from the bottom band corresponds to DNA origami dimers, which are identified by imaging the sample in the AFM. In the SYBR gold channel samples "5x" and "x" do not have significant differences, however the difference becomes apparent if we look at the unstained gel under UV excitation which is able to excite Eu ion complexes (figure 3.17B). The right band is less bright than the left band which tell us that not all the available extensions are linked to Eu ion 20A label. Furthermore, the samples with

Eu labelled DNA origami were immobilized on the SiO<sub>2</sub> substrate and dried using consecutive submerging into ethanol solutions with decreasing ratios of ethanol. The AFM image depicted in the figure 3.17C revealed an unexpected result: more than the half of origami had a different shape. They looked like death stars folded in half along the seam running through the middle of the origami shape. We have called this shape transformation "taco" due to resemblance to the famous Mexican street food. We think that this happens when 20A linkers bind to 20T extensions from different parts of origami, bringing 2 opposite ends of the origami surface together and folding origami. Since they bind only partially, for example, 10T from one side of origami to 20A linker and to 10T from the other side of the same origami, this shape is not stable in solution and can be flattened by strongly charged surface such as gold and mica. We also speculate that these folded shapes of DNA origami are unstable and cause aggregation over prolonged periods of time. AFM image from the second sample with lower concentration of 20A linkers appears to have significantly fewer tacos (3.17D). However, this sample has equal amounts of DNA origami dimers (second origami band in the gel in the figure 3.17A). Dimers can be distinguished in the AFM images by having double the height as a single origami, thus, they look like brighter death stars. For all the above mentioned reasons, we get significant nonspecific binding to background for DNA origami with 235 20T extensions and for origami with 235 Eu ions.

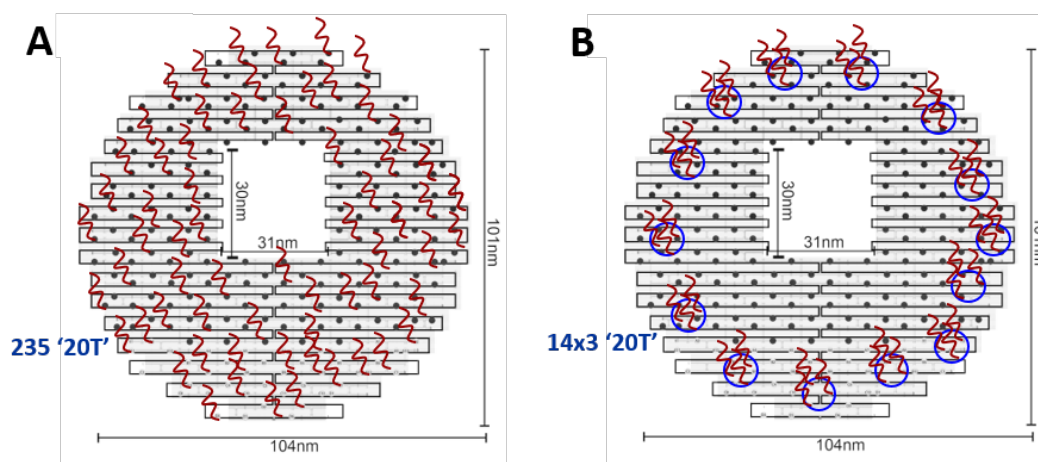


Figure 3.18: **Death star DNA origami with 20T extensions.** A: Death star DNA origami with 235 20T extensions. Every staple that forms death star origami shape was modified by adding 20T to its sequence. B: Death star DNA origami with 42 20T extensions formed by 14 clusters of 3 20T extensions located at the circumference of the disk.

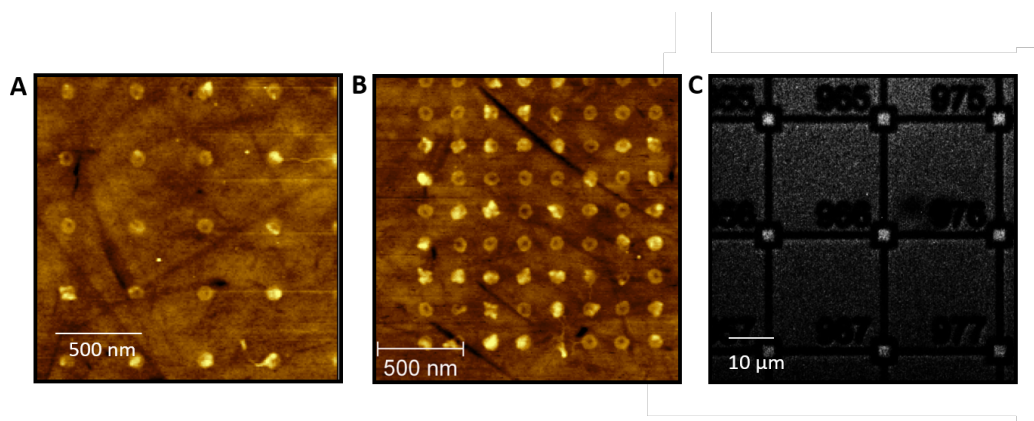


Figure 3.19: **Death star DNA origami with 42 20T extensions.** A: An AFM image of a 5 by 5 array of death star origami modified by 42 20T extensions and linked to Eu ions. B: An AFM image of a 9 by 9 array of death star origami modified with 42 20T extensions and linked to Eu ions. C: Epifluorescence image of a grid with 9 by 9 arrays of death star origami labelled with 42 Eu ions under UV excitation light with emission filtered at 620 nm.

By changing the number of 20T extensions on a single death star as displayed in the figure 3.18 we have identified a maximum number of Eu ions per origami that gives us consistent placement results. AFM images of placed DNA origami arrays in figures 3.19A and 3.19B are similar to arrays achieved with "bare" death star origami without any extensions. Figure 3.19C obtained from epifluorescence microscope shows emission these from 9 by 9 Eu labelled origami arrays from inside the  $3 \mu\text{m}$  squares with significantly reduced background compared to origami labelled with 235 Eu ions in figure 3.16E. For DNA origami labelled with even smaller numbers of Eu ions (15 and 3), we observed similar results for DNA origami placement on substrates, both on quartz slides and on silicon chips.

### 3.3 Interaction of single-stranded extensions with substrates and each other

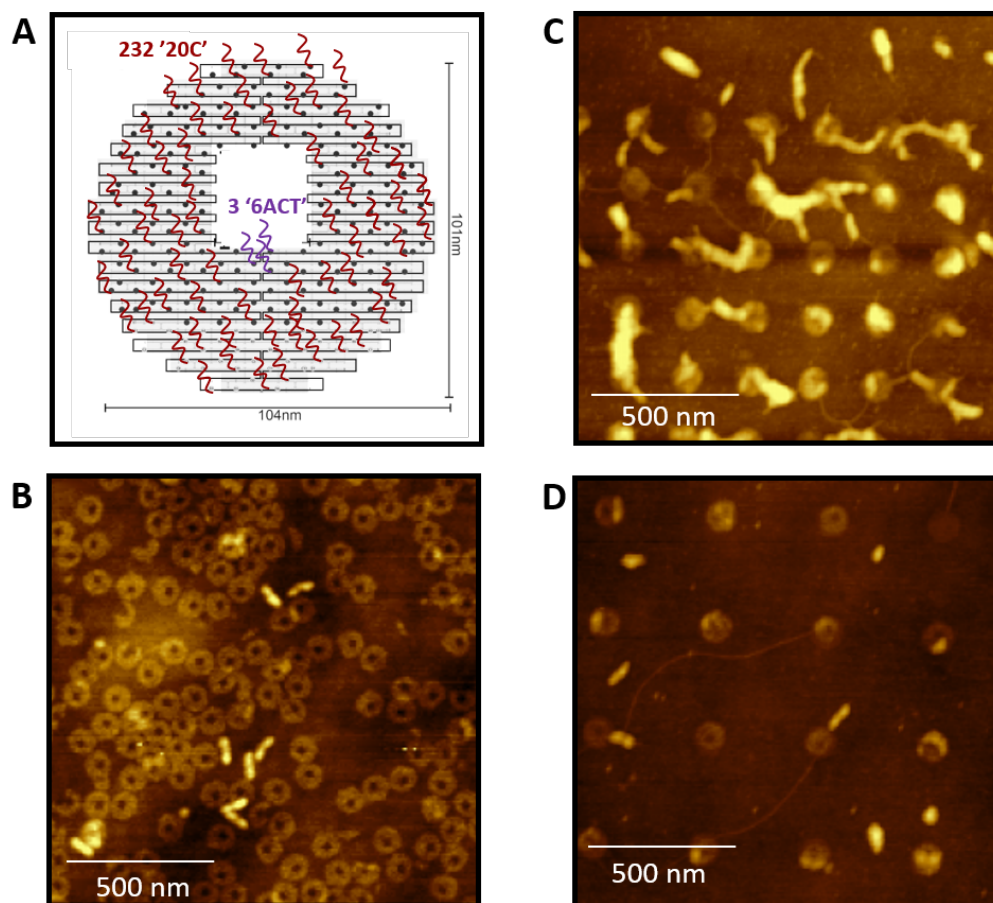


Figure 3.20: **Death star origami placement with 232 20C extensions.** A: Death star DNA origami with 232 20C extensions and 3 5'-ACTACTACTACTACTACT-3' strands in the middle of the origami. B: AFM of death star DNA origami with 232 20C extensions immobilized on silanized surface of SiO<sub>2</sub>. C: AFM of a part of a 9 by 9 array of death star origami with 20C extensions. D: AFM of a 4 by 4 array of the same origami with 20C extensions.

In order to improve DNA origami placement of origami functionalized with large (>42) numbers of molecular components, we studied death star origami with different extensions. Thymine or T is a nucleobase that is known to interact more strongly with the substrate surface compared to other nucleobases (A, C, G). Mainly for this reason we looked at placement of death star origami with 232 20C (5'-CCCCCCCCCCCCCCCCCCCC-3') extensions and 3 6ACT (5'-ACTACTACTACTACTACT-3') visualized in the figure 3.20A. Since complementary strands were not added to bridge two sides of the DNA origami together, we did

not observe taco shapes for this modification of death stars. Figure 3.20B presents an AFM image of death star origami with 232 20C extensions bound to silanized SiO<sub>2</sub> surface under MgCl<sub>2</sub> buffer. Most of the origami are well formed, not aggregated and not folded into taco shapes. We also reproduced these placements on quartz slides and silicon chips with thermally grown oxide. However, DNA origami placement on arrays with disk-shaped binding sites showed worse performance compared to bare death star origami without any extension strands. There is a significant number of "extra stuff" in the figure 3.20 on top of placed DNA origami arrays. This stuff is most likely formed by DNA origami that in solution phase were bound weakly to trimethylsilyl passivated background and rolled onto itself during ethanol drying process. This is the most important difference between our experiments and most of the experiments in the community which are characterized by wet AFM imaging. However, we think it is important to consider the problem in the context of potential applications and nonspecific bindings to the trimethylsilyl passivated areas contribute to the background of the dried sample. Alternative drying procedures could help to reduce this effect but are outside of the scope of this thesis.

We also looked at the mechanism that results in the folded origami shapes such as taco. I remind you that we first observed taco in death star origami that was labelled with 20T extensions and 20A linkers with Eu ions at one end (figure 3.17C). Since 20T or 5'-TTTTTTTTTTTTTTTTTTTTTTT-3' sequence can be bridged by 20A strands, bringing two halves of origami together and folding it at the seam, we looked at alternative unrepeatable sequences, such as 5'-GTTGTAGTGGTATGAGGTTG-3'. In the figure 3.21A and 3.21C, 5'-GTTGTAGTGGTATGAGGTTG-3' sequence is referred as "seq" and the complementary sequence 5'-CAACCTCATACTACTACAAC-3' is referred as "seq<sup>†</sup>". Figure 3.21B reveals another unexpected result, vast majority of death stars with 235 5'-GTTGTAGTGGTATGAGGTTG-3' strands per origami was folded into tacos. We do not have a complete understanding of the process and interactions of 5'-GTTGTAGTGGTATGAGGTTG-3' with each other that cause the death star origami to fold along its seam. It is important to note that folded shape of this origami can be only observed by AFM in air on silicon dioxide silanized surface. The same origami immobilized on mica surface will be flat under wet and dry AFM. The interactions between 5'-GTTGTAGTGGTATGAGGTTG-3' strands should be weaker than attraction to the mica surface under magnesium buffer. This would cause the origami to open up and lay flat on the mica.

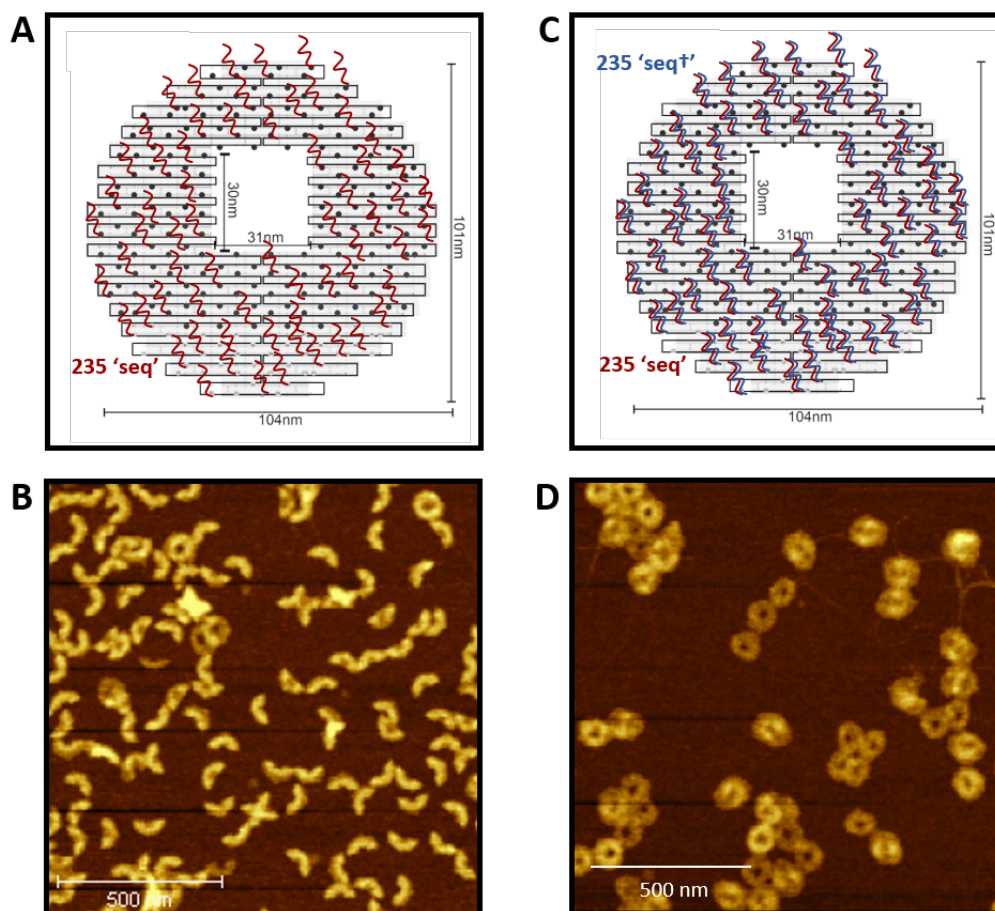


Figure 3.21: **Death star DNA origami with 235 5'-GTTGTAGTGGTATGAGGTTG-3' extensions.** A: Death star DNA origami with 235 20T extensions. Every staple that forms death star origami shape was modified by adding 20T to its sequence. B: Death star DNA origami with 42 20T extensions formed by 14 clusters of 3 20T extensions located at the circumference of the disk.

Another interesting observation came from experiment with origami that was functionalized with linker sequence 5'-CAACCTCATACCACTACAAC-3', which is complimentary to the extensions 5'-GTTGTAGTGGTATGAGGTTG-3' (figure 3.21D). This origami was flat and unfolded after ethanol drying. The addition of complimentary sequence prevented the strands from binding to each other and forming taco shapes. This confirmed our expectations: (1) interactions between single-stranded extensions and linkers can bind two halves of the DNA origami together and fold it along the seam, (2) choosing the sequence of the extensions such that the complimentary linker-strands bind to the extensions in 3' to 5' direction but not in 5' to 3' direction will prevent formation of taco shapes.

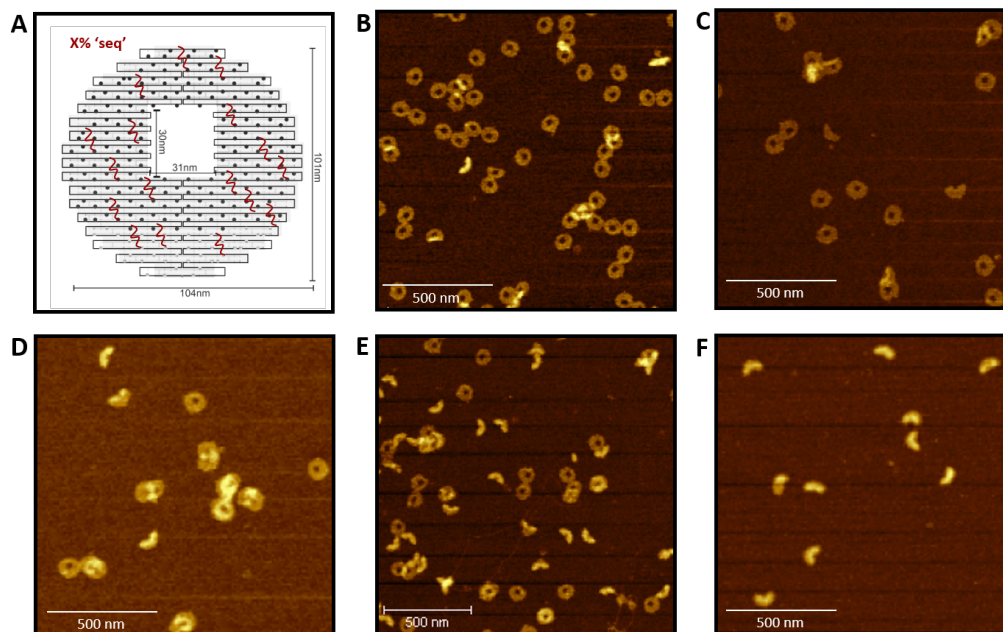


Figure 3.22: **Death star DNA origami with variable number of 5'-GTTGTAGTGGTATGAGGTTG-3' extensions per origami.** A: Death star DNA origami with X% of staples modified 5'-GTTGTAGTGGTATGAGGTTG-3' sequence and the rest of the staples are not modified and correspond to the "bare" death star origami. B-F: AFM images of death star DNA origami immobilized on SiO<sub>2</sub> and ethanol dried. Each AFM image has different percentage (X%) of modified staples, meaning that approximately one death star has  $X \cdot 235/100$  extensions. B: 0% corresponds to "bare" or unmodified death star, that usually does not form taco. C: 25% of staples are modified with extensions. You can see that tacos start appearing in the AFM. D: 50% of staples have extension. In the AFM scans of large areas with sufficient numbers of origami show about half of death stars folded into tacos. E: 75% of staples have extension and a higher percentage of origami is folded. F: 100% almost all origami folded into tacos.

Figure 3.22 demonstrates results of another experiment that looks at how many extensions can cause a death star origami to fold and form a taco. We have modified the staple mix for a death star by adding a percentage of X staples from a staple mix of death star origami modified with 5'-GTTGTAGTGGTATGAGGTTG-3' sequence. 5 different origami were annealed by following the standard protocol, immobilized on SiO<sub>2</sub> surface and ethanol dried before AFM imaging. It is expected that on average X% of staples on a single origami would have extensions and X% of all origami would have taco shape. Figures 3.22B - 3.22F speak towards this assumption, as the ration of taco shapes increase as the ration of modified staples increases.

### 3.4 Conclusions

This chapter focuses on a specific DNA origami shape that is called a "death star" throughout this thesis. The first section demonstrates how this DNA origami shape can be placed and aligned on SiO<sub>2</sub> surface with 3.2° precision and on a large scale with 3,456 origami having 12 distinct orientations. To demonstrate such a large-scale aligned self-assembly, we performed an optical measurement by intercalating origami with TOTO-3 dye molecules and measuring fluorescence polarization under a microscope. The main limitation of this method for single-photon applications is that we cannot control the number of intercalated emitters such as TOTO3, thus we cannot isolate and orient a single molecular emitter. In the second section, we explored a more robust emitter that can be attached to a single DNA strand. We studied death star origami shapes modified to carry chelated europium ion complexes and discovered the tendency of DNA origami to change its shape or bind to the surfaces depending on the number of extensions attached to the origami. The most significant discovery of this section is that the weak interactions between DNA origami extensions and trimethylsilyl passivated background can cause the weakly bound origami to shrink during ethanol drying step and leave residue. We have identified that placement is achievable for small numbers of Eu ion labels (< 42) and demonstrated DNA origami placement into 9 by 9 arrays on quartz slides inside lithographically patterned squares by atomic force microscopy and epifluorescence measurements. Finally, we looked at different DNA origami extensions and their role in the process of death star folding into taco shapes. We discovered that 5'-GTTGTAGTGGTATGAGGTTG-3' strands will interact with each other and cause the death star origami to fold along its seam forming a taco shape. However, death star folding can be avoided by adding a complimentary strand 5'-CAACCTCATACCACTACAAC-3' that will "neutralize" the extensions and restore the flat shape of the death star even after drying procedure.

This work identified limitations for deterministic single-emitter placement via DNA origami shape called "death star". Future experiments should involve a different shape of origami without flexible seams. Since method of absolute orientation of a single-molecule immobilized by DNA origami is yet to be demonstrated, we suggest using symmetrical shapes such as equilateral triangles. We observed that reducing the surface area of silanized binding sites by leaving small patch of trimethylsilyl monolayer inside the shape of the binding sites can reduce multiple binding of the DNA origami to the same binding site. However, it is yet to be determined how a DNA origami shape affects the accuracy of the single DNA

origami coupling to the binding site. For deterministic placement of a single emitter, we recommend keeping the number of extensions on the DNA origami to the minimum. In this work we demonstrated how different extensions on the DNA origami can cause non-specific binding to the neutral background which can result in photoluminescence noise from DNA origami attached to the background. Thus, future directions of research might include designing 3D shapes of DNA origami of different sizes that are rigid and do not form dimers or aggregates when modified with large number of extensions. One could also explore the specific sequences of these single-stranded extensions and the effect of their inter- and intramolecular interactions on the overall origami shape and on covalent binding strength to the silanized surface of the binding site and to the trimethylsilyl monolayer on the background.

*Chapter 4***DNA ORIGAMI AS A PLATFORM FOR NANOPARTICLE ASSEMBLY**

A solid-state based quantum optical network promises compact footprint and a path for scalable integration, as compared to their macroscopic cavity quantum electrodynamics counterparts. However, in comparison to atomic quantum emitters, molecular compounds and solid-state emitters exhibit dephasing and inhomogeneous broadening. At cryogenic temperatures, the dephasing time for some emitters  $T_2^*$  can be comparable to its total decay time  $T_1$ . Confinement of light can increase the local density of states (LDOS) at the position of the emitter, which will decrease the total decay time  $T_1$ , while keeping the dephasing time  $T_2^*$  the same. In this chapter, we explore approaches to incorporate emitters such as colloidal QDs and organic dye molecules within media with high LDOS. We demonstrate that we can deterministically position QDs on top of a microring resonator and place dye molecules next to plasmonic nanoparticles.

**4.1 DNA origami functionalization with QDs**

In this section we describe different methods that we explored to achieve DNA origami functionalization with a certain number of QDs. Labelling of a QD with DNA strands is a very challenging task from chemical point of view. We attempted getting reagents from commercial companies and research institutions but were not able to find a workable solution. First of all, we tried coupling QDs to 20A ssDNA via streptavidin to biotin binding. We ordered streptavidin coated QDs from Thermo Fisher and 5'-AAAAAAAAAAAAAAAAAAAAA-biotin-3' strand with a biotin molecule at the 3' end from IDT. To coat QD with 20A strands, we incubated 1  $\mu$ L of 1  $\mu$ M QD solution with 2  $\mu$ L of 1  $\mu$ M of 20A strands in water together overnight at room temperature. The process is illustrated in the figure 4.1C. We used death star DNA origami to immobilize these QDs on a surface. Two modifications of death stars were used: one was modified with 42 20T extensions and the second had only 3 20A extensions in the middle of the origami as depicted in the figures 4.1A and 4.1B. The staples of DNA origami had 20T strand added at the 5' end and 20A strands had QDs at the 3' ends. Thus, QDs were sticking out for about 10 nm

from the surface of the origami. To localize QDs to the smaller area on the origami, we used a tripod configuration: every binding site for a QD was comprised of three 20T extending strands.

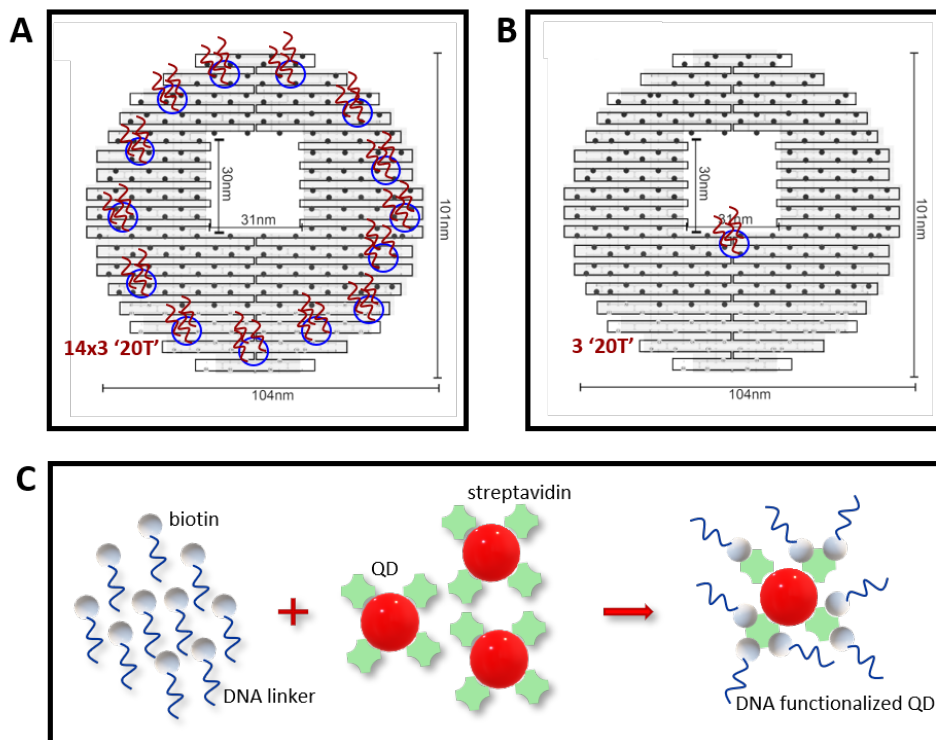


**Figure 4.1: DNA origami functionalization with QDs.** A: Death star DNA origami labelled with 42 20T strands arranged in groups of three. B: Death star DNA origami labelled with 3 20T strands. These three strands extend from the neighboring staples and are designed to hold a single QD in the middle like a tripod. C: To functionalize QD by 20A DNA strands, we incubate streptavidin coated QDs with 20A ssDNA with biotin at 3' end.

The quantitative characterization of this synthesis was performed by immobilization of functionalized DNA origami on silanized  $\text{SiO}_2$  surface. This process was done in two steps. First, DNA origami were immobilized on  $\text{SiO}_2$  by using a standard DNA origami placement method described in Appendix, but the samples were not dried. Second, 20  $\mu\text{L}$  of 1 nM QD solution were added to the washed samples with 20  $\mu\text{L}$  of 40 mM  $\text{MgCl}_2$  Tween buffer on them. The samples were incubated with QDs for at least 2 hours in humidified chamber made with a petri dish a wet Kimtech wipe. Afterwards, the samples were washed again 10 times with Tween buffer and ethanol dried. The AFM image in the figure 4.2 shows two samples imaged in air. The sample with 14 binding sites for QDs comprised of 42 20T

extensions (figures 4.1A and 4.2A) on average had 6 QDs per origami and the sample with 1 binding site per origami (figures 4.1B and 4.2B) had about half of origami with a single QD and half without any QDs. We made several conclusions from this experiment. First of all, it is not possible to couple more than 7 streptavidin coated QDs to a single DNA origami due to the large hydrodynamic radius that prevents QDs from coming close to each other. Second, as expected from the design of 20T extension that are located at the circumference of the death star, most of the QDs are attached at the edges of the origami. There is a visible spacial separation between most of the QDs and origami, which corresponds to the physical dimensions of the double stranded DNA linker. The third conclusion is coming from the figure 4.2B and the fact that only half origami is coupled to a QDs. This could point to the fact that the half of the origami that does not have a QD could be facing the surface of SiO<sub>2</sub> with 20T extensions underneath the origami. That would prevent QDs from binding to the middle of the death star origami. On the other side, samples with 6 QDs in the figure 4.2A have 20T extensions exposed to the side of the origami even when they are facing down.

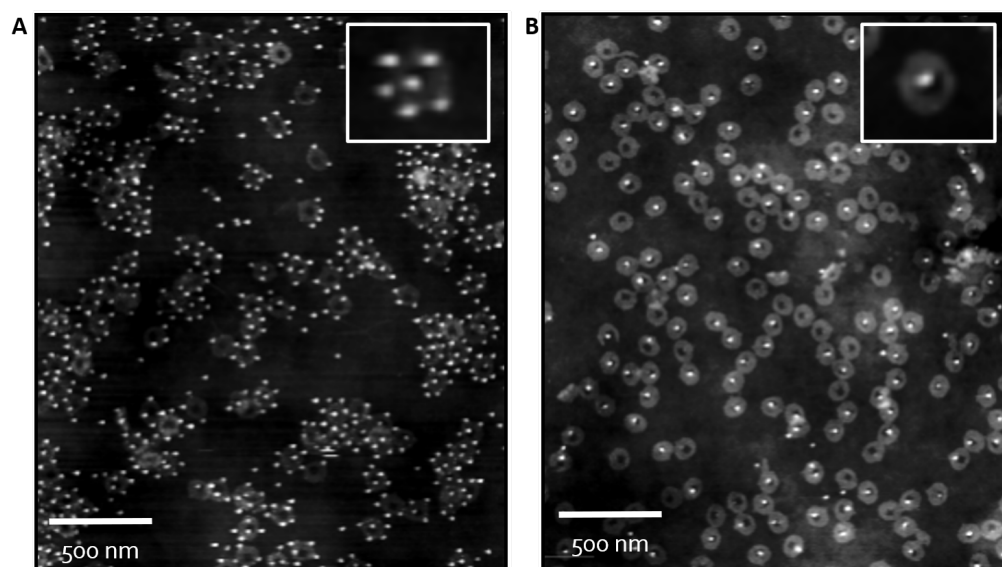


**Figure 4.2: AFM images of death star origami functionalized with QDs** A: Each origami was designed to capture 14 QDs, however, the average number of QDs per origami is 6 due to large hydrodynamic radius of QDs. B: Each origami was modified to carry only one QD, but the average number of QDs per origami is 0.5 with some origami having zero QDs. This can be explained by half of the death stars attaching face down to the surface and blocking the 20T extensions from binding to a QD.

To provide an additional proof of our ability to specifically bind QDs to nanostructures by using the method of DNA origami placement, we positioned QDs on top of microrings and performed optical measurements. The DNA origami binding sites were first defined by electron-beam lithography and arranged in the shape of a 4  $\mu\text{m}$  circle. Afterwards, the placement sites were activated by burning through trimethylsilyl passivation layer with oxygen plasma. New layer of negative electron-beam resist was spin-coated on top of activated DNA origami binding sites and the sample was patterned by e-beam lithography again. The resist layer was developed and left behind a ring of hardened polymer that defined a mask for the structure. Using ICP plasma etching the ring was transferred through the layer of silicon nitride as described in the flow diagram in the figure 4.3. As a last fabrication step, remaining resist was removed exposing DNA binding sites on top of the ring. After origami were placed, QDs were immobilized on top of origami in a process similar to described above.

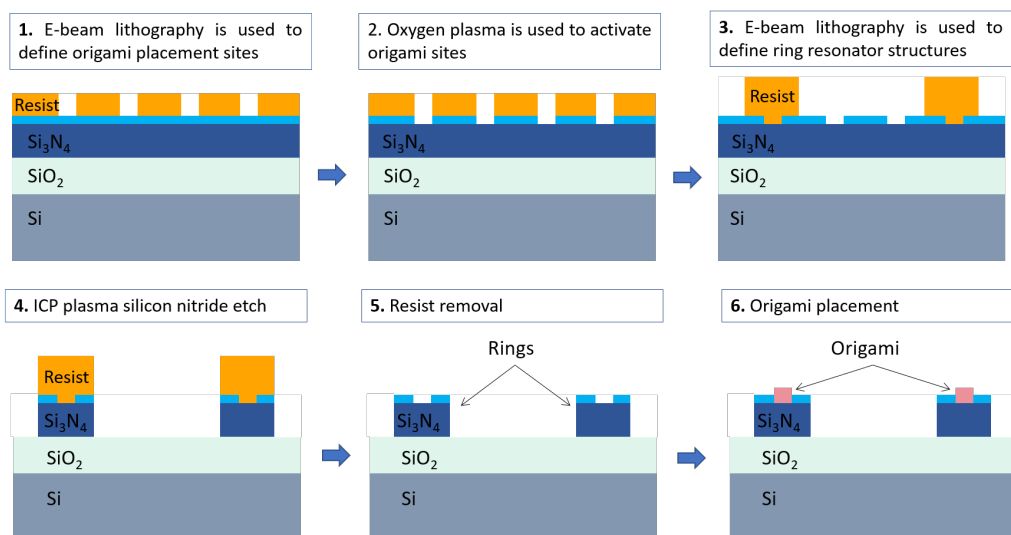


Figure 4.3: **Fabrication flow diagram of a microring with DNA origami on top.**

DNA origami were positioned inside binding sites on top of the ring by using a standard protocol for DNA origami placement described in Appendix. QDs were introduced as a step before ethanol drying of the sample similarly to the QD immobilization procedure above. The sample was dried and scanned in the AFM first, imaged in the optical confocal microscope, spectrally characterized and finally taken to the SEM.

Figure 4.4 presents SEM and AFM images of fabricated rings with DNA origami coupled to QDs on top of the rings. The dimensions of the fabricated ring

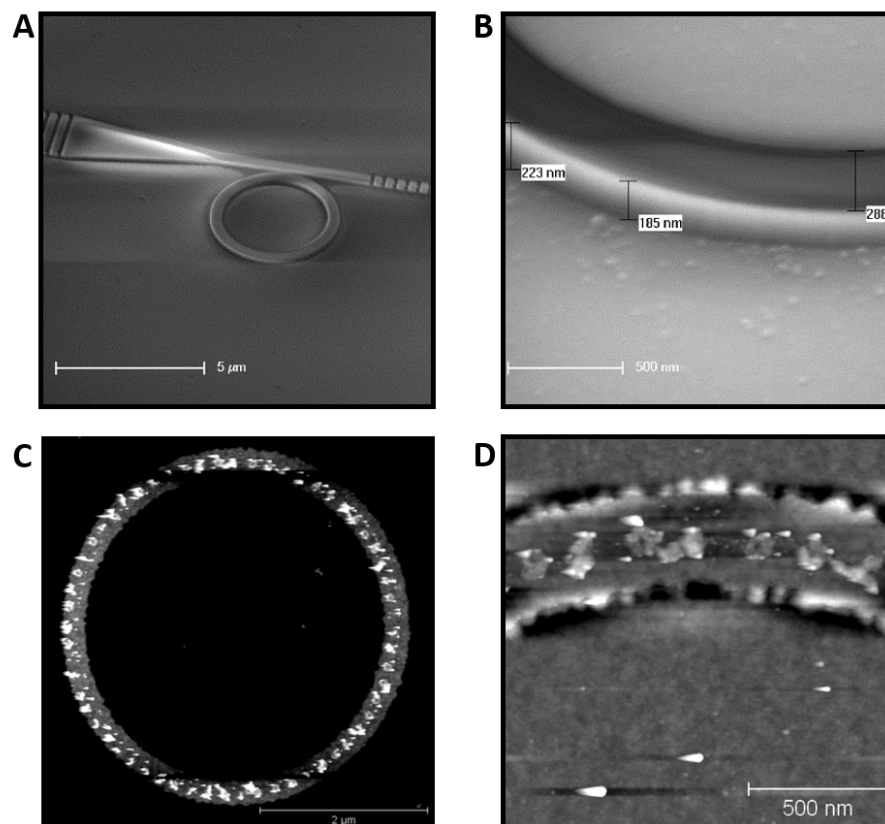


Figure 4.4: **DNA origami placement on microrings** A: SEM images of a microring with  $4\ \mu\text{m}$  diameter. B: Zoomed-in side SEM image of the ring, which is 200nm tall and about 300nm wide. C: AFM image of DNA origami with QDs positioned equidistantly on top of a ring by using DNA origami directed self-assembly method. D: Closer AFM of a segment of the ring with origami and QDs.

are noted in the figure 4.4B. Since the ring is 300 nm tall it is challenging to perform AFM scanning with high resolution. Figure 4.4C shows an AFM image of a whole ring with equidistant origami on top of it. In the figure 4.4D you can resolve brighter spots that correspond to QDs bound to origami.

Fluorescence image in the figure 4.5A confirms that small features on top of the ring in the previous figure are indeed QDs. The rings on the fluorescent image have  $4\ \mu\text{m}$  diameter and emit light transmitted through 650 nm bandpass filter after being excited by 488 nm laser light under a confocal microscope. The second part of this figure (figure 4.5B) is a recorded spectrum from an array of rings taken at a different fluorescence setup with a spectrometer. The sample was excited at 375nm and the peak of emission sits at 655 nm which is the emission wavelength of QDs specified by the manufacturing company. This further proves that we can

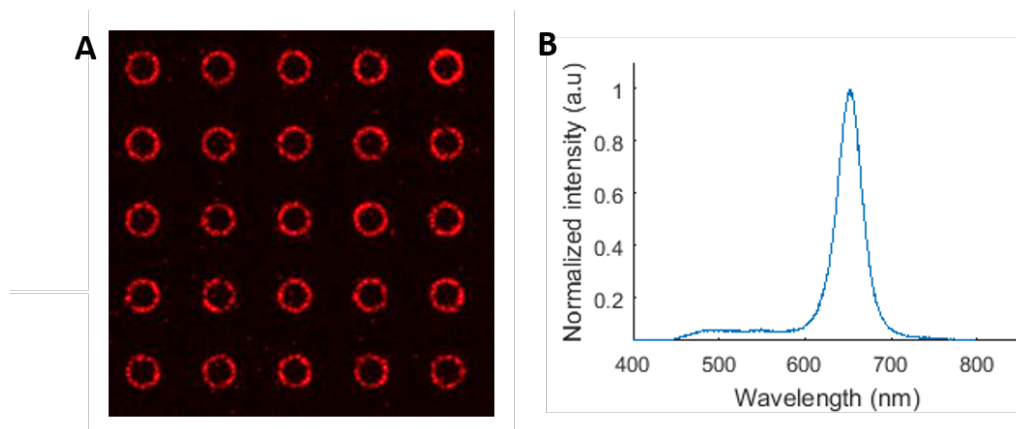


Figure 4.5: **Photoluminescence of QDs** A: Fluorescence from an array of 4 μm rings functionalized by QDs under 488 nm excitation laser. B: Spectra of this fluorescence shows peak at 655 nm, which corresponds to emission of QDs.

deterministically position QD on top of nanofabricated structures.

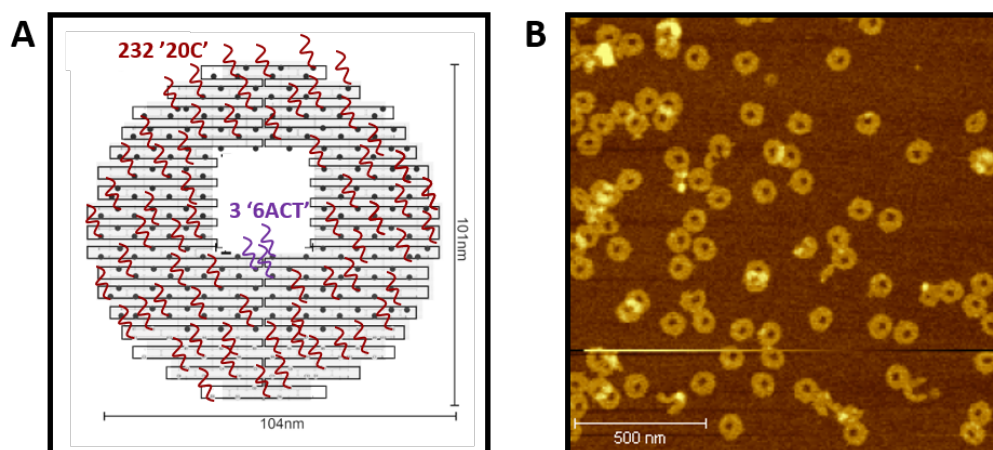


Figure 4.6: **Death star origami with one binding site for a QD**. A: A death star is functionalized with 20C extensions to break the symmetry and insure that that origami always attaches to the surface with the right-side up. One binding site for a QD in the middle consists of three ssDNA making a tripod construction for a QD. B: AFM image of these origami immobilized on SiO<sub>2</sub>.

To improve the efficiency of coupling a single QD to a DNA origami, we used a death star origami with all but three staples modified with 20C ssDNA. 20C extensions were added to break the symmetry and facilitate origami placement with right-side up. This would keep three extensions in the middle (5'-ACTACTACTACTACTACT-3') of the origami facing up and always available for QD binding. Figure 4.6A shows the location of different extensions and figure 4.6B

presents an AFM of these origami immobilized on SiO<sub>2</sub> surface. By introducing 1 nM solution of QDs to the sample with origami and incubating overnight, similarly to the recipe described above, we were able to get 87% efficiency of QD coupling, meaning 87% of all origami had only one QD. The result is presented by an AFM of a dried sample in figure 4.7.

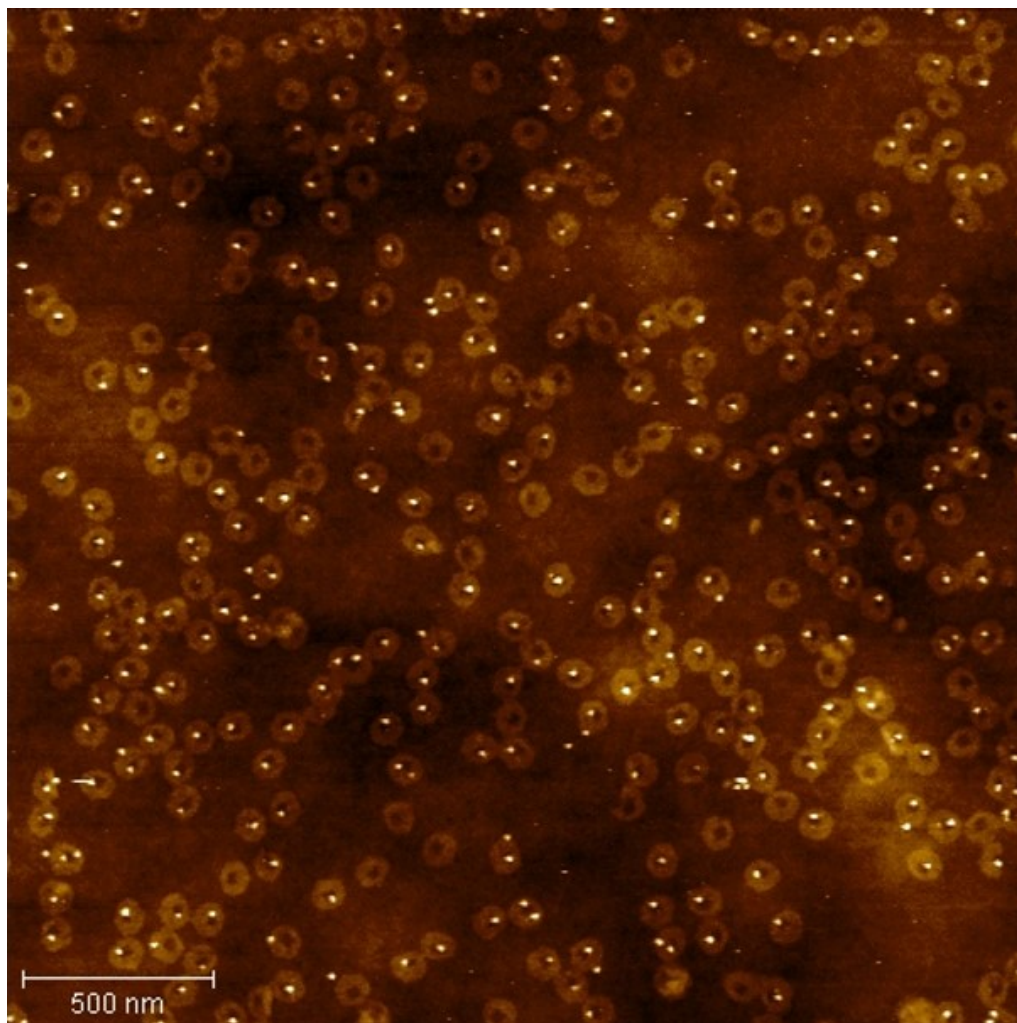


Figure 4.7: **Single QD-origami system.** Our system with highest percentage of single QDs coupled to single origami. The AFM shows 87% of origami have only a single QD attached to the origami.

We also studied the assembly of death star origami and QDs in solution phase using density gradient ultracentrifugation. For this method we used the same death stars with a single binding site for a QD and with 232 20C extensions. The prepared out QD sample using the same method described above. The QD were first incubated with biotinated ssDNA complimentary to the sequence of binding sites

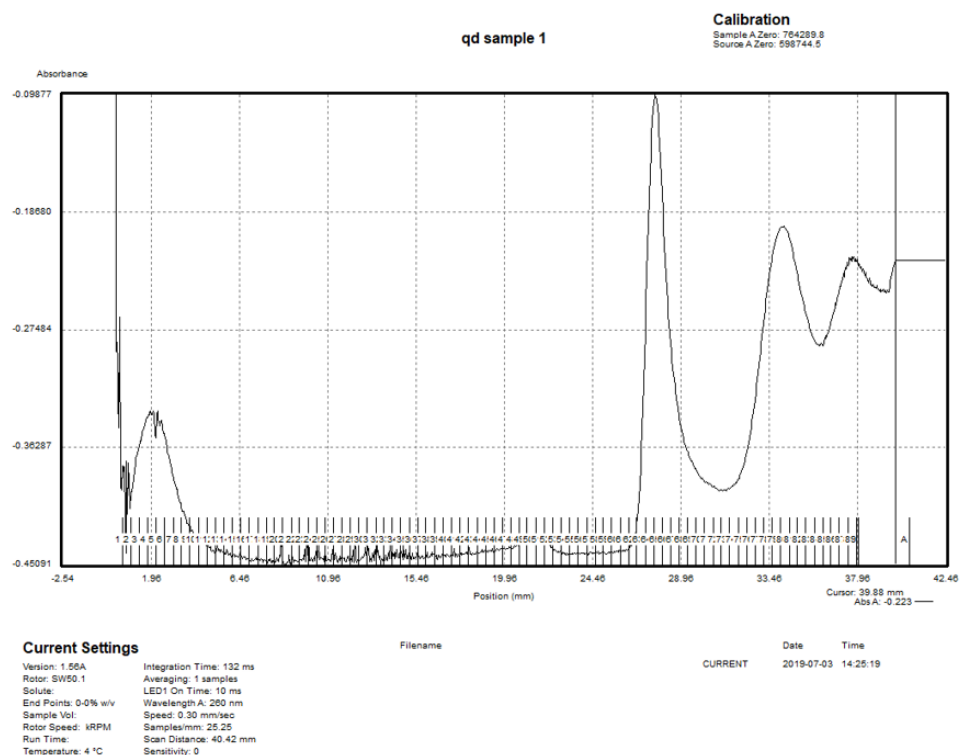
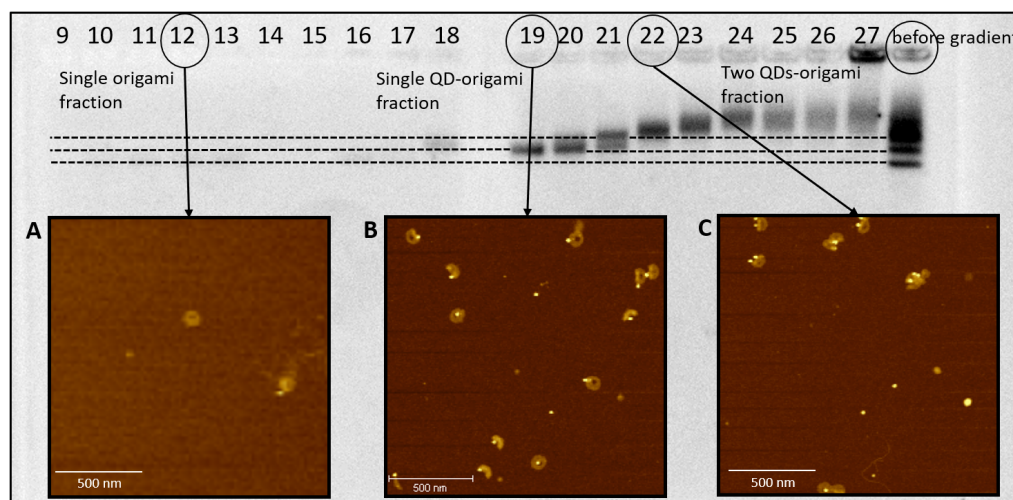


Figure 4.8: **Density gradient ultracentrifugation.** Absorbance of different fractions at 260 nm of origami sample coupled to a single QD. The first peak corresponds to short staples that were not coupled to QDs. The sharp peak at 28 mm is comprised of single origami that do not carry QDs. The broader peak after that at 35 mm correspond to the origami coupled to only one QD. The peaks after 38 mm position are due to absorption of origami with more than one QD, origami dimers and QDs that are not bound to origami.

(5'-AGTAGTAGTAGTAGTAGT-3') overnight. Origami were annealed separately and purified using 100 KDa Amicon spin filter. Prior to running the gradient purification 100  $\mu$ L of 10 nM DNA origami solution in 12.5 mM MgCl<sub>2</sub> buffer was combined with 8  $\mu$ L of 500 nM QDs functionalized with ssDNA. The reasoning behind these numbers is that we want the same ratio 2 to 1 of QDs to origami as in the previous experiments with assembly on the surface. The death star origami were incubated with DNA labelled QDs overnight. In the morning they were purified by density gradient ultracentrifugation at 50,000 rpm in sucrose gradient at 4° for 2 hours. Automatic fractionator was used to obtain the absorbance at 260 nm for each fraction of the sample. Since both DNA and QDs absorb light at 260 nm they show up as peaks in absorbance plot. The sharp peak at 28 mm in the figure 4.8 corresponds to the single DNA origami species without QD attached to them. The

desired system with only one QD per origami is located at 35 mm and also forms a well-defined peak. The other broad features in absorbance plot correspond to more complicated assemblies with several QDs per origami, origami dimers with QDs and QDs that did not bind to any origami travelled the longest distance and were pushed to the bottom of the vial with sucrose gradient.



**Figure 4.9: Gel electrophoresis and AFM of individual fractions collected after ultracentrifugation.** A: AFM image of the sample in the well number 12, which corresponds to a fraction with a single origami. B: Sample with one QD per origami as shows in the AFM of the sample in the well 19. C: Sample in the well 22 shows significant fluorescence in the gel scanner which is emitted by two QDs per origami.

To cross-reference these results with gel electrophoresis, we loaded collected fractions in the wells of 1% agarose gel and ran it at 100V for 1 hour. The post-stained with SYBR gold gel is presented in the figure 4.9. Since the density of origami collected after the gradient purification was low, the emission from the QD dominates the fluorescence from the SYBR gold stain. However, to identify the species in the different wells we have imaged some of the most fluorescent samples from wells 12, 19 and 22 in AFM. Figure 4.9A corresponds to the AFM of the sample in the well number 12 and confirms our suggestion that the first peak in absorbance plot is due to absorption of single DNA origami. AFM from the well number 19 reveals that every origami has a QD and is depicted in the figure 4.9B. The following fractions show significant fluorescence in the gel scanner and most likely correspond to origami bound to more than one QD and origami dimers. By performing AFM of the sample in the well 22, we identified that it had a few DNA origami with 2 QDs (figure 4.9C). These findings are consistent with our interpretation of absorbance plot in figure 4.8.

Finally, we conclude that assembly on the surface gives higher yield of single QD to single origami placement (up to 87%). However, it is challenging to completely eliminate nonspecific binding of QDs to background. Density gradient ultracentrifugation is a more powerful purification method for our system compared to conventional gel electrophoresis and gel extraction. It enables to select exclusively origami with single QDs, but the yield of this method is lower, the purified material comes in sucrose solution and dialysis is required to decrease sucrose concentration for further manipulations with the sample.

## 4.2 Single-photon fluorescent enhancement

Solid-state emitters exhibit large dephasing times homogeneous and inhomogeneous line-broadening. Homogeneous broadening is induced by phononic interactions in the host material and inhomogeneous broadening is due to defects and irregularities in the material. Two approaches can be used to mitigate each one of this factors. Plasmonic antennas can enlarge spontaneous emission rate making it exceed the pure-dephasing rate. However, due to extremely confined volumes, high precision of emitter placement is needed to achieve significant radiative rate enhancement (Wein et al., 2018). To reduce inhomogeneous broadening, high quality factor dielectric cavities are used as spectral filters to induce indistinguishability a posteriori (Grange et al., 2015).

A degree of indistinguishability of a quantum emitter can be expressed as a following ratio:

$$I = \frac{\gamma}{\gamma + \gamma^*},$$

where  $\gamma = 1/T_1$  is the population decay rate,  $\gamma^* = 1/T_2^*$  is the pure-dephasing rate and  $1/T_2 = 1/T_1 + 1/T_2^*$  is the total dephasing rate.

Single-photon emitters such as color centers, QDs, or organic molecules have pure-dephasing rates at room temperature that are typically 3 to 6 orders of magnitude larger than the population rate and intrinsic indistinguishability is usually very small making them non-viable candidates for quantum interactions. From the expression for  $I$  above it is obvious that one can effectively increase indistinguishability by increasing Purcell factor, or  $\gamma_{sp}/\gamma_{sp}^0$ , where  $\gamma_{sp}$  is enhanced spontaneous emission rate and  $\gamma_{sp}^0$  is spontaneous emission rate of the same emitter in vacuum, by modifying the LDOS of a dissipative emitter ( $\gamma^* \gg \gamma$ ).

In this section of the thesis we present several systems that could be potentially

used to increase indistinguishability of solid-state emitters. We will start with the dielectric ring resonator that can be coupled to colloidal QDs or chelated europium ion complexes via directed DNA origami self-assembly method. We have already demonstrated in the previous section of this chapter that DNA origami can be deterministically positioned on top of silicon nitride microring. To determine Purcell factor and spectral response of the ring we performed three-dimensional (3D) finite difference time domain (FDTD) simulation using FDTD Solutions from Lumerical Solutions, Inc. <https://www.lumerical.com/>. The Purcell factor of an emitter in dielectric medium is given by

$$F = \frac{3}{4\pi^2} \frac{\lambda^3 Q}{V},$$

where  $Q$  is cavity quality factor and  $\lambda^3/V$  is mode volume in cubic wavelengths.

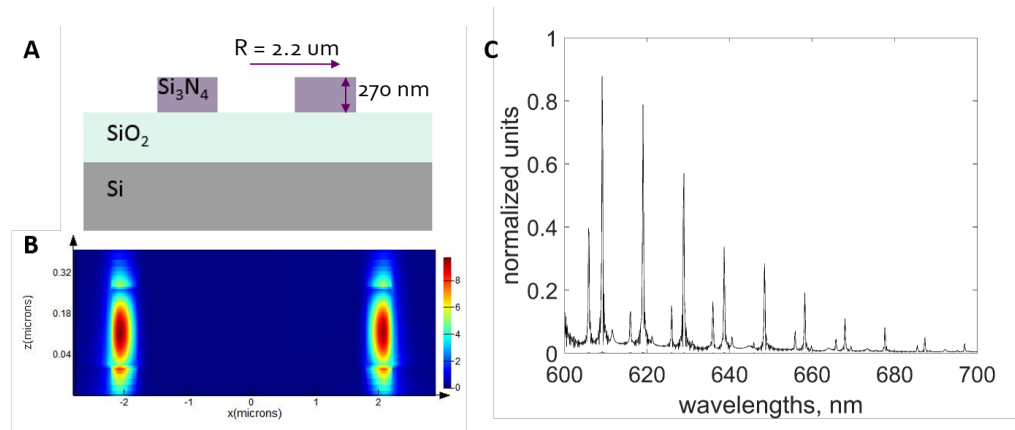


**Figure 4.10: Design of a silicon nitride ring.** A: Geometry of the ring. The outer radius is  $2.2 \mu\text{m}$  and the inner radius is  $1.8 \mu\text{m}$ . The ring is etched into  $270 \text{ nm}$  of silicon nitride and supported by several micrometers of silicon dioxide layer. B: Electric-field profile of a cross-section of the ring shows that the light is confined in the ring and a bit is leaking into the silicon dioxide substrate. C: Spectral response of such a ring has several sharp peaks that can be matched with emission of europium ions or QDs.

Figure 4.10A shows the materials and dimensions of the ring. We performed simulation in Lumerical for a silicon nitride ring on silicon dioxide substrate. The wafers were purchased from University Wafer and the specified thickness of thermally grown silicon nitride layer was  $270 \text{ nm}$ . We selected the outer and the inner radii of the ring to maximize the  $Q$  factor and to achieve spectral overlap with europium ions and CdSe/ZnS QDs. Figure 4.10B describes a side view of the electric-field profile in a ring with a  $2.2 \mu\text{m}$  outer radius,  $1.8 \mu\text{m}$  inner radius. In

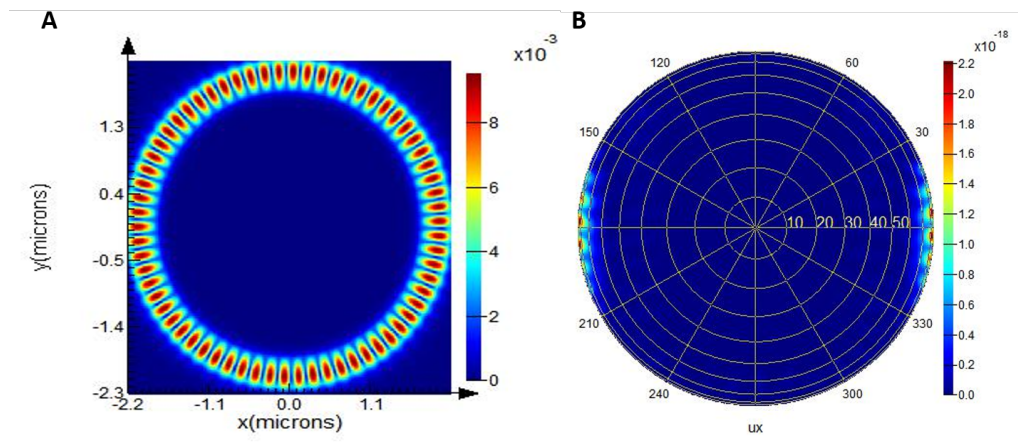


Figure 4.11: **Electric field of a microring.** A: Top view of the electric-field profile of the cross-section of the ring. Whispering gallery mode manifests in the multiple antinodes equidistant along the ring. B: Angular distribution of electric field projected into the far field of the ring. The majority light escapes through the side walls of the ring.

the simulation the ring was excited by a point dipole with emission peak at 640 nm. The Q factor of such a ring is  $10^3$  and its spectral response is depicted in the figure 4.10C. The whispering gallery mode of the ring is observable from the top view of the field mode profile in the figure 4.11A. The projected far field angular distribution in the figure 4.11B shows that the field is only emitted from the sides of the ring and waveguide coupler is required to effectively collect the light. When light resonant in ring is outcoupled with a waveguide from the side of the ring, the antinodes are not moving and such system presents a good opportunity for efficient coupling to the emitter on the top of the ring.

We were able to fabricate the system with parameters described above and position origami located in multiple locations corresponding to the antinodes of the microring (figure 4.3). Thus, we suggest that future experiments could be performed to validate whether this system can be used to effectively increase indistinguishability of colloidal QDs or europium ion complexes described in Chapter 3 at cryogenic temperatures.

The second structure that we considered was a plasmonic antenna assembled from two 50 nm gold nanocubes connected by DNA origami. The nanocube dimer is presented in the figure 4.12 and as a substrate we used glass slide. An emitter such as an organic dye molecule or europium ion complex is located between two cubes at the bottom corner as in figure 4.12A-B. We conducted simulations in

Lumerical to find optimal parameters of the structure for the highest radiative decay rate enhancement that could be realizable with the materials that we had. The plot of the radiative decay rate dependence on wavelength of emission is depicted in figure 4.12C. The nanocube dimer can increase radiative decay rate by 3000 for europium ions emitting at 620 nm with horizontal dipole moment. The field is highly confined in the space between two nanocubes as seen from electric-field profile of the cross-section of the structure in the figure 4.13A. The exact position of the emitter in the structure is critical to prevent quenching into plasmonic modes, thus chelated europium ion complexes presented in the previous chapter would be a good candidate for enhancement. The system works effectively as antenna and the light can be collected by conventional microscope objective with high numerical aperture (see figure 4.13B).

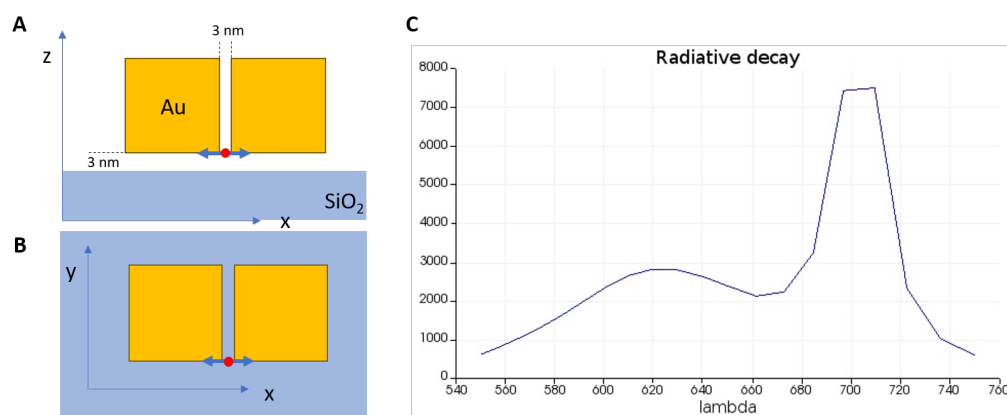


Figure 4.12: **Plasmonic nanocube dimer.** A: Geometrical dimensions and configuration of two 50 nm gold nanocubes with a horizontal dipole in between. The two cubes are separated by 3 nm and are sitting on top. B: View from the top. C: Radiative decay rate as a function of emission wavelength of a dipole from A and B.

We attempted to fabricate gold nanocube dimer by placing two cubes together by directed DNA self-assembly. Our collaborators from Prof. Seungwoo Lee's group in Sungkyunkwan University in South Korea provided us with 50 nm gold nanocubes functionalized with 30T (5'-30T-3') ssDNA. SEM of one of the cubes is presented in the figure 4.14A. We tried to couple nanocubes with death star DNA origami modified with 20A (5'-20A-3') extensions (see figure 4.14B) by using our method of surface assembly that worked successfully with colloidal QDs. We fabricated death star origami arrays depicted by AFM in the figure 4.14C and incubated with functionalized gold nanocubes overnight in 1x TAE 40 mM MgCl<sub>2</sub>

buffer. However, the AFM of the ethanol dried arrays did not reveal any coupling of the cubes to origami.

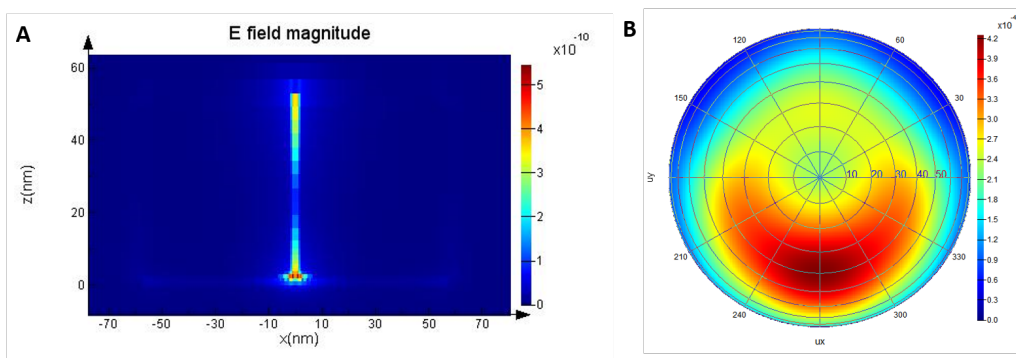


Figure 4.13: **Electric-field distribution.** A: View from the side. Electric field is confined in the space between two cubes. B: Far field angular distribution of  $|\vec{E}|^2$  demonstrates that the system outcouples the light effectively into the far field.

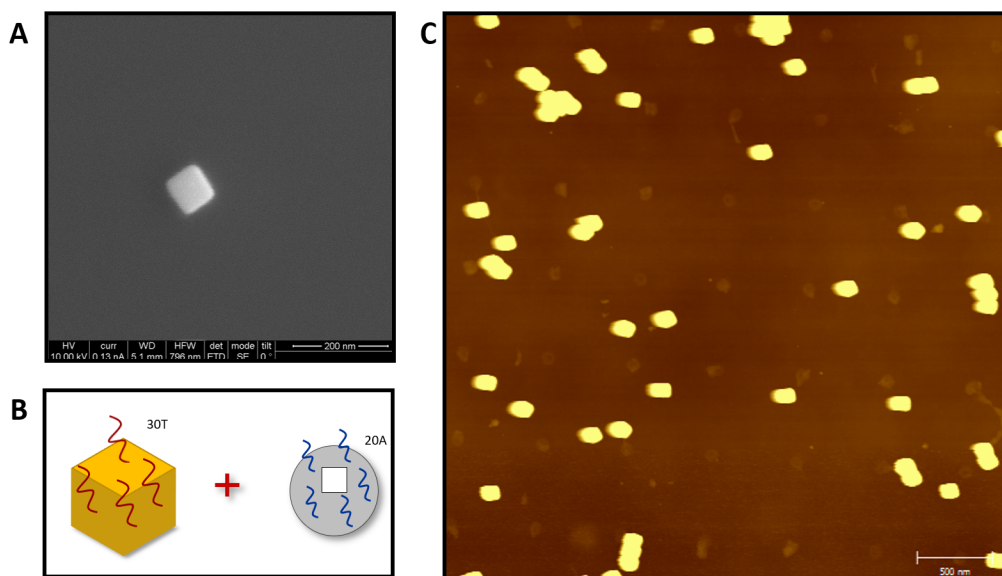


Figure 4.14: **Fabrication of a 50nm gold dimer.** A: SEM image of a gold cube. B: Coupling schematic of a nanocube functionalized with DNA strands and a death star origami with complimentary extensions. C: AFM showing an attempt to couple nanocubes to a placed death star origami array. It seems that the used nanocubes do not bind to origami on immobilized on the surface.

We conclude that our nanocube dimer could be utilized as a viable structure for the purposes of decreasing pure dephasing of molecular emitters. We suggest that the system should be assembled in solution on a DNA origami platform with

a molecular emitter embedded in the same DNA origami exactly in between two nanocubes.

Our next structure is an example of such a hybrid system assembled on a single DNA origami. Prof. Risheng Wang from Missouri University of Science and Technology was able to synthesize a gold nanostructure comprised of 3 gold spheres and one gold triangular plate that are held together by a single DNA origami. The dimensions of the structure are presented in the figure 4.15A, the gray frame around the gold triangular plate is a 3D DNA origami that is bound to the nanoparticles and is holding the structure together. A TEM image of the synthesized structures and an AFM image confirm the shape and parameters of the structures (see figures 4.15B-C).

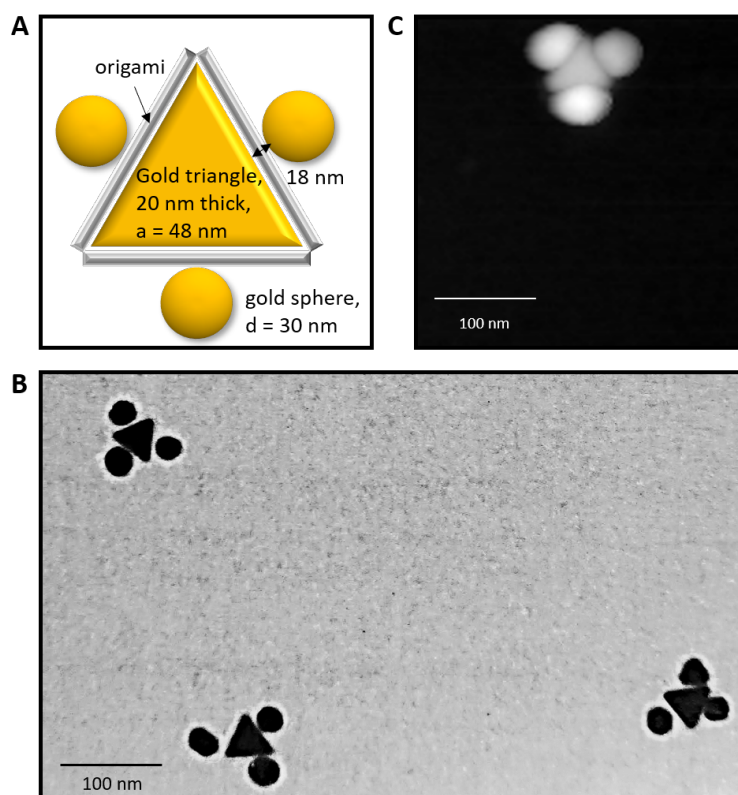


Figure 4.15: **Gold nanostructure assembled via DNA origami.** A: Three gold spheres with a 30 nm diameter are attached to a triangular origami. A gold triangular plate 20 nm thick and with a 48 nm side in located in the middle of the origami. B: TEM image of the structures provided by Risheng Wang. C: AFM image of a structure deposited on a glass slide scanned in air.

First, we simulated the electromagnetic field propagation emitted by a horizontal electric dipole moment located on DNA origami between a sphere and a plate

in 3D FDTD Lumerical. The dipole is pointing to the center of the triangular plate as can be seen in figure 4.16A. Due to the large gap between the plate and the sphere and the planar geometry of the plate the confinement of the electric field is not expected to be large. Thus, we have added a gold back reflector and a  $\text{SiO}_2$  spacer layer between the substrate and the structure. We propose to use template stripped gold surface and deposit 5 nm of silica by atomic layer deposition. This configuration, as displayed in figure 4.16B, increases significantly confinement in z-direction. The field profile of the structure at 555 nm presented in the figure 4.16C shows effective confinement between the plate and the sphere. Based on Purcell factor values for different wavelengths from figure 4.16D and non-radiative decay rates, we came to conclusion that we would be able to demonstrate that such structures assembled on a single DNA origami could be used for radiative decay rate enhancement.

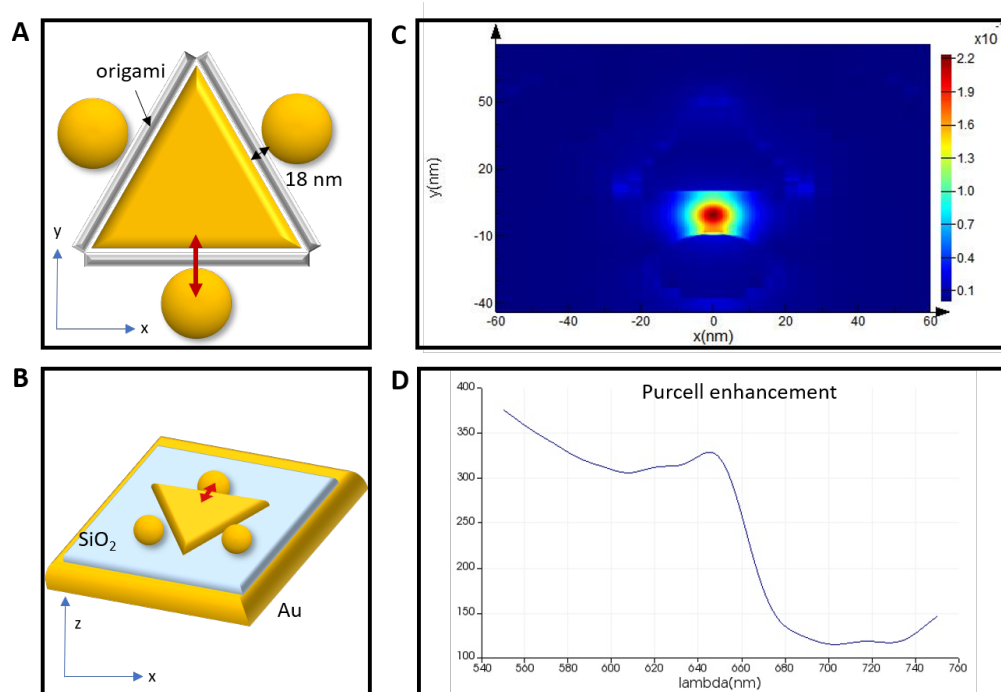


Figure 4.16: **Electromagnetic simulation of the nanostructure.** A: The response in the structure was recorded after being excited by a horizontal dipole pointing in the direction of the center of the triangular plate. B: The structure is deposited on a 5 nm  $\text{SiO}_2$  spacer layer on top of gold. C: Electric-field profile at  $\lambda = 555$  nm from 3D FDTD simulation in Lumerical software. D. Purcell factor for different wavelengths with respect to the dipole spontaneous decay rate in vacuum.

### 4.3 Optical measurements of a self-assembled nanoplasmonic system with embedded emitters

Our collaborates embedded an ATTO-532 fluorescent dye molecule (Integrated DNA Technologies) inside the triangular DNA origami support located between the plate and the sphere as in our simulation. ATTO-532 can be excited by 532 nm light and has a maximum of emission at 555nm. We deposited 10  $\mu\text{L}$  of nanostructures, suspended in 1x TAE 11.5 mM  $\text{MgCl}_2$  buffer, on silicon dioxide and incubated for two hours. The structures were already purified by gel electrophoresis and extracted from the gel, the approximated concentration of the structures was several nanomolar. After incubation we washed the sample with 40  $\mu\text{L}$  of fresh buffer with Tween 5 times and ethanol dried the sample. The AFM of the sample is shown in the figure 4.17. Only one structure had the expected configuration, but we assume that most of the structures have origami with embedded emitters attached to them.

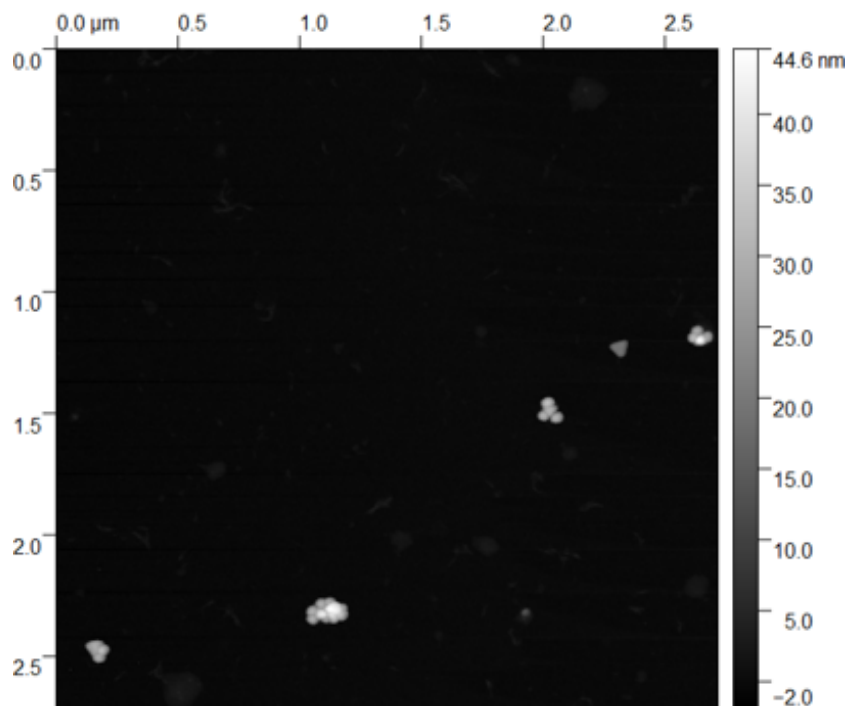
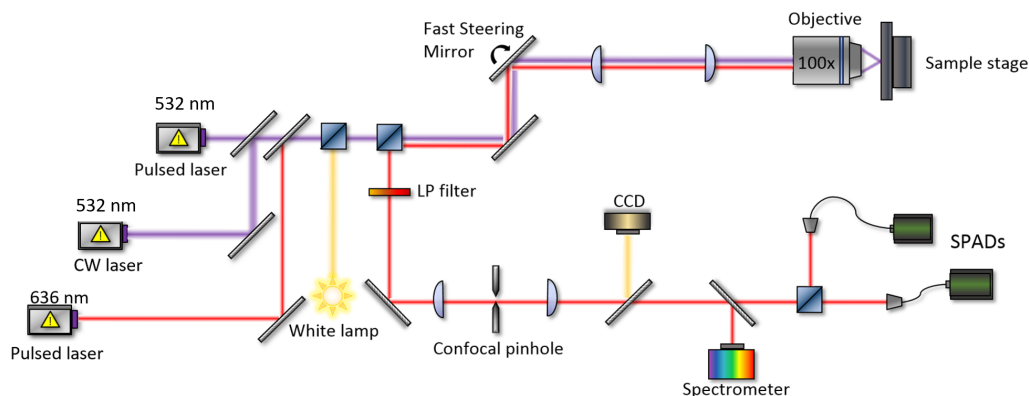


Figure 4.17: **AFM of the sample with 3 emitters per structure.** This AFM image shows that not all the structures remained in the initial configuration after deposition and ethanol drying procedures. Several structures aggregated, others lost one or more elements or deformed. However, one structure in the AFM has designed organization of its elements.

To demonstrate that the structures have a definite number of emitters, we



**Figure 4.18: Scanning confocal microscope setup.** In this experiment the samples were excited by 532 nm CW laser for PL measurements and with 532 nm pulsed laser for time-resolved measurements. The samples were scanned by a fast steering mirror and background was reduced by confocal pinhole. The PL maps and time-resolved PL were acquired with single-photon avalanche photodiodes (SPADs) and the spectra from the samples were measured by a monochromator with a Peltier cooled CCD camera.

performed optical characterization of two samples: one with 3 ATTO molecules in symmetrical locations and one with only one ATTO emitter (see figure 4.19A-B). Using our home built-scanning confocal microscope setup (see figure 4.18), we acquired photoluminescence (PL) map of an area on two samples. Figure 4.19C corresponds to a map of a sample with 3 emitters per each structure. We identified 4 bright spots on the map and fitted the intensity distributions with a Gaussian curve. On average the FWHM of a fitted Gaussian presented in the figure 4.19E was  $0.5 \mu\text{m}$  and the amplitude  $5.4 \cdot 10^4$  counts. Since the spots are diffraction limited they belong to the same structure or to an aggregate of structures, similar to one, scanned by AFM in the figure 4.17. Our next measurement confirmed that each spot indeed corresponds to a single hybrid nanostructure. For the second sample with a single emitter, a PL was acquired as well. From this map presented in the figure 4.19D we selected 3 bright spots and fitted their intensity distributions with a Gaussian curve (see figure 4.19F). The results confirmed that we have a diffraction limited spots with FWHM equal to  $0.5 \mu\text{m}$  and the amplitude of  $1.8 \cdot 10^4$  counts, which is exactly 3 times lower than the amplitude of the previous sample. This confirms that we can identify and isolate a single ATTO molecule within the gold nanostructure. Unfortunately, the bleaching rate of such organic dyes was too high to perform a second-order intensity correlation measurement, or  $g^{(2)}(\tau)$  function.

An ensemble PL measurement from ATTO molecules coupled to origami only

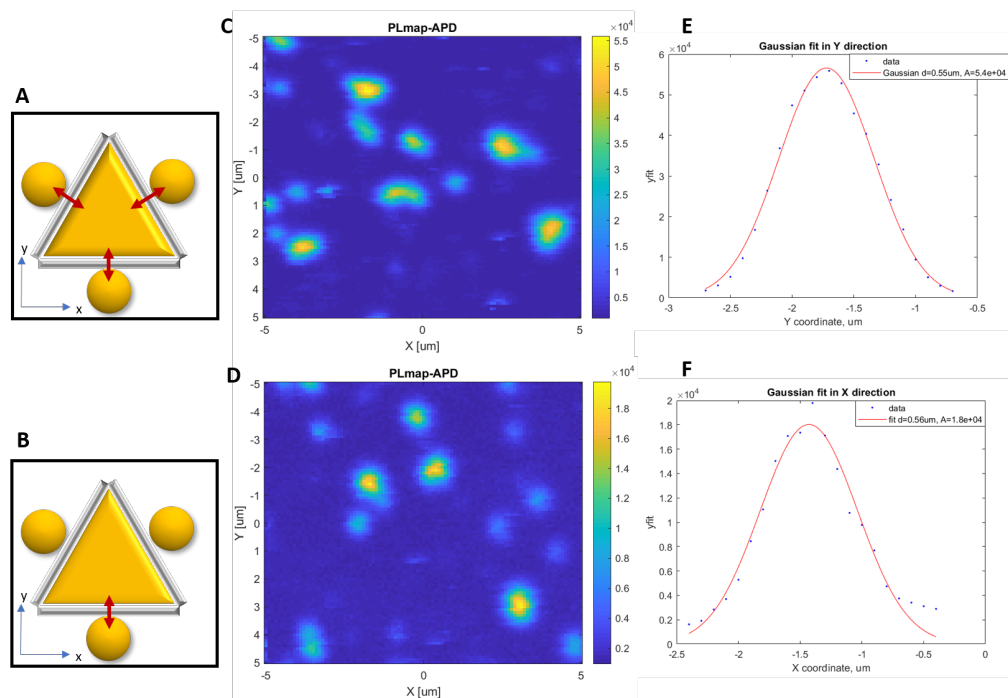
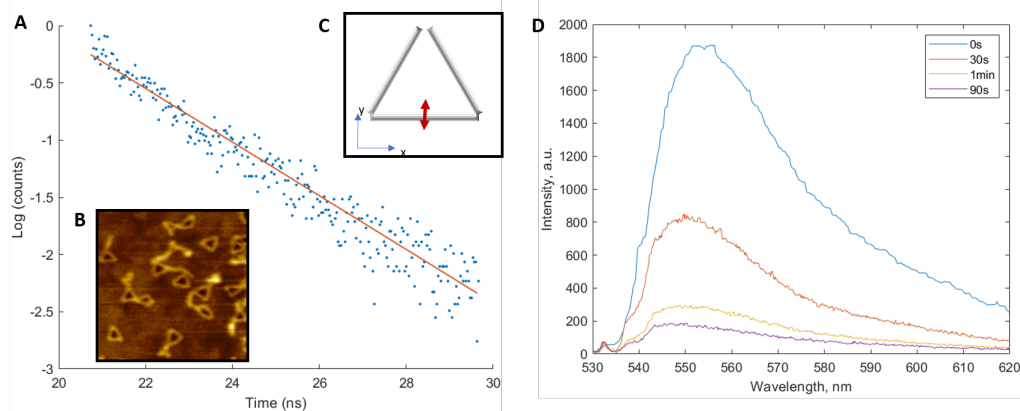


Figure 4.19: **Photoluminescence maps of the samples.** A: A gold nanostructure with 3 ATTO molecules. B: A gold nanostructure with one ATTO molecule. C: A PL map of the sample with structures in A deposited on silicon dioxide chip. D: A PL map of the sample with structures in B deposited on silicon dioxide chip. E: The intensity cross-section of one of the bright spots of the PL map in C was fitted with a Gaussian curve. The parameters of the fitting curve are: radius equals to  $0.5 \mu\text{m}$  and the amplitude equals  $5.4 \cdot 10^4$ . F: The parameters of the fitted Gaussian for the intensity distribution of one of the spots in D: radius equals to  $0.5 \mu\text{m}$  and the amplitude equals  $1.8 \cdot 10^4$ . This amplitude value in the sample A is three times large than the corresponding value of the sample B for all the spots, which suggests that light is emitted from a single ATTO molecule in sample B.

to confirm that the bleaching happens without plasmonic nanoparticles. In the figure 4.20C triangular origami is coupled only to the ATTO dye and AFM image in the figure 4.20B shows hollow triangular origami. This sample had much higher density of emitters and we were able to measure PL from several molecules. Time-resolved PL presented in the figure 4.20A shows linear decay in the log scale with calculated lifetime of 4 ns. To demonstrate bleaching, we measured spectra from the same spot on the sample for the first 30 seconds, for the second 30 seconds starting at 30s, for the third 30 seconds starting at 1 min and for the fourth 30 s started at one and a half minute at the low laser power ( $5 \mu\text{W}$ ). This was the lowest laser power setting that was giving spectra with a good signal to noise ratio. The results are shown in

the figure 4.20D, where you can see that PL decreases significantly after the first 30 s and decreases by two orders of magnitude in 2 min. This high bleaching rate makes it challenging to perform measurements with single ATTO molecules. We suggest using encapsulation strategies for future experiments at room temperature and increasing brightness of emitters by adding back reflector.



**Figure 4.20: Measurements of an ensemble ATTO molecules.** A: PL decay rate at log scale is a line. The lifetime of ATTO molecules obtained from the plot is 4 ns. B: AFM image of triangular origami with a single ATTO molecule. C: Triangular origami with a single ATTO molecules and removed gold nanoparticles. D: PL spectra of an ensemble of ATTO molecules coupled to DNA origami and excited by a CW laser with 532 nm wavelength and  $5 \mu\text{W}$  power. After each 30 s the PL significantly reduces and goes to background level in 2 min.

Overall, we intend to continue single-emitter measurements with this nanostructure, including measurements with a gold back reflector and a spacer layer at cryogenic temperature. Ideally, we would redesign the structure to achieve bowtie antenna architecture for ultrasmall resonator volume and high spontaneous decay rate enhancement. We would also replace ATTO molecule with chelated lanthanide ions to have a more robust emitter with lower unmodified pure-dephasing rates.

#### 4.4 Conclusions

In this chapter we studied several systems that can increase indistinguishability of solid-state emitters. We demonstrated coupling of colloidal QDs to dielectric ring resonators via DNA origami. We also showed DNA origami-enabled nanoparticle assembly with 3 gold nanospheres, a triangular gold plate and an embedded emitter. We suggested that a high-Q dielectric cavity can be utilized in combination with inhomogeneously broadened emitters such as QDs for spectral filtering. Al-

ternatively embedding emitters into plasmonic nanocavities with ultrasmall modal volume enables to achieve large Purcell enhancement of spontaneous emission and can decrease pure dephasing of dissipative emitters such as organic dyes.

DNA origami self-assembly provides a scalable bottom-up fabrication method for deterministic coupling of single emitters and molecules to silicon chips with top-down nanofabricated structures. Such systems could be integrated into photonic quantum networks for generations of qubits with large photon numbers for quantum computing applications. Another application of single-molecule coupling and Purcell enhancement of emission is single-molecule detection for bioengineering and medical diagnostics.

The future work on deterministic placement of single-emitter sources should utilize organic compounds with lanthanide ions that are robust against photobleaching and can have dephasing times in the order of microseconds. Plasmonic nanocavity with ultrasmall volume could be used to enhance spontaneous emission rate of rare-earth emitter compound for higher efficiency and lower signal to noise ratio. DNA origami enables to position the emitter inside the tight volumes of plasmonic nanocavities with a sub 5-nm precision. We suggest that the future efforts should focus on assembling a bowtie antenna structure on a 3D rectangular DNA origami. Triangular gold plates that we used in our nanostructure could be attached to a single sheet of rectangular origami with Eu ion molecular compound positioned in the hotspot of the bowtie. The architecture with a nanoparticle-structure on a gold mirror with dielectric spacer layer enables to achieve even larger confinement for dipole moments perpendicular to the plane of origami. DNA origami placement can be performed on smooth gold surfaces with a few-nm silica layer deposited by atomic layer deposition method. Deterministic placement and on-chip integration of such hybrid nanophotonic sources could result in a tremendous advancement into development of optical quantum computing.

## BIBLIOGRAPHY

- Acuna, G. P., F. M. Möller, P. Holzmeister, S. Beater, B. Lalkens, and P. Tinnefeld (Oct. 2012). “Fluorescence Enhancement at Docking Sites of DNA-Directed Self-Assembled Nanoantennas”. In: *Science* 338.6106, p. 506. DOI: 10.1126/science.1228638. URL: <http://science.sciencemag.org/content/338/6106/506.abstract>.
- Akimov, A. V., A. Mukherjee, C. L. Yu, D. E. Chang, A. S. Zibrov, P. R. Hemmer, H. Park, and M. D. Lukin (Nov. 2007). “Generation of single optical plasmons in metallic nanowires coupled to quantum dots”. In: *Nature* 450.7168, pp. 402–406. ISSN: 0028-0836, 1476-4687. DOI: 10.1038/nature06230. URL: <http://www.nature.com/articles/nature06230> (visited on 04/03/2020).
- Altewischer, E., M. P. van Exter, and J. P. Woerdman (July 2002). “Plasmon-assisted transmission of entangled photons”. In: *Nature* 418.6895, pp. 304–306. ISSN: 0028-0836, 1476-4687. DOI: 10.1038/nature00869. URL: <http://www.nature.com/articles/nature00869> (visited on 04/03/2020).
- Arbabi, Amir and Lynford L. Goddard (Oct. 1, 2013). “Measurements of the refractive indices and thermo-optic coefficients of Si<sub>3</sub>N<sub>4</sub> and SiO<sub>x</sub> using microring resonances”. In: *Optics Letters* 38.19. Publisher: Optical Society of America, pp. 3878–3881. ISSN: 1539-4794. DOI: 10.1364/OL.38.003878. URL: <https://www.osapublishing.org/ol/abstract.cfm?uri=ol-38-19-3878> (visited on 04/13/2020).
- Archambault, Alexandre, François Marquier, Jean-Jacques Greffet, and Christophe Arnold (July 12, 2010). “Quantum theory of spontaneous and stimulated emission of surface plasmons”. In: *Physical Review B* 82.3, p. 035411. ISSN: 1098-0121, 1550-235X. DOI: 10.1103/PhysRevB.82.035411. URL: <https://link.aps.org/doi/10.1103/PhysRevB.82.035411> (visited on 04/03/2020).
- Bennett, Charles H., François Bessette, Gilles Brassard, Louis Salvail, and John Smolin (Jan. 1992). “Experimental quantum cryptography”. en. In: *Journal of Cryptology* 5.1, pp. 3–28. ISSN: 1432-1378. DOI: 10.1007/BF00191318. URL: <https://doi.org/10.1007/BF00191318> (visited on 04/25/2020).
- Benson, Oliver (Dec. 2011). “Assembly of hybrid photonic architectures from nanophotonic constituents”. en. In: *Nature* 480.7376, pp. 193–199. ISSN: 1476-4687. DOI: 10.1038/nature10610. URL: <https://www.nature.com/articles/nature10610> (visited on 04/27/2020).
- Bergman, David J. and Mark I. Stockman (Jan. 14, 2003). “Surface Plasmon Amplification by Stimulated Emission of Radiation: Quantum Generation of Coherent Surface Plasmons in Nanosystems”. In: *Physical Review Letters* 90.2, p. 027402. ISSN: 0031-9007, 1079-7114. DOI: 10.1103/PhysRevLett.90.027402. URL:

- <https://link.aps.org/doi/10.1103/PhysRevLett.90.027402> (visited on 04/03/2020).
- Berini and De Leon (Jan. 2012). “Surface plasmon–polariton amplifiers and lasers”. en. In: *Nature Photonics* 6.1. Number: 1 Publisher: Nature Publishing Group, pp. 16–24. ISSN: 1749-4893. DOI: 10.1038/nphoton.2011.285. URL: <https://www.nature.com/articles/nphoton.2011.285> (visited on 05/31/2020).
- Bhar, G.C. (July 1991). “A technique for the calculation of phase-matching angle for type-II noncollinear sum-frequency generation in negative uniaxial crystals.” In: *Opt. Comm* 80, p. 381384.
- Brokmann, X., G. Messin, P. Desbiolles, E. Giacobino, M. Dahan, and J. P. Hermier (July 2004). “Colloidal CdSe/ZnS quantum dots as single-photon sources”. en. In: *New Journal of Physics* 6. Publisher: IOP Publishing, pp. 99–99. ISSN: 1367-2630. DOI: 10.1088/1367-2630/6/1/099. (Visited on 04/25/2020).
- Brouri, Rosa, Alexios Beveratos, Jean-Philippe Poizat, and Philippe Grangier (Sept. 2000). “Photon antibunching in the fluorescence of individual color centers in diamond”. EN. In: *Optics Letters* 25.17. Publisher: Optical Society of America, pp. 1294–1296. ISSN: 1539-4794. DOI: 10.1364/OL.25.001294. URL: <https://www.osapublishing.org/ol/abstract.cfm?uri=ol-25-17-1294> (visited on 04/25/2020).
- Buller, G. S. and R. J. Collins (Nov. 2009). “Single-photon generation and detection”. In: *Measurement Science and Technology* 21.1. Publisher: IOP Publishing, p. 012002. ISSN: 0957-0233. DOI: 10.1088/0957-0233/21/1/012002. (Visited on 04/25/2020).
- Cai, Yong-Jing, Ming Li, Xi-Feng Ren, Chang-Ling Zou, Xiao Xiong, Hua-Lin Lei, Bi-Heng Liu, Guo-Ping Guo, and Guang-Can Guo (July 14, 2014). “High-Visibility On-Chip Quantum Interference of Single Surface Plasmons”. In: *Physical Review Applied* 2.1, p. 014004. ISSN: 2331-7019. DOI: 10.1103/PhysRevApplied.2.014004. URL: <https://link.aps.org/doi/10.1103/PhysRevApplied.2.014004> (visited on 04/03/2020).
- Carolan, Jacques, Christopher Harrold, Chris Sparrow, Enrique Martín-López, Nicholas J. Russell, Joshua W. Silverstone, Peter J. Shadbolt, Nobuyuki Matsuda, Manabu Oguma, Mikitaka Itoh, Graham D. Marshall, Mark G. Thompson, Jonathan C. F. Matthews, Toshikazu Hashimoto, Jeremy L. O’Brien, and Anthony Laing (Aug. 2015). “Universal linear optics”. en. In: *Science* 349.6249, pp. 711–716. ISSN: 0036-8075, 1095-9203. DOI: 10.1126/science.aab3642. URL: <https://science.sciencemag.org/content/349/6249/711> (visited on 04/24/2020).
- Chen, Junghuei and Nadrian C. Seeman (Apr. 1991). “Synthesis from DNA of a molecule with the connectivity of a cube”. In: *Nature* 350.6319, pp. 631–633. ISSN: 0028-0836, 1476-4687. DOI: 10.1038/350631a0. URL: <http://www.nature.com/articles/350631a0> (visited on 04/21/2020).

- Chen, Yueyang, Albert Ryou, Max R. Friedfeld, Taylor Fryett, James Whitehead, Brandi M. Cossairt, and Arka Majumdar (Oct. 2018). “Deterministic Positioning of Colloidal Quantum Dots on Silicon Nitride Nanobeam Cavities”. In: *Nano Letters* 18.10. Publisher: American Chemical Society, pp. 6404–6410. ISSN: 1530-6984. DOI: [10.1021/acs.nanolett.8b02764](https://doi.org/10.1021/acs.nanolett.8b02764). URL: <https://doi.org/10.1021/acs.nanolett.8b02764> (visited on 04/27/2020).
- Chikkaraddy, Rohit, Bart de Nijs, Felix Benz, Steven J. Barrow, Oren A. Scherman, Edina Rosta, Angela Demetriadou, Peter Fox, Ortwin Hess, and Jeremy J. Baumberg (July 2016). “Single-molecule strong coupling at room temperature in plasmonic nanocavities”. en. In: *Nature* 535.7610. Number: 7610 Publisher: Nature Publishing Group, pp. 127–130. ISSN: 1476-4687. DOI: [10.1038/nature17974](https://doi.org/10.1038/nature17974). URL: <https://www.nature.com/articles/nature17974> (visited on 04/22/2020).
- Chikkaraddy, Rohit, V. A. Turek, Nuttawut Kongsuwan, Felix Benz, Cloudy Carnegie, Tim van de Goor, Bart de Nijs, Angela Demetriadou, Ortwin Hess, Ulrich F. Keyser, and Jeremy J. Baumberg (Jan. 2018). “Mapping Nanoscale Hotspots with Single-Molecule Emitters Assembled into Plasmonic Nanocavities Using DNA Origami”. en. In: *Nano Letters* 18.1, pp. 405–411. ISSN: 1530-6984, 1530-6992. DOI: [10.1021/acs.nanolett.7b04283](https://doi.org/10.1021/acs.nanolett.7b04283). URL: <https://pubs.acs.org/doi/10.1021/acs.nanolett.7b04283> (visited on 04/22/2020).
- Choy, Jennifer T., Birgit J. M. Hausmann, Thomas M. Babinec, Irfan Bulu, Mughees Khan, Patrick Maletinsky, Amir Yacoby, and Marko Lončar (Dec. 2011). “Enhanced single-photon emission from a diamond–silver aperture”. en. In: *Nature Photonics* 5.12. Number: 12 Publisher: Nature Publishing Group, pp. 738–743. ISSN: 1749-4893. DOI: [10.1038/nphoton.2011.249](https://doi.org/10.1038/nphoton.2011.249). URL: <https://www.nature.com/articles/nphoton.2011.249> (visited on 04/26/2020).
- Chworos, Arkadiusz, Isil Severcan, Alexey Y. Koyfman, Patrick Weinkam, Emin Oroudjev, Helen G. Hansma, and Luc Jaeger (2004). “Building Programmable Jigsaw Puzzles with RNA”. In: *Science* 306.5704, pp. 2068–2072. ISSN: 0036-8075. DOI: [10.1126/science.1104686](https://doi.org/10.1126/science.1104686). eprint: <https://science.sciencemag.org/content/306/5704/2068.full.pdf>. URL: <https://science.sciencemag.org/content/306/5704/2068>.
- Clauser, John F. (Feb. 1974). “Experimental distinction between the quantum and classical field-theoretic predictions for the photoelectric effect”. In: *Physical Review D* 9.4. Publisher: American Physical Society, pp. 853–860. DOI: [10.1103/PhysRevD.9.853](https://doi.org/10.1103/PhysRevD.9.853). URL: <https://link.aps.org/doi/10.1103/PhysRevD.9.853> (visited on 04/24/2020).
- Di Martino, G., Y. Sonnefraud, M. S. Tame, S. Kéna-Cohen, F. Dieleman, Ş. K. Özdemir, M. S. Kim, and S. A. Maier (Apr. 15, 2014). “Observation of Quantum Interference in the Plasmonic Hong-Ou-Mandel Effect”. In: *Physical Review Applied* 1.3, p. 034004. ISSN: 2331-7019. DOI: [10.1103/PhysRevApplied.1.3](https://doi.org/10.1103/PhysRevApplied.1.3)

034004. URL: <https://link.aps.org/doi/10.1103/PhysRevApplied.1.034004> (visited on 04/03/2020).
- Di Martino, Giuliana, Yannick Sonnefraud, Stéphane Kéna-Cohen, Mark Tame, Şahin K. Özdemir, M. S. Kim, and Stefan A. Maier (May 9, 2012). “Quantum Statistics of Surface Plasmon Polaritons in Metallic Stripe Waveguides”. In: *Nano Letters* 12.5. Publisher: American Chemical Society, pp. 2504–2508. ISSN: 1530-6984. DOI: 10.1021/nl300671w. URL: <https://doi.org/10.1021/nl300671w> (visited on 04/03/2020).
- Dicke (Jan. 1954). “Coherence in Spontaneous Radiation Processes”. In: *Physical Review* 93.1. Publisher: American Physical Society, pp. 99–110. DOI: 10.1103/PhysRev.93.99. URL: <https://link.aps.org/doi/10.1103/PhysRev.93.99> (visited on 05/05/2020).
- Ding, Baoquan, Hao Wu, Wei Xu, Zhao Zhao, Yan Liu, Hongbin Yu, and Hao Yan (Dec. 2010). “Interconnecting Gold Islands with DNA Origami Nanotubes”. In: *Nano Letters* 10.12. Publisher: American Chemical Society, pp. 5065–5069. ISSN: 1530-6984. DOI: 10.1021/nl1033073. URL: <https://doi.org/10.1021/nl1033073> (visited on 04/28/2020).
- Elson, J. M. and R. H. Ritchie (Dec. 15, 1971). “Photon Interactions at a Rough Metal Surface”. In: *Physical Review B* 4.12, pp. 4129–4138. ISSN: 0556-2805. DOI: 10.1103/PhysRevB.4.4129. URL: <https://link.aps.org/doi/10.1103/PhysRevB.4.4129> (visited on 04/03/2020).
- Englund, Dirk, Andrei Faraon, Ilya Fushman, Nick Stoltz, Pierre Petroff, and Jelena Vučković (Dec. 2007). “Controlling cavity reflectivity with a single quantum dot”. en. In: *Nature* 450.7171. Number: 7171 Publisher: Nature Publishing Group, pp. 857–861. ISSN: 1476-4687. DOI: 10.1038/nature06234. URL: <https://www.nature.com/articles/nature06234> (visited on 04/26/2020).
- Englund, Dirk, Brendan Shields, Kelley Rivoire, Fariba Hatami, Jelena Vučković, Hongkun Park, and Mikhail D. Lukin (Oct. 2010). “Deterministic Coupling of a Single Nitrogen Vacancy Center to a Photonic Crystal Cavity”. In: *Nano Letters* 10.10. Publisher: American Chemical Society, pp. 3922–3926. ISSN: 1530-6984. DOI: 10.1021/nl101662v. URL: <https://doi.org/10.1021/nl101662v> (visited on 04/27/2020).
- Fakonas, James S., Hyunseok Lee, Yousif A. Kelaita, and Harry A. Atwater (Apr. 2014). “Two-plasmon quantum interference”. In: *Nature Photonics* 8.4, pp. 317–320. ISSN: 1749-4885, 1749-4893. DOI: 10.1038/nphoton.2014.40. URL: <http://www.nature.com/articles/nphoton.2014.40> (visited on 04/03/2020).
- Faraon, Andrei, Paul E. Barclay, Charles Santori, Kai-Mei C. Fu, and Raymond G. Beausoleil (May 2011). “Resonant enhancement of the zero-phonon emission from a colour centre in a diamond cavity”. en. In: *Nature Photonics* 5.5. Number: 5 Publisher: Nature Publishing Group, pp. 301–305. ISSN: 1749-4893. DOI: 10.

- 1038/nphoton.2011.52. URL: <https://www.nature.com/articles/nphoton.2011.52> (visited on 04/26/2020).
- Fasel, Sylvain, Franck Robin, Esteban Moreno, Daniel Erni, Nicolas Gisin, and Hugo Zbinden (Mar. 21, 2005). “Energy-Time Entanglement Preservation in Plasmon-Assisted Light Transmission”. In: *Physical Review Letters* 94.11, p. 110501. ISSN: 0031-9007, 1079-7114. DOI: 10.1103/PhysRevLett.94.110501. URL: <https://link.aps.org/doi/10.1103/PhysRevLett.94.110501> (visited on 04/03/2020).
- Fernandez, Veronica, Robert J. Collins, Karen J. Gordon, Paul D. Townsend, and Gerald S. Buller (Feb. 2007). “Passive Optical Network Approach to Gigahertz-Clocked Multiuser Quantum Key Distribution”. In: *IEEE Journal of Quantum Electronics* 43.2. Conference Name: IEEE Journal of Quantum Electronics, pp. 130–138. ISSN: 1558-1713. DOI: 10.1109/JQE.2006.887175.
- Fox, M. (2006). *Quantum Optics: An Introduction*. Oxford Master Series in Physics. OUP Oxford. ISBN: 978-0-19-856673-1. URL: [https://books.google.com/books?id=2\\_ZP-LDF9jkC](https://books.google.com/books?id=2_ZP-LDF9jkC).
- Fujii, Go, Daiji Fukuda, and Shuichiro Inoue (Aug. 25, 2014). “Direct observation of bosonic quantum interference of surface plasmon polaritons using photon-number-resolving detectors”. In: *Physical Review B* 90.8, p. 085430. ISSN: 1098-0121, 1550-235X. DOI: 10.1103/PhysRevB.90.085430. URL: <https://link.aps.org/doi/10.1103/PhysRevB.90.085430> (visited on 04/03/2020).
- Gao, Bo, Koshala Sarveswaran, Gary H. Bernstein, and Marya Lieberman (Aug. 2010). “Guided Deposition of Individual DNA Nanostructures on Silicon Substrates”. In: *Langmuir* 26.15. Publisher: American Chemical Society, pp. 12680–12683. ISSN: 0743-7463. DOI: 10.1021/la101343k. URL: <https://doi.org/10.1021/la101343k> (visited on 04/28/2020).
- Gerdon, Aren E., Seung Soo Oh, Kuangwen Hsieh, Yonggang Ke, Hao Yan, and H. Tom Soh (2009). “Controlled Delivery of DNA Origami on Patterned Surfaces”. In: *Small* 5.17, pp. 1942–1946. ISSN: 1613-6829. DOI: 10.1002/smll.200900442. URL: <https://onlinelibrary.wiley.com/doi/abs/10.1002/smll.200900442> (visited on 04/28/2020).
- Gerry, Christopher and Peter Knight (2004). *Introductory Quantum Optics*. Cambridge University Press. DOI: 10.1017/CB09780511791239.
- Goltsman, G. N., O. Okunev, G. Chulkova, A. Lipatov, A. Semenov, K. Smirnov, B. Voronov, A. Dzardanov, C. Williams, and Roman Sobolewski (Aug. 2001). “Picosecond superconducting single-photon optical detector”. In: *Applied Physics Letters* 79.6. Publisher: American Institute of Physics, pp. 705–707. ISSN: 0003-6951. DOI: 10.1063/1.1388868. URL: <https://aip.scitation.org/doi/10.1063/1.1388868> (visited on 04/24/2020).

- Gopinath, Ashwin, Evan Miyazono, Andrei Faraon, and Paul W. K. Rothemund (July 2016). “Engineering and mapping nanocavity emission via precision placement of DNA origami”. en. In: *Nature* 535.7612. Number: 7612 Publisher: Nature Publishing Group, pp. 401–405. ISSN: 1476-4687. DOI: 10.1038/nature18287. URL: <https://www.nature.com/articles/nature18287> (visited on 04/22/2020).
- Gopinath, Ashwin and Paul W. K. Rothemund (Dec. 2014). “Optimized Assembly and Covalent Coupling of Single-Molecule DNA Origami Nanoarrays”. In: *ACS Nano* 8.12. Publisher: American Chemical Society, pp. 12030–12040. ISSN: 1936-0851. DOI: 10.1021/nn506014s. URL: <https://doi.org/10.1021/nn506014s> (visited on 04/28/2020).
- Grange, Hornecker and Hunger, Poizat, Gérard, Senellart, and Auffèves (May 2015). “Cavity-Funneled Generation of Indistinguishable Single Photons from Strongly Dissipative Quantum Emitters”. en. In: *Physical Review Letters* 114.19, p. 193601. ISSN: 0031-9007, 1079-7114. DOI: 10.1103/PhysRevLett.114.193601. URL: <https://link.aps.org/doi/10.1103/PhysRevLett.114.193601> (visited on 05/12/2020).
- Guo, Zhenyu, Bradley F. Habenicht, Wan-Zhen Liang, and Oleg V. Prezhdo (Mar. 16, 2010). “*Ab initio* study of phonon-induced dephasing of plasmon excitations in silver quantum dots”. In: *Physical Review B* 81.12, p. 125415. ISSN: 1098-0121, 1550-235X. DOI: 10.1103/PhysRevB.81.125415. URL: <https://link.aps.org/doi/10.1103/PhysRevB.81.125415> (visited on 04/03/2020).
- Ha, Laurence, Chemla, and Weiss (Aug. 1999). “Polarization Spectroscopy of Single Fluorescent Molecules”. In: *The Journal of Physical Chemistry B* 103.33. Publisher: American Chemical Society, pp. 6839–6850. ISSN: 1520-6106. DOI: 10.1021/jp990948j. URL: <https://doi.org/10.1021/jp990948j> (visited on 05/01/2020).
- Heeres, Reinier W., Sander N. Dorenbos, Benny Koene, Glenn S. Solomon, Leo P. Kouwenhoven, and Valery Zwiller (Feb. 10, 2010). “On-Chip Single Plasmon Detection”. In: *Nano Letters* 10.2. Publisher: American Chemical Society, pp. 661–664. ISSN: 1530-6984. DOI: 10.1021/nl903761t. URL: <https://doi.org/10.1021/nl903761t> (visited on 04/03/2020).
- Heeres, Reinier W., Leo P. Kouwenhoven, and Valery Zwiller (Oct. 2013). “Quantum interference in plasmonic circuits”. In: *Nature Nanotechnology* 8.10, pp. 719–722. ISSN: 1748-3387, 1748-3395. DOI: 10.1038/nnano.2013.150. URL: <http://www.nature.com/articles/nnano.2013.150> (visited on 04/03/2020).
- Hennessy, K., A. Badolato, M. Winger, D. Gerace, M. Atatüre, S. Gulde, S. Fält, E. L. Hu, and A. Imamoglu (Feb. 2007). “Quantum nature of a strongly coupled single quantum dot–cavity system”. en. In: *Nature* 445.7130. Number: 7130 Publisher: Nature Publishing Group, pp. 896–899. ISSN: 1476-4687. DOI: 10.1038/nature05586. URL: <https://www.nature.com/articles/nature05586> (visited on 04/26/2020).

- Hiskett, P. A., D. Rosenberg, C. G. Peterson, R. J. Hughes, S. Nam, A. E. Lita, A. J. Miller, and J. E. Nordholt (Sept. 2006). "Long-distance quantum key distribution in optical fibre". en. In: *New Journal of Physics* 8.9. Publisher: IOP Publishing, pp. 193–193. ISSN: 1367-2630. DOI: 10.1088/1367-2630/8/9/193. (Visited on 04/25/2020).
- Hong, C. K. and L. Mandel (Jan. 1986). "Experimental realization of a localized one-photon state". In: *Physical Review Letters* 56.1. Publisher: American Physical Society, pp. 58–60. DOI: 10.1103/PhysRevLett.56.58. URL: <https://link.aps.org/doi/10.1103/PhysRevLett.56.58> (visited on 04/25/2020).
- Hong, C. K., Z. Y. Ou, and L. Mandel (Nov. 2, 1987). "Measurement of subpicosecond time intervals between two photons by interference". In: *Physical Review Letters* 59.18, pp. 2044–2046. ISSN: 0031-9007. (Visited on 04/13/2020).
- Huck, Alexander, Stephan Smolka, Peter Lodahl, Anders S. Sørensen, Alexandra Boltasseva, Jiri Janousek, and Ulrik L. Andersen (June 19, 2009). "Demonstration of Quadrature-Squeezed Surface Plasmons in a Gold Waveguide". In: *Physical Review Letters* 102.24, p. 246802. ISSN: 0031-9007, 1079-7114. DOI: 10.1103/PhysRevLett.102.246802. URL: <https://link.aps.org/doi/10.1103/PhysRevLett.102.246802> (visited on 04/03/2020).
- Hung, Albert M., Christine M. Micheel, Luisa D. Bozano, Lucas W. Osterbur, Greg M. Wallraff, and Jennifer N. Cha (Feb. 2010). "Large-area spatially ordered arrays of gold nanoparticles directed by lithographically confined DNA origami". In: *Nature Nanotechnology* 5.2, pp. 121–126. ISSN: 1748-3387, 1748-3395. DOI: 10.1038/nnano.2009.450. URL: <http://www.nature.com/articles/nnano.2009.450> (visited on 04/18/2020).
- Huo, G, H Chen, and M Zhang (2016). "A Generalized Method for Calculating Phase Matching Conditions in Biaxial Crystals". en. In: *Journal of Lasers, Optics & Photonics* 03.02. ISSN: 2469410X. DOI: 10.4172/2469-410X.1000143. URL: <https://www.omicsgroup.org/journals/a-generalized-method-for-calculating-phase-matching-conditions-inbiaxial-crystals-2469-410X-1000143.php?aid=84557> (visited on 04/22/2020).
- Jiang, Mingming, Jonathan A. Kurvits, Yao Lu, Arto V. Nurmikko, and Rashid Zia (Aug. 2015). "Reusable Inorganic Templates for Electrostatic Self-Assembly of Individual Quantum Dots, Nanodiamonds, and Lanthanide-Doped Nanoparticles". In: *Nano Letters* 15.8. Publisher: American Chemical Society, pp. 5010–5016. ISSN: 1530-6984. DOI: 10.1021/acs.nanolett.5b01009. URL: <https://doi.org/10.1021/acs.nanolett.5b01009> (visited on 04/27/2020).
- Jin, J.I.I. and J. Grote (2016). *Materials Science of DNA*. CRC Press. ISBN: 978-1-4398-2742-0. URL: <https://books.google.com/books?id=cInRBQAAQBAJ>.
- Kaiser, W. and W. L. Bond (Aug. 1959). "Nitrogen, A Major Impurity in Common Type I Diamond". In: *Physical Review* 115.4. Publisher: American Phys-

- ical Society, pp. 857–863. DOI: [10.1103/PhysRev.115.857](https://doi.org/10.1103/PhysRev.115.857). URL: <https://link.aps.org/doi/10.1103/PhysRev.115.857> (visited on 04/25/2020).
- Kershner, Ryan J., Luisa D. Bozano, Christine M. Micheel, Albert M. Hung, Ann R. Fornof, Jennifer N. Cha, Charles T. Rettner, Marco Bersani, Jane Frommer, Paul W. K. Rothemund, and Gregory M. Wallraff (Sept. 2009). “Placement and orientation of individual DNA shapes on lithographically patterned surfaces”. en. In: *Nature Nanotechnology* 4.9. Number: 9 Publisher: Nature Publishing Group, pp. 557–561. ISSN: 1748-3395. DOI: [10.1038/nnano.2009.220](https://doi.org/10.1038/nnano.2009.220). URL: <https://www.nature.com/articles/nnano.2009.220> (visited on 04/28/2020).
- Knill, E., R. Laflamme, and G. J. Milburn (Jan. 2001). “A scheme for efficient quantum computation with linear optics”. In: *Nature* 409.6816, pp. 46–52. ISSN: 1476-4687. DOI: [10.1038/35051009](https://doi.org/10.1038/35051009). URL: <https://www.nature.com/articles/35051009> (visited on 04/24/2020).
- Kolesov, Roman, Bernhard Grotz, Gopalakrishnan Balasubramanian, Rainer J. Stöhr, Aurélien A. L. Nicolet, Philip R. Hemmer, Fedor Jelezko, and Jörg Wrachtrup (July 2009). “Wave–particle duality of single surface plasmon polaritons”. In: *Nature Physics* 5.7, pp. 470–474. ISSN: 1745-2473, 1745-2481. DOI: [10.1038/nphys1278](https://doi.org/10.1038/nphys1278). URL: <http://www.nature.com/articles/nphys1278> (visited on 04/03/2020).
- Kuzyk, Anton, Bernard Yurke, J. Jussi Toppari, Veikko Linko, and Päivi Törmä (2008). “Dielectrophoretic Trapping of DNA Origami”. en. In: *Small* 4.4, pp. 447–450. ISSN: 1613-6829. DOI: [10.1002/sml1.200701320](https://doi.org/10.1002/sml1.200701320). URL: <https://onlinelibrary.wiley.com/doi/abs/10.1002/sml1.200701320> (visited on 04/28/2020).
- Langmuir, I. (1928). “Oscillations in ionized gases”. In: 14, p. 11.
- Liu, Mingzhao, Matthew Pelton, and Philippe Guyot-Sionnest (Jan. 27, 2009). “Reduced damping of surface plasmons at low temperatures”. In: *Physical Review B* 79.3, p. 035418. ISSN: 1098-0121, 1550-235X. DOI: [10.1103/PhysRevB.79.035418](https://doi.org/10.1103/PhysRevB.79.035418). URL: <https://link.aps.org/doi/10.1103/PhysRevB.79.035418> (visited on 04/03/2020).
- Maier, Stefan A. (2007). *Plasmonics: Fundamentals and Applications*. Springer, New York, NY. DOI: <https://doi.org/10.1007/0-387-37825-1>.
- Marton, L., J. Arol Simpson, H. A. Fowler, and N. Swanson (Apr. 1, 1962). “Plural Scattering of 20-kev Electrons in Aluminum”. In: *Physical Review* 126.1, pp. 182–192. ISSN: 0031-899X. DOI: [10.1103/PhysRev.126.182](https://doi.org/10.1103/PhysRev.126.182). URL: <https://link.aps.org/doi/10.1103/PhysRev.126.182> (visited on 04/03/2020).
- Michler, P., A. Imamoğlu, M. D. Mason, P. J. Carson, G. F. Strouse, and S. K. Buratto (Aug. 2000). “Quantum correlation among photons from a single quantum dot at room temperature”. en. In: *Nature* 406.6799, pp. 968–970. ISSN: 1476-4687. DOI: [10.1038/35023100](https://doi.org/10.1038/35023100). URL: <https://www.nature.com/articles/35023100> (visited on 04/25/2020).

- Pearson, Anthony C., Elisabeth Pound, Adam T. Woolley, Matthew R. Linford, John N. Harb, and Robert C. Davis (May 2011). “Chemical Alignment of DNA Origami to Block Copolymer Patterned Arrays of 5 nm Gold Nanoparticles”. In: *Nano Letters* 11.5. Publisher: American Chemical Society, pp. 1981–1987. ISSN: 1530-6984. DOI: 10.1021/nl200306w. URL: <https://doi.org/10.1021/nl200306w> (visited on 04/28/2020).
- Penzo, Erika, Risheng Wang, Matteo Palma, and Shalom J Wind (Nov. 2011). “Selective placement of DNA origami on substrates patterned by nanoimprint lithography”. In: *Journal of Vacuum Science & Technology B* 29.6. Publisher: American Vacuum Society, 06F205. ISSN: 2166-2746. DOI: 10.1116/1.3646900. URL: <https://avs.scitation.org/doi/10.1116/1.3646900> (visited on 04/28/2020).
- Persson, Westerlund, Tegenfeldt, and Kristensen (2009). “Local Conformation of Confined DNA Studied Using Emission Polarization Anisotropy”. In: *Small* 5.2, pp. 190–193. ISSN: 1613-6829. DOI: 10.1002/smll.200800423. URL: <https://onlinelibrary.wiley.com/doi/abs/10.1002/smll.200800423> (visited on 05/01/2020).
- Peyskens, Frédéric, Chitrleema Chakraborty, Muhammad Muneeb, Dries Van Thourhout, and Dirk Englund (Sept. 2019). “Integration of single photon emitters in 2D layered materials with a silicon nitride photonic chip”. en. In: *Nature Communications* 10.1. Number: 1 Publisher: Nature Publishing Group, pp. 1–7. ISSN: 2041-1723. DOI: 10.1038/s41467-019-12421-0. URL: <https://www.nature.com/articles/s41467-019-12421-0> (visited on 04/27/2020).
- Pilo-Pais, Mauricio, Guillermo P. Acuna, Philip Tinnefeld, and Tim Liedl (Dec. 2017). “Sculpting light by arranging optical components with DNA nanostructures”. en. In: *MRS Bulletin* 42.12, pp. 936–942. ISSN: 0883-7694, 1938-1425. DOI: 10.1557/mrs.2017.278. URL: [https://www.cambridge.org/core/product/identifier/S0883769417002780/type/journal\\_article](https://www.cambridge.org/core/product/identifier/S0883769417002780/type/journal_article) (visited on 04/22/2020).
- Ritchie, R. H. (June 1, 1957). “Plasma Losses by Fast Electrons in Thin Films”. In: *Physical Review* 106.5, pp. 874–881. ISSN: 0031-899X. DOI: 10.1103/PhysRev.106.874. URL: <https://link.aps.org/doi/10.1103/PhysRev.106.874> (visited on 04/03/2020).
- Rothmund, Paul W. K. (Mar. 1, 2006). “Folding DNA to create nanoscale shapes and patterns”. In: *Nature* 440.7082, pp. 297–302. ISSN: 1476-4687. DOI: 10.1038/nature04586. URL: <https://doi.org/10.1038/nature04586>.
- Saxena, Abhi, Yueyang Chen, Albert Ryou, Carlos G. Sevilla, Peipeng Xu, and Arka Majumdar (Dec. 2019). “Improving Indistinguishability of Single Photons from Colloidal Quantum Dots Using Nanocavities”. In: *ACS Photonics* 6.12. Publisher: American Chemical Society, pp. 3166–3173. DOI: 10.1021/acsp Photonics.9b01481. (Visited on 04/25/2020).

- Scharte, Mathias, Ron Porath, Torsten Ohms, Martin Aeschlimann, Bernhard Lamprecht, Harald Ditlbacher, and Franz Rembert Aussenegg (Dec. 5, 2001). "Lifetime and dephasing of plasmons in Ag nanoparticles". In: *Controlling and Using Light in Nanometric Domains*. Controlling and Using Light in Nanometric Domains. Vol. 4456. International Society for Optics and Photonics, pp. 14–21. DOI: 10.1117/12.449533. URL: <https://www.spiedigitallibrary.org/conference-proceedings-of-spie/4456/0000/Lifetime-and-dephasing-of-plasmons-in-Ag-nanoparticles/10.1117/12.449533.short> (visited on 04/03/2020).
- Scheible, Max B., Günther Pardatscher, Anton Kuzyk, and Friedrich C. Simmel (Mar. 2014). "Single Molecule Characterization of DNA Binding and Strand Displacement Reactions on Lithographic DNA Origami Microarrays". In: *Nano Letters* 14.3. Publisher: American Chemical Society, pp. 1627–1633. ISSN: 1530-6984. DOI: 10.1021/nl500092j. URL: <https://doi.org/10.1021/nl500092j> (visited on 04/28/2020).
- Schins, Agronskaia, Grooth, and Greve (1999). "Orientation of the chromophore dipoles in the TOTO-DNA system". In: *Cytometry* 37.3, pp. 230–237. ISSN: 1097-0320. DOI: 10.1002/(SICI)1097-0320(19991101)37:3<230::AID-CYT010>3.0.CO;2-#. (Visited on 05/01/2020).
- Schlosshauer, Maximilian (Feb. 23, 2005). "Decoherence, the measurement problem, and interpretations of quantum mechanics". In: *Reviews of Modern Physics* 76.4, pp. 1267–1305. ISSN: 0034-6861, 1539-0756. DOI: 10.1103/RevModPhys.76.1267. URL: <https://link.aps.org/doi/10.1103/RevModPhys.76.1267> (visited on 04/03/2020).
- Seeman, Nadrian C. (Nov. 21, 1982). "Nucleic acid junctions and lattices". In: *Journal of Theoretical Biology* 99.2, pp. 237–247. ISSN: 0022-5193. DOI: 10.1016/0022-5193(82)90002-9. URL: <http://www.sciencedirect.com/science/article/pii/0022519382900029> (visited on 04/19/2020).
- Seeman, Nadrian C and Philip S Lukeman (2004). "Nucleic acid nanostructures: bottom-up control of geometry on the nanoscale". In: *Reports on Progress in Physics* 68.1, pp. 237–270. DOI: 10.1088/0034-4885/68/1/r05.
- Shoji, T., T. Tsuchizawa, T. Watanabe, K. Yamada, and H. Morita (2002). "Low loss mode size converter from 0.3  $\mu\text{m}$  square Si wire waveguides to singlemode fibres". In: *Electronics Letters* 38.25, pp. 1669–1670.
- Sick, Hecht, and Novotny (Nov. 2000). "Orientational Imaging of Single Molecules by Annular Illumination". In: *Physical Review Letters* 85.21. Publisher: American Physical Society, pp. 4482–4485. DOI: 10.1103/PhysRevLett.85.4482. URL: <https://link.aps.org/doi/10.1103/PhysRevLett.85.4482> (visited on 05/01/2020).

- Sönnichsen, C., T. Franzl, T. Wilk, G. von Plessen, J. Feldmann, O. Wilson, and P. Mulvaney (Jan. 31, 2002). “Drastic Reduction of Plasmon Damping in Gold Nanorods”. In: *Physical Review Letters* 88.7, p. 077402. ISSN: 0031-9007, 1079-7114. DOI: 10.1103/PhysRevLett.88.077402. URL: <https://link.aps.org/doi/10.1103/PhysRevLett.88.077402> (visited on 04/03/2020).
- Spielmann, Wemmer, and Jacobsen (July 1995). “Solution Structure of a DNA Complex with the Fluorescent Bis-Intercalator TOTO Determined by NMR Spectroscopy”. In: *Biochemistry* 34.27. Publisher: American Chemical Society, pp. 8542–8553. ISSN: 0006-2960. DOI: 10.1021/bi00027a004. URL: <https://doi.org/10.1021/bi00027a004> (visited on 05/01/2020).
- Stockman, Mark I. (June 2008). “Spasers explained”. In: *Nature Photonics* 2.6, pp. 327–329. ISSN: 1749-4885, 1749-4893. DOI: 10.1038/nphoton.2008.85. URL: <http://www.nature.com/articles/nphoton.2008.85> (visited on 04/03/2020).
- Tame, M. S., C. Lee, J. Lee, D. Ballester, M. Paternostro, A. V. Zayats, and M. S. Kim (Nov. 7, 2008). “Single-Photon Excitation of Surface Plasmon Polaritons”. In: *Physical Review Letters* 101.19, p. 190504. ISSN: 0031-9007, 1079-7114. DOI: 10.1103/PhysRevLett.101.190504. URL: <https://link.aps.org/doi/10.1103/PhysRevLett.101.190504> (visited on 04/03/2020).
- Tame, M. S., K. R. McEnery, Ş. K. Özdemir, J. Lee, S. A. Maier, and M. S. Kim (June 2013). “Quantum plasmonics”. In: *Nature Physics* 9.6, pp. 329–340. ISSN: 1745-2473, 1745-2481. DOI: 10.1038/nphys2615. URL: <http://www.nature.com/articles/nphys2615> (visited on 04/03/2020).
- Tokpanov, Yury S., James S. Fakonas, Benjamin Vest, and Harry A. Atwater (Oct. 16, 2019). “Quantum Coherence Preservation in Extremely Dispersive Plasmonic Media”. In: *Physical Review Applied* 12.4, p. 044037. ISSN: 2331-7019. DOI: 10.1103/PhysRevApplied.12.044037. URL: <https://link.aps.org/doi/10.1103/PhysRevApplied.12.044037> (visited on 04/09/2020).
- Tonndorf, Philipp, Robert Schmidt, Robert Schneider, Johannes Kern, Michele Buscema, Gary A. Steele, Andres Castellanos-Gomez, Herre S. J. van der Zant, Steffen Michaelis de Vasconcellos, and Rudolf Bratschitsch (Apr. 2015). “Single-photon emission from localized excitons in an atomically thin semiconductor”. EN. In: *Optica* 2.4. Publisher: Optical Society of America, pp. 347–352. ISSN: 2334-2536. DOI: 10.1364/OPTICA.2.000347. URL: <https://www.osapublishing.org/optica/abstract.cfm?uri=optica-2-4-347> (visited on 04/27/2020).
- Tran, Toan Trong, Kerem Bray, Michael J. Ford, Milos Toth, and Igor Aharonovich (Jan. 2016). “Quantum emission from hexagonal boron nitride monolayers”. en. In: *Nature Nanotechnology* 11.1. Number: 1 Publisher: Nature Publishing Group, pp. 37–41. ISSN: 1748-3395. DOI: 10.1038/nnano.2015.242. URL: <https://www.nature.com/articles/nnano.2015.242> (visited on 04/27/2020).

- Wein, Lauk, Ghobadi, and Simon (May 2018). “Feasibility of efficient room-temperature solid-state sources of indistinguishable single photons using ultra-small mode volume cavities”. In: *Physical Review B* 97.20. arXiv: 1710.03742, p. 205418. ISSN: 2469-9950, 2469-9969. DOI: 10.1103/PhysRevB.97.205418. URL: <http://arxiv.org/abs/1710.03742> (visited on 05/12/2020).
- Whitesides GM Mathias JP, Seto CT (Feb. 1991). “Molecular self-assembly and nanochemistry: a chemical strategy for the synthesis of nanostructures”. In: *Science* 254.5036, pp. 1312–1319. DOI: <https://doi.org/10.1126/science.1962191>.
- Zhang, Xin, Chang Xu, and Zhongzhou Ren (Feb. 2018). “High fidelity heralded single-photon source using cavity quantum electrodynamics”. en. In: *Scientific Reports* 8.1, pp. 1–8. ISSN: 2045-2322. DOI: 10.1038/s41598-018-21481-z. URL: <https://www.nature.com/articles/s41598-018-21481-z> (visited on 04/25/2020).
- Zhang, Yuwen and Nadrian C. Seeman (Mar. 1994). “Construction of a DNA-Truncated Octahedron”. In: *Journal of the American Chemical Society* 116.5, pp. 1661–1669. ISSN: 0002-7863. DOI: 10.1021/ja00084a006. URL: <https://pubs.acs.org/doi/abs/10.1021/ja00084a006> (visited on 04/21/2020).

## FABRICATION METHODS

### **A.1 Samples path-entanglement experiments**

Fabrication methods for the chip that was used to perform entanglement experiments in Chapter 2 are described in the thesis by James Fakonas: Fakonas, James Spencer (2015), "Quantum Interference and Entanglement of Surface Plasmonons" (<https://resolver.caltech.edu/CaltechTHESIS:12052014-101005469>).

### **A.2 Fabrication and simulation methods of PCC arrays**

Fabrication and simulation methods of PCC arrays and description of the experimental setups for deterministic DNA origami placement with arbitrary orientation presented in the first section of Chapter 3 are described in the supplementary material to our paper: Gopinath, Ashwin et al. (2018). "Absolute and arbitrary orientation of single molecule shapes". In: arXiv:1808.04544 [physics.app-ph].

### **A.3 Fabrication of substrates for placement**

Substrates for experiments with origami functionalized with Eu ion complexes were fabricated in Caltech's Kavli Nanoscience Institute cleanroom. Quartz slides from SPI Supplies (Brand Quartz Microscope Slide 1 × 1 in. × 0.5 mm) were used as substrates for these experiments.

- In the first step of the fabrication process gold grid with labelled 3  $\mu\text{m}$  squares was fabricated by lift-off process. Two layers of PMMA electron-beam resist were spin-coated on the substrates. Electron-beam lithography was used to expose resist and write the grid pattern. Afterwards, the samples were developed in 1:3 MIBK(Methyl isobutyl ketone):IPA(Isopropanol) solution for 60 seconds.
- During the second step, 100 nm of gold was deposited on the developed samples using electron-beam evaporation process. To lift off the gold on the unexposed PMMA area the samples were left overnight in acetone. Next day the samples were rinsed in acetone followed by IPA and blow dried in nitrogen. The grid pattern was left on the substrate were PMMA was completely developed.

- The third step of fabrication lithographically defined binding sites for DNA origami arrays. The sample with fabricated gold grid lines, labels and squares was treated with oxygen plasma for 5 min and silanized with a trimethylsilyl passivation layer by vapor deposition of HMDS (hexamethyldisilazane). A thin (100 nm) layer of PMMA 950 A3 was spun-coat on the substrate as a resist. Binding sites in the shape of a DNA origami are defined in the resist with e-beam lithography and developed.

This completes the fabrication part that was taking place in the cleanroom. After the above mentioned steps the sample was brought upstairs into the DNA laboratory. 24 hours prior to DNA origami placement the sample was exposed to oxygen plasma for 90 seconds. The exact time could be varied depending on the desired size of the binding sites for DNA origami. Ideally, you would want the disk-shaped site to be exactly the same size as death star origami. However, if the sample is underexposed or underdeveloped during the electron-beam lithography, the last oxygen plasma step could be prolonged for up to 2 min. This step insures that the trimethylsilyl passivation layer is selectively removed at the binding sites and this step is called "activation". Finally, the residual PMMA resist is removed by sonication in Remover PG solvent at 50°C to reveal a substrate that is composed of two chemically distinct regions: (1) origami-shaped features covered with ionizable surface silanols ( $\text{OH}^-$ ) and (2) a neutrally charged background covered with trimethylsilyl groups that prevents DNA origami binding. This procedure enables good DNA origami placement in  $\text{Mg}^{2+}$  buffer.

#### A.4 DNA origami preparation

- **Designs.** Death star origami were designed with caDNAno (<http://cadnano.org/>) software. All 5' ends of the staples are located at the same side of the origami and extensions are always added to the same 5' end of the origami.
- **Origami mixture.** Staple mix was prepared by adding 1  $\mu\text{L}$  of each strand with 100  $\mu\text{M}$  concentration (Integrated DNA Technologies). The scaffold that was used for death star origami is single-stranded M13mp18 (Tilibit) at 100 nM concentration in water. We found that staple to scaffold ratios that worked for us are any between 2.5 to 1 and 10 to 1, respectively. The target concentration for DNA origami usually was 20 nM and the origami were

annealed in 1x TAE (prepared from 50x TAE from Bio-Rad) buffer and 12.5 mM MgCl<sub>2</sub>. Staples mixes and scaffolds are stored in the freezer at -5°.

- **Annealing.** 50  $\mu$ L of staple/scaffold mixture was prepared in 0.5 ml DNA LoBind tubes (Eppendorf) to minimize loss of origami to the sides of the tube. Then the tubes were heated to 90°C for 5 min and annealed from 90°C to 20°C at -0.2°C/min in a PCR machine. The annealed origami could be stored in the refrigerator before purification step.
- **Purification.** The origami were purified away from excess staples using 100 kDa molecular weight cut-off spin filters (Amicon) in 1x TAE 12.5 mM MgCl<sub>2</sub> buffer at room temperature. The first step is to wet the spin filter by running 500  $\mu$ L of the buffer at 3000 rcf for 8 min. The filtrate was discarded, 50  $\mu$ L of origami were added to filter and the remaining volume was filled up with the buffer. Then the following steps were repeated 4 times: run the centrifuge at 3000 rcf for 8 min at room temperature, discard the filtrate, fill up the filter with the buffer. After 4 spinning rounds, the filter was reversed, placed in a new tube and centrifuged again at 3000 rcf for 5 min. The filtered origami that were pushed out of the spin filter were collected and transferred for storage to 500  $\mu$ L LoBind tube.
- **Concentration measurement.** After purification, the origami concentration was measured using a NanoDrop spectrophotometer (Thermo Scientific). The theoretical molar extinction coefficient of a fully double-stranded M13mp18 molecule ( $\epsilon = 123,735,380 \text{ M}^{-1}\text{cm}^{-1}$ ) was used to calculate concentration from the measured extinction coefficient by NanoDrop. After 4 purification cycles, we usually measure 10-15 nM concentration of DNA origami for initial scaffold concentrations of 20 nM. The origami should be stored at concentration above 10 nM to prevent degradation of the concentration due to the binding of the origami to the walls of the LoBind tube.

#### A.5 DNA origami placement procedure

- **Incubation.** Incubation was done in a covered petri dish with wet Kimtech wipes inside to prevent the samples from drying out. For DNA origami placement solution with 500 pM origami was prepared in placement buffer (10 mM Tris, 40 mM MgCl<sub>2</sub>, pH 8.3) and a 20  $\mu$ L droplet was deposited in the middle of the chip on top of the patterned region. The chip was placed in

a closed, humid petri dish and the origami solution was allowed to incubate on the chip for 1 hour.

- **Washing.** After the 1 hour incubation, excess origami (in solution) were washed away with at least 5 buffer washes by pipetting 40  $\mu\text{L}$  of fresh placement buffer onto the chip, and pipetting 40  $\mu\text{L}$  off of the chip. Each of the 5 washes consisted of pipetting the 40  $\mu\text{L}$  volume up and down 2–3 times to mix the fresh buffer with existing buffer on the chip. Next, in order to remove origami that were non-specifically bound to the passivated background, the chip was buffer-washed 3 times using a Tween washing buffer made by adding 0.1% Tween 20 (v/v) to placement buffer. Because of the low surface tension of the Tween washing buffer, these washes were somewhat tricky: they involved adding 20–40  $\mu\text{L}$  of Tween wash buffer, just enough to cover most of the chip, but not enough to spill over the chip and wet the back side of the chip (this may introduce dust contamination from the petri dish).
- **Tween incubation.** After the 3rd wash, the chip was left to incubate for 30 minutes in the Tween buffer.
- **Final wash.** After 30-minutes incubation the chip was washed again for 5 times in Tween buffer.
- **Ethanol drying.** After DNA origami were washed out in a two-step process, the samples were dried by exposure to an ethanol dilution series: 10 seconds in 50% ethanol, 30 seconds in 75% ethanol, and 120 seconds in 90% ethanol. To remove remaining 90% ethanol, chips were dried by compressed air from an office duster.

## A.6 AFM characterization

All AFM images were acquired using a Dimension Icon AFM/Nanoscope V Scanner (Bruker). Dried samples were scanned in air by a cantilever from an SNL-10 probe (Bruker) at 62 kHz resonance. High-contrast height imaging was performed to identify small (3  $\mu\text{m}$ ) origami arrays inside a 100nm gold grid. The zoomed-in images of individual origami were performed by the same AFM tip with higher resolution and slower scanning speed. AFM images were processed using Gwyddion (<http://gwyddion.net/>) and ImageJ (<https://imagej.nih.gov/ij/>).